UNIVERSITAT POLITÈCNICA DE CATALUNYA
BARCELONATECH
Escola Superior d'Enginyeries Industrial,
Aeroespacial i Audiovisual de Terrassa

Study of Machine Learning Techniques for modelling Large Structural Vibrations

BACHELOR FINAL THESIS

Document:

Report

Author:

Albert Llonch Majó

Director/Co-director:

Dr. Joaquín Alberto Hernández Ortega

Degree:

Bachelor on Aerospace Technologies Engineering

Call:

Spring, 2022 - Extension

Abstract

The main purpose of the present work can be divided into two separate objectives.

The first one and most important is to study the different computational techniques that are used in the structural vibrations modelling field in both the linear and nonlinear regimes, as well as their methodology of implementation. In particular, this thesis places special emphasis on a specific order-reducing model called hyperreduction. This approach makes use of Machine Learning techniques such as the Singular Value Decomposition to solve an optimization problem that selects the set of reduced elements to be integrated from the entirety of finite elements of the mesh.

To do so, several simulations are launched an analysed throughout the study. These simulations intend to estimate the dynamic response that a simple 2D cantilever beam would suffer when subjected under different types of boundary conditions. Such a task is performed thanks to a Finite Element Method based on the Galerkin approximation. With the help of Matlab, the semi-discrete equation of motion that governs the dynamic response of the system can be computationally integrated making use of the Newmark-Bossak scheme and the Newton-Raphson algorithm.
The results obtained from the Finite Element study will be compared with the analytical solution deduced from the modal analysis decomposition technique and also with the results obtained from the hyperreduction stage.

On the other hand, the second goal of this thesis is to study the dynamic response of the above-mentioned structure when subjected to the action of real wind gusts. This study is included in the list of simulations to be launched in this project.
In this sense, the Fast Fourier Transform (FFT) is also employed in order to obtain a continuous representation in the time domain of a discrete data set representing real measurements of wind speed.

The main conclusion of this work is that the hyperreduction method is significantly more efficient than a standard Finite Element method since it requires less than 1% of the finite elements of the mesh to integrate the semi-discrete equation of motion, thus contributing to achieving reductions of up to 96% in computational time within an accuracy tolerance of the order of 10^{-3}. Therefore, this technique is a highly valuable tool in any engineering field that involves simulations with very refined meshes or with complex nonlinear conditions among others, since they require great computational efforts.

El principal propòsit d'aquest treball es divideix en dos objectius diferenciats:

En primer lloc, l'objectiu més important és el d'estudiar les diferents tècniques de computació que s'utilitzen en el camp de la modelització de vibracions estructurals, tant en el règim lineal com en el no lineal, així com la seva metodologia d'implementació. En particular, aquesta tesis dona especial importància a un mètode concret de reducció d'orde, anomenat *hiperreducció*. Aquest mètode fa servir tècniques de *Machine Learning* com per exemple el *Singular Value Decomposition* per resoldre un problema d'optimització que permet seleccionar el conjunt d'elements a integrar, respecte del total d'elements finits que formen la malla.

Per fer-ho, es llancen un conjunt de simulacions al llarg de l'estudi. Aquestes simulacions intenten estimar la resposta dinàmica que experimentaria una biga 2D en voladís quan fos sotmesa sota diferents tipus de condicions de contorn. Aquesta tasca com a tal és realitzada gràcies a un Mètode d'Elements Finits basat en l'aproximació de Galerkin. Amb l'ajuda de Matlab, l'equació semi-discreta de moviment que regeix la resposta dinàmica del sistema es pot integrar computacionalment fent servir l'esquema de Newmark-Bossak i l'algoritme de Newton-Raphson.

Els resultats obtinguts del estudi d'Elements Finits es compararà amb la solució analítica deduïda de l'anàlisi de descomposició modal així com també amb els resultats obtinguts de *l'hiperreducció*.

Per altra banda, el segon objectiu d'aquesta tesis és poder estudiar la resposta dinàmica de l'estructura mencionada anteriorment quan aquesta és sotmesa a l'acció de ràfegues de vent reals. Aquest estudi està inclòs a la llista de simulacions que es llançaran al llarg del projecte.

En aquest sentit, la Transformada Ràpida de Fourier (FFT) és també usada amb la intenció d'aconseguir una representació continua en el domini temporal d'un conjunt de dades que representen mesures reals de la velocitat del vent.

La conclusió principal d'aquest projecte és que el mètode *d'hiperreducció* és significativament més eficient que un mètode estàndard d'Elements Finits ja que només necessita menys d'un 1% del total d'elements finits que formen la malla per integrar l'equació semi-discreta de moviment, contribuïnt així a aconseguir reduccions de fins el 96% en temps de computació dins una tolerància de precisió de l'orde de 10^{-3}. Per tant, aquesta tècnica és una eina altament valuosa en qualsevol camp de l'enginyeria que involucri simulacions amb malles molt denses o amb condicions no lineals complexes entre altres, ja que requereixen grans esforços computacionals.

Table of Contents

List of Figures

List of Tables

List of abbreviations / Glossary

Afegir el llistat d'abreviatures o glossari si s'escau.

ML - Machine Learning

FEM - Finite Elements Method

HROM - Hyperreduced Order Model

FFT - Fast Fourier Transform

ROM - Reduced Order Model

PK1 - First Piola-Kirchhoff stress tensor

PK2 - Second Piola-Kirchhoff stress tensor

S.F - Strong Form

W.F - Weak Form

DOF - Degree of Freedom

ODE - Ordinary Differential Equation

FT - Fourier Transform

IFT - Inverse Fourier Transform

SVD - Singular Value Decomposition

SVDT - Truncated Singular Value Decomposition

DFT - Discrete Fourier Transform

ECM - Empirical Cubature Method

PCA - Principal Component Analysis

Chapter 1

Introduction

1.1 Object

The object of this project is to get familiar with the computational techniques that are used in real-life projects that study both linear and nonlinear structural vibrations, going through the time integration schemes, rigid body semi-discrete equations of motion, etc. and to explore a specific ML approach that significantly enhances the computational efficiency.
In this project, the student will conduct a study on the finite element method (FEM) used for modelling structural vibrations of large amplitude, going through the conventional computational techniques applied to this theory and exploring other new methodologies that combine the conventional ones with machine ML technique known as Hyperreduction Order Model (HROM).

On the one hand, the student will conduct several FEM simulations in the linear regime, including the analysis of the dynamic response of a structure submitted to real wind gusts. On the other hand, the nonlinear regime will also be analysed and discussed.

1.2 Scope

This project will be divided into five different blocks.

1. **Introduction to large strains**

   In this block the student will complement and expand his education on the theory of small strains, as well as get introduced to the large strains regime in both the static and the dynamic regimes. Furthermore, he will acquire familiarity with some computational methods used to study these regimes, such as the Newmark-Bossak method (for integrating the semi-discrete motion equation) or the theory of model order reduction for linear structures (standard modal analysis).

2. **Studying and understanding the formulation and methodology behind both the Finite Element Method (FEM) and the modal analysis code**

In this pack, the student will examine a series of given Matlab codes used for simulating small and large strains in structural analysis and understand its functioning, thanks to the acquired theory from the first block. Precisely, the student will carry out the analysis of the Newmark-Bossak method, the Newton Raphson algorithm and the classical linear modal approach.

3. **Code testing and adapting**

   Once the student is able to understand the coding, he will run a series of finite element simulations for different boundary conditions and external forces to compare the performance of the Newmark-Bossak method with the predictions provided by the linear modal analysis. To conduct this variety of studies, the student will also have to perform some adaptations and/or modifications to some functions of the original code.

   Moreover, to conduct a more rigorous analysis, the student will make use of the software GiD for pre and postprocess purposes, in order to visualize the behaviour of the structure in a clearer way.

4. **Study of the hyperreduced order model (HROM) and comparison with other techniques**

   As done in blocks 2 and 3, the student will study the theory behind the HROM and the ML techniques for mining data from FE simulations that this method implies.

   A comparison of this method's results with the predictions from both the modal analysis and the FEM will also be performed in this block.

5. **Fourier analysis**

   This pack is independent of the rest and its objective is to obtain a temporal and continuous expression from a series of discrete data obtained from real measurements of wind speed along time.

   To do that, the student will have to create a code which will make us of the Fast Fourier Transform (FFT) algorithm.

It is important to notice that, except for the last block, the student will not develop any original Matlab code, nor will he create any structure or mesh using GiD. All these resources will be provided by this project's director in order for the student to be able to conduct a proper and complete study within the accepted time allocations.
However, the student will have to conduct some adaptations to the given code, since it is only prepared to cope with specific boundary conditions.

Buckling analysis, code optimization and aerodynamic analysis are out of the scope of the present work.

1.3 Requirements

The requirements that the final solution of this project must meet are divided into project management requirements and technical requirements.

Project management requirements:

- The project dedication must be roughly 300 hours.
- The project must be written and presented in English.
- There must be a project meeting at least one day a week with the project director to monitor and supervise the advances made by the student.
- Deadlines must be respected.

Technical requirements:

- All the data obtained from all the FE or HROM simulations must be extracted and stored offline.
- The developed code must be created with and for MATLAB and must be as accurate and efficient as possible.
- Any creation or modification of the finite element structure or its mesh must be carried out using GiD.
- The pre and post process of any simulation or test must be done with GiD.

1.4 Rationale

Data-driven discovery is currently revolutionizing how we model, predict, and control complex systems. The most pressing scientific and engineering problems of the modern era are not amenable to empirical models or derivations based on first-principles. These systems are typically nonlinear, dynamic, multi-scale in space and time, high-dimensional, with dominant underlying patterns that should be characterized and modeled for the eventual goal of sensing, prediction, estimation, and control. With modern mathematical methods, enabled by unprecedented availability of data and computational resources, we are now able to tackle previously unattainable challenge problems [1].

Driving modern data science is the availability of vast and increasing quantities of data, enabled by remarkable innovations in low-cost sensors, orders-of-magnitudes increases in computational power, and virtually unlimited data storage and transfer capabilities. Such vast quantities of data are affording engineers and scientists across all disciplines new opportunities for data-driven discovery, which has been referred to as the fourth paradigm of scientific discovery [2]. This fourth paradigm is the natural culmination of the first three paradigms: empirical experimentation, analytical derivation, and computational investigation. In the context of this new paradigm, machine learning techniques and algorithms play a crucial role, as they are created to cope with such large amounts of data (nowadays also referred as Big Data) obtained from measurements of a complex system, identify and classify it, and combine it with the theory that governs the above-mentioned method to produce fast, efficient subrogate models, able to provide predictions in almost real time.

Increasingly, researchers are turning to data-driven approaches for a diverse range of those complex systems, such as turbulence, the brain, climate, epidemiology, finance, robotics, autonomy and structural vibration modelling among others.

In this circumstance and relating to these novel techniques, accurate modelling of structural vibrations of

large amplitude is of utmost importance in the aerospace field. The industry of aviation is gaining more and more importance through the years and it does not appear to be changing in the future. Two of the most important aspects of this sector are safety and reliability. Being able to predict the structural behaviour of a plane when given, for example, some specific meteorologic conditions, would represent a major breakthrough for the industry.

As such, this project will intend to carry out a study of how small and large strains caused by the effect of random wind gusts are computationally modelled using the FEM combined with the FFT, and answer whether certain new ML techniques and algorithms can be applied to the FEM for the sake of modelling the dynamic structural response in a more efficient way.

Chapter 2

Review of the state of the art

Taking into consideration that this thesis addresses different topics, this chapter intends to give a brief contextualization of the state of the art of each of them.

2.1 Finite Elements Method

Essentially, a Finite Element Method is an approximation method that reduces a problem space, most usually a structure, into a numerous small and easier to deal with pieces referred to as the finite elements.
Analysing the semi-discrete equations that govern the behaviour of the structure is way simpler when the physical domain is a quadrilateral/triangular element, for 2D cases, or a tetrahedral/hexahedral element for 3D cases.

FEM was originally developed for engineering analysis to model and analyze complex systems in mechanical, civil, and aeronautical engineering. It has as its foundation the basic concepts of mechanics, such as Newton's laws of motion, conservation of mass and energy, equilibrium, and the laws of thermodynamics.

FEMs are nowadays used inside a wide range of applications, being the more common ones the study of structural mechanics of structures under different loading conditions, the heat flows, or the distribution of electromagnetic radiation.
Such phenomena are described by multiple interdependent partial-differential equations that involve different variables (being space and time the most usual). The main intention of the FEMs is to deal with these equations and, to do so, they use one of the following approaches:

- **Variational methods:** are the most common in FEMs and is the technique that will be addressed in this thesis. They are based on the energy minimization principle.
  Knowing the equations that define the minimum-energy condition enables the definition of "weak form" equations, so called because they allow for discontinuities that are inherent in a system in which each element is analyzed separately.
  These equations enable discretization to a set of matrix equations (one for each finite element), which

are solved by an iterative solver.

- **Finite difference analysis:** it approximates the derivatives driving the PDEs by use of finite difference equations.

The Finite Elements Method can be employed to analyse three types of problems:

- **Static**: Frequently used in structural analysis to assess the stress that certain parts of a structure can be exposed to when specific loads are applied.
- **Dynamic**: its main application is in systems where external conditions change over time, producing motion (in structural analysis) or heat flow (in thermodynamics analysis).
- **Modal**: It is widely used in structural analysis to evaluate the effects of vibration on a structure.

In this thesis, only the dynamic and modal approaches will be carried out.

According to [3] several variants of the FEM exist depending on the characteristics of the problem to analyse:

- **Extended FEM**: applied in systems with discontinuities, such as fractures.
- **Generalized FEM**: makes use of advanced *meshless* methods in combination with the traditional ones.
- **Mixed FEM**: employed in problems that involve contact between two moving parts.
- **hp-FEM**: used when the equations have different order depending on the element and thus the mesh needs to be refined on specific places.
- **Galerkin FEM**: which converts a continuous problem, i.e a differential equation in its weak form, to a discrete problem by applying constraints determined by finite element basis functions that are needed to approximate and integrate the internal forces.

The FEM that will be employed in this work is a Galerkin FEM whose basis functions are linear.

2.2 Reduced-Order Methods

A class of approximated methods that is receiving increasing attention in recent years are those combining the FE method at the coarse-scale and Reduced-Order Modeling (ROM) at the fine scale [4]. Because of its relevance within the present work, the basic principles of these approaches - hereafter referred to as FE-ROM methods - are described in what follows.

Like classical model reduction methods for linear modal analysis, FE-ROM methods rely on the approximation of the displacement field of the structure as a linear combination of a few characteristic modes. The distinct feature here is that these modes are not obtained via the modal decomposition analysis, but rather determined from computational experiments.
The matrix of modes is obtained in a process that is performed offline: FE analyses of the structure subjected to representative deformation histories are conducted; and then the set of computed solutions is processed by

dimensionality reduction tools in order to identify and unveil the most statistically dominant displacement modes [5].

In cases where the governing equations feature nonlinear relationships between the state variable and the input parameters, these methods entail two sequential stages [6] to achieve a dimensional reduction: projection onto the reduced basis and approximation of the nonlinear term.

The first stage consists in introducing the approximation of the state variables in the governing equation and subsequently posing the resulting equation in the space spanned by the basis matrix. Galerkin projection of the FE equilibrium equations onto the subspace spanned by these modes leads to a reduced-order model with far fewer equations that the original FE model and thus reduces the computational effort.
To complete the reduction process, the projection has to be accompanied by a second stage that consists on an efficient integration rule, tailored to the physics of the problem: ROM with efficient integration rules are known as Hyperreduced-Order Models (HROM) [7].

Some of the procedures to conduct these second stage are the Empirical Interpolation Method (EIM) [8], [9], the Best Point Interpolation Method (BPIM) [10], the Discrete BPIM [11] or the Missing Point Estimation Method [12].

Nonetheless, the present work is not interested in the construction of the low-dimensional interpolant required in the above-mentioned approaches, and it focuses the attention on solving the balance equations at appropriately selected points. This idea, known as collocation, is proposed in [7] and is based on the idea of approximating the integral of the nonlinear vector rather than approximating the vector itself. Such operation can be performed by either computing a low-dimensional approximation of the integrand or, as it is the case in this thesis, by approximating the integral itself as a weighted sum of the integrand evaluated at optimal sampling points thanks to *cubature* methods - which are similar to the Gauss quadrature of polynomials.

More precisely, the *cubature-based* ROM that will be employed in the present work is the Empirical Cubature Method (ECM), proposed by [13] and which essentially determines, among the integration points of the FE mesh, a reduced set of points and associated positive weights so that the integration error is minimized over a set of representative samples of the integrand. This technique makes use of the Singular Value Decomposition to efficiently perform the dimensionality reduction process, selects the p dominant modes of the problem and finally selects the above-mentioned points by integrating the p dominant modes. According to [13], the integration can be exactly solved with $m = p + 1$ Gauss points.

Chapter 3

Methodology

3.1 Finite Element Method Implications

As it has been briefly introduced in the previous chapters, the solution of this project will require the use of FEMs. This methods need both pre and post-process actions in order to create the mesh of the structure on which the balance equations will be solved, and also to be able to represent and analyse its results. As mentioned, these processes will be carried out with the aid of a software called GiD, which is developed by CIMNE (International Centre of Numerical Methods in Engineering), Barcelona.

Pre-process tasks include the definition of the structure to be analysed, as well as its meshing, material, Neumann boundary conditions, etc. The structure that will be used throughout this project is a simple but legitimate 2D cantilever beam (embedded on one end and free on the other), as exemplified in figure 3.1 whilst its mesh is depicted in figure 3.2.

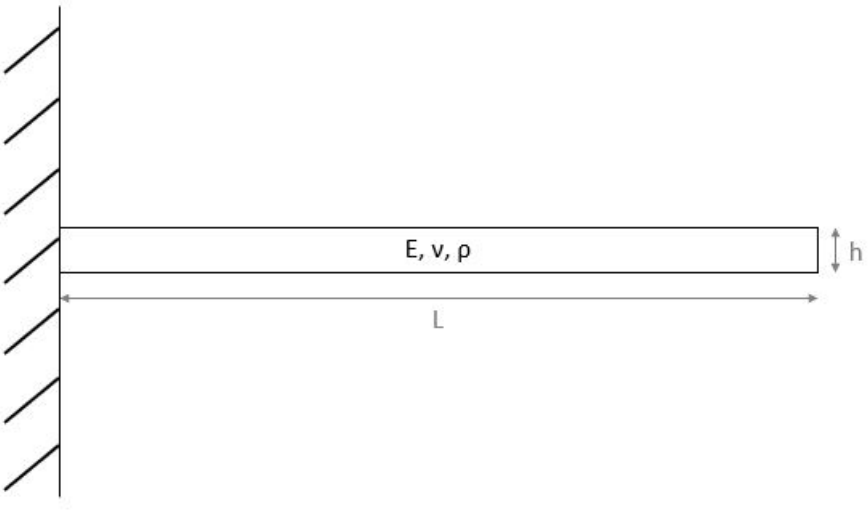

Figure 3.1: Example of a 2D cantilever beam. Its length L is 1 meter, while its height h is just 2 cm. *Source: Own elaboration.*

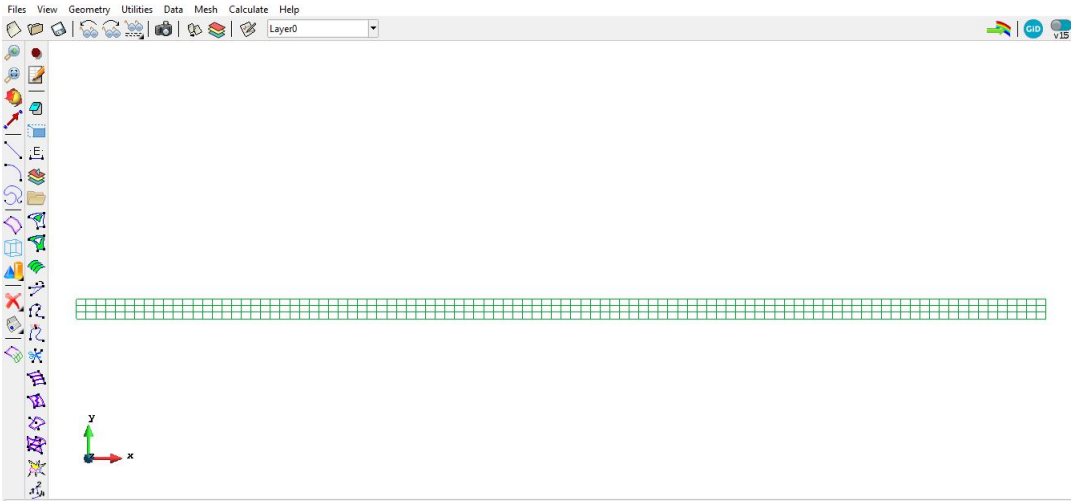

Figure 3.2: Representation of the mesh of the cantilever beam created using GiD.
Source: Own elaboration.

Since one of the main objectives of the present work is to study the response of the structure under the influence of wind gusts, it has been considered that the material that would be the most realistic given such circumstances is aluminium. The wind is a phenomena of interest in the aerospace industry and, as it is widely known, the vast majority of aeronautical structures are mostly made of aluminium.
This material has the following properties:

Property	Young Modulus (E)	Poisson Coefficient (v)	Density (ρ)
Value	70000 MPa	0.33	$2712 \times 10^{-6}\ kg/m^3$

Table 3.1: List of the properties that will be needed for this project studies.

Since it is a cantilever beam, the Neumann boundary conditions have to restrict any displacement and rotation on the embedded end.

As it can be seen in figure 3.1, the finite element mesh is a structured mesh consisting on quadrilateral elements. In the physical domain, a quadrilateral element has four nodes, i.e one for each corner. However, in the FE analysis there are usually more nodes. Depending on the desired degree of accuracy of the FEM, one finite element (FE) may consist on higher nodes. The more nodes there are in an element, the higher accuracy is obtained when solving the FE integrals. Figure 3.3 represents the default case of analysis, in which the FE mesh will have 506 elements of 9 nodes each, thus 1407 nodes.

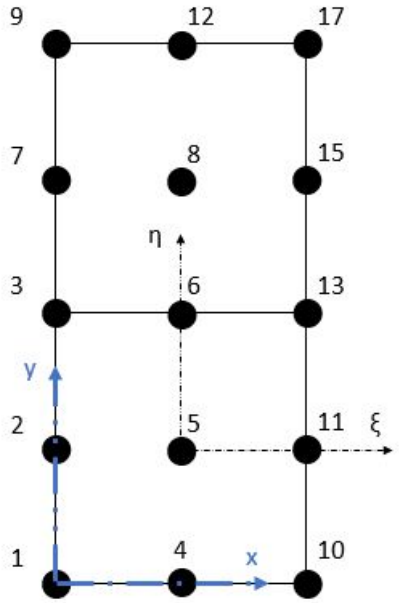

Figure 3.3: Representation of the 9 node quadratic elements that form the mesh.
Source: Own elaboration.

Figure 3.3 shows the order of the nodes according to the criteria that GiD uses by default. This criteria will be crucial to identify every node correctly when understanding the FE code.
ξ and η are the coordinates of the FE parent domain, which are further addressed in chapter 4.

3.2 Work Methodology

The methodology followed throughout the execution of this project has been based on the different work packages exposed in the scope (see section 1.2).

The first step aim is to acquire the necessary background on the structural dynamics field in both the linear and nonlinear regimes, as well as the finite element methods behind them. Furthermore, the student will have to investigate and research on the order reducing methods that exist and some of the ML that they require to decrease the computational cost of those studies.
All the information gathered during the first stage is summarised in chapter 4. This content will serve as a guideline for all the remaining tasks that contribute to make up the final solution.

Once the theoretical framework behind this work is settled, it is time to analyse the FE code that is provided to the student with the objective to conduct this project's studies.
At the beginning of the project, the code is able to obtain the dynamic response in both the linear and nonlinear regime, and is also able to conduct the HROM. However, the code is only prepared for cases where the external force consists on a harmonic and uniformly distributed force with the form:

$$F^{ext}(t) = \bar{F} sin(\Omega t) \tag{3.1}$$

Moreover, the code is only prepared to obtain the analytical solution (i.e the modal decomposition analysis) for the undamped vibration case.

One of the final objectives of this project is to study the dynamic response of a structure subjected to real wind gusts. Those wind gusts will be represented by a Fourier expansion thanks to the FFT algorithm, so all the code adaptations will be carried out with the intention of being able to obtain the temporal evolution of a structure subjected to an external force consisting on a large combination of sines (i.e a Fourier expansion). Moreover, to compare the results with the analytical solution, the code will also have to solve the modal analysis for the damped vibrations produced by this type of force.
To reach that point, the student will conduct several simulations for different types of external forces and boundary conditions (including large strains conditions), which will help to verify that all the necessary adaptations work correctly and to gain confidence with the code.
First of all, the damped case will be solved exclusively for one sine. Afterwards, once everything works, the process will be repeated but with an external force consisting on a combination of 10 sines, which will simulate a truncated Fourier expansion. Furthermore, the student will also study the nonlinear regime by launching different simulations under this condition, and comparing its results with the linear response.
All these simulations and their respective results will be later discussed in chapter 6. As it has been previously advanced, the modal decomposition analysis will be the analytical solution used to understand the precision of the results obtained in the different simulations.

As it has been mentioned, this project seeks to study the response of a structure under the action of the wind, among other objectives. That being said, the code will need an external force function that is able to represent the wind speed along time.
In the real world, wind tends to be rather random and, although there are statistical and complex methods to represent it, those are totally out of this project scope. Instead, the approach that will be performed in this work will be to take real measurements of wind speed in a wind turbine blade and try to obtain a continuous time function that would match with the discrete data. To do that, the FFT algorithm will be used in order to extract a Fourier expansion from the original data, which will be later used to obtain the time expression of the external force that the wind would produce on the structure.

Finally, and once the code works well with the FFT, the student will be able to conduct the final simulation which will give out the dynamic response of the structure exposed to real wind gusts. In this final task, the student will obtain and compare results from 3 different approaches: the FEM, the HROM and the analytical or modal analysis.
Based on these results, the student will discuss and extract some conclusions on the effectiveness and feasibility of the HROM in the field of structural vibrations modelling.

During the entire development of the solution, the student will collect all the necessary information about the different simulations and all the considerations and code modifications associated to each of them.
Given the complexity of the code, this procedure will allow the student to track all the simulations no matter

when they are launched. This way, if any inconsistency is to appear, the student is able to detect its origin in an easier and more comfortable way, and is also capable of retracting his own steps by undoing all the incorrect code modifications.

All these information is gathered with Matlab in a format that has the extension *.mlx*, i.e Live Scripts. This work environment is ideal if one wants to launch different simulations while also writing down some considerations about them that may be relevant in the future.

Chapter 4

Theoretical Framework

Structural dynamics is an engineering field that studies the dynamic behaviour of structures. This dynamic response is caused by one or more external dynamic loads. Dynamic stresses can include people, wind, waves, earthquakes, etc. and can affect any kind of structure. Precisely, one of the goals of this project is to study the response of a structure when submitted to the effect of real wind gusts.

To better understand the methodology that has been carried out to achieve the final solution, this chapter will try to give a background on the theory that surrounds this work.

First of all the physical equation of motion derived from the linear regime problem will be formulated and discussed. Afterwards, the computation formulation and time integration method will be explored and compared with the analytical approach. Then, the same procedure will be followed for the case of nonlinear structural vibrations and, finally, the Reduced Order Models (ROM) and the ML techniques behind them will be introduced.

4.1 Preliminaries

Before beginning with the theoretical framework, this section will expose some of the preliminary notation that will be respected henceforth:

4.1.1 Notation

- $n_{sd} = 2$ or 3, will refer to the space dimension of the problem.
- The concept Degree of Freedom (DOF) refers to the direction in which a node can move. Every node has as many DOFs as dimension has the problem.
- Ω_0 is an open set, representing the physical domain, with piecewise smooth boundary Γ_0, representing the boundaries of the physical domain.
  The sub index 0 indicates the undeformed or initial configuration. Ω_t and Γ_t are the same but in the deformed configuration.

- N and n denote the unit outward vector to Γ_0 and Γ_t respectively.
- In the Finite Element analysis, the sub-indices r will refer to the restricted or prescribed degrees of freedom, while the sub-indices l will represent the unrestricted or free degrees of freedom.
- The Voigt notation avoids repeating the non-diagonal components of a symmetric tensor, with the objective of saving computational effort and avoiding redundancies (see equation 4.1).
  When using this notation, the tensors will be written between braces as:

$$E = \begin{bmatrix} E_{11} & E_{12} & E_{13} \\ E_{12} & E_{22} & E_{23} \\ E_{13} & E_{23} & E_{33} \end{bmatrix} \rightarrow \{E\} = \begin{bmatrix} E_{11} \\ E_{22} \\ E_{33} \\ E_{23} \\ E_{13} \\ E_{12} \end{bmatrix} \tag{4.1}$$

4.1.2 Large Strain Kinematics

- The material or Lagrangian coordinates (X) will refer to a general point in Ω_0, which will be identified with a position vector emanating from the origin of the cartesian coordinates.
  It is important to notice that X includes all the coordinates of the point, and not only the x coordinate.
- The spatial or Eulerian coordinates (x) will denote the coordinates of X but in the deformed configuration Ω_t.
- The displacement field, which will be the solution of the FE analysis, will be represented as:

$$u(X,t) = \phi(X,t) - X \tag{4.2}$$

  Where ϕ is the function that represents the motion from Ω_0 to Ω_t, and t denotes the time, which domain will be $[0,T]$.
- The velocity and acceleration fields:

$$\dot{u}(x,t) = \frac{\partial u}{\partial t}, \quad \ddot{u}(x,t) = \frac{\partial^2 u}{\partial^2 t} \tag{4.3}$$

- The deformation gradient, which identifies the deformation state at any $X \in \Omega_0$, will be expressed as:

$$F = \frac{\partial \phi}{\partial X} = \begin{bmatrix} \frac{\partial \phi_1}{\partial X_1} & \frac{\partial \phi_1}{\partial X_2} & \frac{\partial \phi_1}{\partial X_3} \\ \frac{\partial \phi_2}{\partial X_1} & \frac{\partial \phi_2}{\partial X_2} & \frac{\partial \phi_2}{\partial X_3} \\ \frac{\partial \phi_3}{\partial X_1} & \frac{\partial \phi_3}{\partial X_2} & \frac{\partial \phi_3}{\partial X_3} \end{bmatrix} \tag{4.4}$$

  This second order tensor is used to relate an infinitesimal line segment from the undeformed configuration with an infinitesimal line segment from the deformed configuration:

$$dx = F\, dX \tag{4.5}$$

  From equation 4.2, F can be expressed in terms of the gradient of the displacements as:

$$F = \nabla_0 u + I = \frac{\partial u}{\partial X} + \delta \rightarrow F = \begin{bmatrix} \frac{\partial u_1}{\partial X_1} & \frac{\partial u_1}{\partial X_2} & \frac{\partial u_1}{\partial X_3} \\ \frac{\partial u_2}{\partial X_1} & \frac{\partial u_2}{\partial X_2} & \frac{\partial u_2}{\partial X_3} \\ \frac{\partial u_3}{\partial X_1} & \frac{\partial u_3}{\partial X_2} & \frac{\partial u_3}{\partial X_3} \end{bmatrix} + \begin{bmatrix} 1 & 0 & 0 \\ 0 & 1 & 0 \\ 0 & 0 & 1 \end{bmatrix} \tag{4.6}$$

- The Green-Lagrange strain tensor will be expressed as:

$$E = \frac{1}{2}\left(F^T F - I\right) \tag{4.7}$$

  According to 4.6, E can be expressed as

$$E = \frac{1}{2}\left((\nabla_0 u + I)^T(\nabla_0 u + I) - I\right) = \overbrace{\frac{1}{2}\left(\nabla_0 u^T + \nabla_0 u\right)}^{\nabla_0^s u} + \frac{1}{2}\nabla_0 u^T \nabla_0 u \tag{4.8}$$

4.1.3 Stress Measurements

- The Cauchy stress tensor σ (see [14]), which is used to obtain the traction vector t (force per unit deformed area) in the deformed configuration, will be referenced as

$$t = \sigma n \tag{4.9}$$

- The Kirchhoff stress tensor, τ, is the same as σ, but measured of undeformed area units (force per unit undeformed area):

$$t^0 = \tau n \tag{4.10}$$

  The relation between τ and σ is

$$\tau = detF\ \sigma \tag{4.11}$$

- The first Piola-Kirchhoff stress tensor, P (abbreviated PK1 stress), relates t^0 with the normal of a given surface in the undeformed configuration:

$$t^0 = PN \tag{4.12}$$

And

$$P = \tau F^{-T} \tag{4.13}$$

- The second Piola-Kirchhoff stress tensor (abbreviated PK2 stress), S, relates normals of a given surface in the undeformed configuration to a traction vector T defined in the undeformed configuration as well:

$$T^0 = SN \tag{4.14}$$

S can be related to τ with the following expression:

$$S = F^{-1}\tau F^{-T} \tag{4.15}$$

And thus equation 4.13 can be also expressed as:

$$P = F\ S \tag{4.16}$$

- The elasticity tensor C is used to relate the second Piola-Kirchhoff stress tensor S with the Green-Lagrange strain tensor E.
  In the linear regime and for isotropic materials, the elastic tensor is defined by Hooke's Law and relates the PK2 stresses with the Green-Lagrange strains. This relationship is also know ans the constitutive equation, given by:

$$S = C\ E \tag{4.17}$$

Where C is a fourth order tensor ($n_{sd}^2 \times n_{sd}^2$) that depends on the lame parameters λ and μ, which are functions of the Young's modulus E and the Poisson's coefficient ν.
This tensor will be further discussed in sections 4.2 and 4.3.

4.1.4 Boundary Conditions

- The Dirichlet boundary conditions, which refer to the prescribed displacements on undeformed boundaries $\Gamma^i_{0_u}$ (i going from one to the number of dimensions of the problem n_{sd}), will be expressed as

$$u_i = \bar{u}^i \tag{4.18}$$

- The Neumann boundary conditions, which refer to the prescribed tractions on undeformed boundaries

$\Gamma_{0\sigma}^{i}$, will be expressed as

$$P_{iJ}N_J = \bar{t}_i^0 \tag{4.19}$$

- The initial conditions, i.e at t_0, will be denoted as:

$$u(X,0) = u^0(X), \qquad \dot{u}(X,0) = \mathrm{v}^0(X) \tag{4.20}$$

4.2 Linear Regime: Small Strains

In many structural design problems it can be assumed that $\|E\| << 1$. This is the same hypothesis that holds in the small displacement case, except that, in that case, the hypothesis is formulated in terms of the infinitesimal strain tensor ϵ. It is important to remark that neither follower loads nor rotational frames are considered in the scope of this project.

To address the dynamic problem, it is necessary to introduce the static formulation.

4.2.1 Static Strong Form

In this kind of problems, the motion is considered to be quasi-static, which means that the instantaneous acceleration can be neglected and thus the system will always find itself in physical equilibrium, which is why the problem can be treated statically.

The governing equation and boundary condition, also known as the strong form of the problem or physical system, can be expressed as (indexes i, J take values $1 \dots n_{sd}$, where $n_{sd} = 2$ for 2D problems, and $n_{sd} = 3$ for 3D problems):

$$\text{S.F} \begin{cases} \text{Given } f_i : \Omega_0 \to \mathbb{R}, \bar{u}_i : \Gamma_{0u}^i \to \mathbb{R}, \bar{t}_i^0 : \Gamma_{0\sigma}^i \to \mathbb{R}, & \text{find } u_i : \bar{\Omega}_0 \to \mathbb{R} \text{ such that} \\ \frac{\partial P_{iJ}}{\partial X_J} + f_i = 0, & \text{in } \Omega_0 \\ u_i = \bar{u}_i & \text{on } \Gamma_{0u}^i \\ P_{iJ}N_J = \bar{t}_i^0 & \text{on } \Gamma_{0\sigma}^i \end{cases} \tag{4.21}$$

Where $f_i : \Omega_0 \to \mathbb{R}, i, j = 1, 2 \dots n_{sd}$ denotes the body force per unit volume (see [15], page 121).

4.2.2 Dynamic Strong Form

In the dynamic analysis, the acceleration is indeed considered, which means that one must take the inertial force into account when defining the governing equations. In addition, the physical displacements field $u(X)$, besides of being space dependant, will now also depend on time.
Moreover, it should be noted that, in dynamic analysis, the frictional resistances opposing the motion of the physical system or structure must be also considered. More commonly know as viscous damping terms, they

can be caused by the aerodynamic resistance of the fluid surrounding the structure, internal micro structural movements, etc. These losses are often related to the velocity in a nonlinear way, but, to avoid complexity, the term will be considered linear with velocity through the viscosity parameter $\mu_0 : \Omega_0 \to \mathbb{R}$ (see [16]).

That being said, the strong form of the dynamic approach is derived from the static formulation by adding the following new terms to the body forces per unit volume:

$$f \to f_{static} - \rho_0 \ddot{u} - \mu_0 \dot{u} \tag{4.22}$$

Where $\rho_0 : \Omega_0 \to \mathbb{R}$ represents the density of the surrounding fluid, being the air in this project. Notice that both new body forces involve the minus sign, which means that both of them oppose to the movement and will apparently try to dissipate it.

The strong form can be then written as

$$\text{S.F.} \begin{cases} \text{Given } f_i : \Omega_0 \times [0,T] \to \mathbb{R}, \bar{u}_i : \Gamma^i_{0u} \to \mathbb{R}, \bar{t}^0_i : \Gamma^i_{0\sigma} \times [0,T] \to \mathbb{R}, \quad \text{find} \quad u_i : \bar{\Omega}_0 \times \big[0,T\big] \to \mathbb{R} \text{ such that} \\ \frac{\partial P_{iJ}}{\partial X_J} + f_i - \mu_0 \dot{u}_i = \rho_0 \ddot{u}_i, & \text{in } \Omega_0 \\ u_i = \bar{u}_i & \text{on } \Gamma^i_{0u} \times \big[0,T\big] \\ P_{iJ} N_J = \bar{t}^0_i & \text{on } \Gamma^i_{0\sigma} \times \big[0,T\big] \\ u_i(X,0) = u^0_i(X) & X \in \Omega_0 \\ \dot{u}_i(X,0) = u^0_i(X) & X \in \Omega_0 \end{cases} \tag{4.23}$$

4.2.3 Finite Element Basis Functions

As it has been already mentioned in the state of the art review (see chapter 2), the main objective of any FEM is to solve the differential equations that govern any physical system.
The basis functions that will be used in this work will consist on linear finite element functions or degree one polynomials. For example, for a 1D mesh like the one depicted in figure 4.1, the basis function would be:

$$N(x) = \begin{cases} \frac{x_2 - x}{x_2 - x_1} & \text{if} \quad x \in [x_1, \ x_2] \\ 0 \quad \text{otherwise} \end{cases} \tag{4.24}$$

However, in cases like the one studied in this project, where the dimension is 2, each element has its own origin of coordinates, which do not match with the physical origin of coordinates. The elemental reference system is called the parental domain ξ, (see figure 3.3).
In this case, the mesh is 2D and the shape function:

$$N^e_\xi = [(1-\xi)(1-\eta) \ (1+\xi)(1-\eta) \ (1+\xi)(1+\eta) \ (1-\xi)(1+\eta) \ ] \tag{4.25}$$

To go from one domain to the other:

$$X = N_\xi^e \, X^e \longleftrightarrow X(\xi) = X^e \, N^{eT}(\xi) \tag{4.26}$$

The spatial derivative of this elemental shape function is also of interest when solving the balance equation that appears in the strong form (deduced in the previous section 4.2.2). Nevertheless, one needs to distinguish between the derivative in the parental domain B_ξ^e and the in the physical domain B^e.

$$B_\xi^e = \nabla_\xi N^e = \begin{bmatrix} \frac{\partial N^e}{\partial \xi} \\ \\ \frac{\partial N^e}{\partial \eta} \end{bmatrix} = \frac{1}{4} \begin{bmatrix} -(1-\eta) & (1-\eta) & (1+\eta) & -(1+\eta) \\ \\ -(1-\xi) & -(1+\xi) & (1+\xi) & (1-\xi) \end{bmatrix} \tag{4.27}$$

B^e is also the spatial derivative but, this time, in the physical domain:

$$B^e = \nabla N^e = J^{e-T} \left(\nabla_\xi N^e \right) = J^{e-T} B_\xi^e \tag{4.28}$$

Where J^e is the elemental Jacobian of the domain transformation, which, in 2D cases, can be expressed as follows:

$$J^e = \begin{bmatrix} \frac{\partial \xi}{\partial x} & \frac{\partial \eta}{\partial x} \\ \\ \frac{\partial \xi}{\partial y} & \frac{\partial \eta}{\partial y} \end{bmatrix} \tag{4.29}$$

As it can be seen in figure 4.1, in the 1D case, these functions have their maximum value when x is situated at the node that they represent.

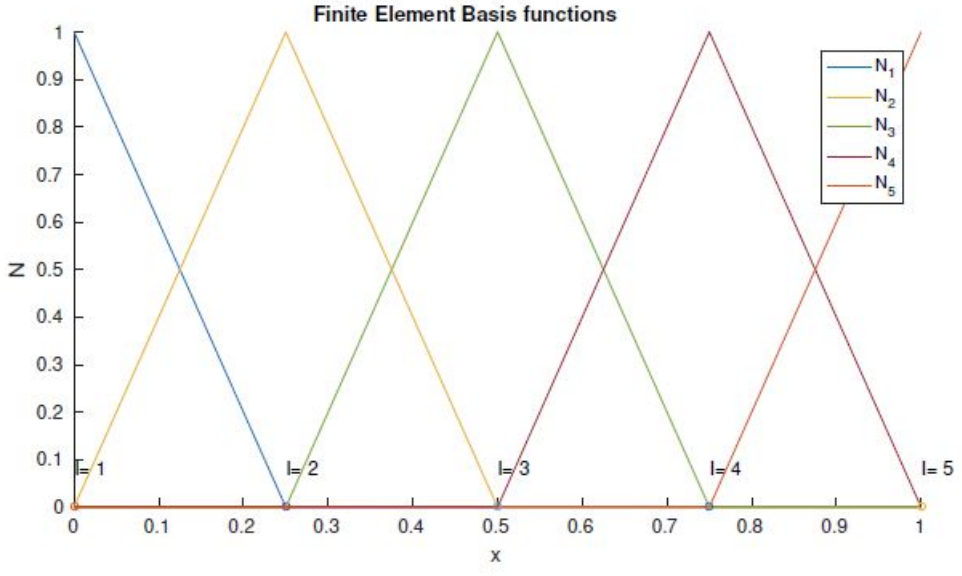

Figure 4.1: Linear basis functions for a 1D structure composed of 5 nodes.
Source: Extracted from [17].

In the 2D case, however, the concept is the same but it is harder to represent. Nevertheless, figure 4.1 can be

understood as the behaviour of N^e when y is maintained constant and x is varied among this dimension.

The essence of these FE basis is to interpolate the displacement coefficient d, that the FEM has solved for every degree of freedom (DOF) from every node of the mesh, to the entire physical domain of the structure.

This way, the solution of the problem will be constructed by a linear combination of these shape functions and the displacement coefficients obtained by the FEM. This construction is also known as trial function vector $u^h(X,t)$, and is expressed as:

$$u(X,t) \approx u^h(X,t) = \sum_{i=1}^{n} N_i(x) d_i(t) = [N_1(x)\ N_2(x)\ ...\ N_n(x)] \begin{bmatrix} d_1(t) \\ d_2(t) \\ ... \\ d_n(t) \end{bmatrix} = N(x)\ d(t) \tag{4.30}$$

4.2.4 Dynamic Weak Form

As it has been shown in figure 4.1, basis functions are only continuous in the vicinity of the node that they are associated to. Taking a look into the strong form of the problem (see balance equation in 4.23), one can spot the presence of the following spatial derivative:

$$\frac{\partial P_{iJ}}{\partial X_J} \tag{4.31}$$

Regarding equations 4.16 and 4.17, the previous expression can be rewritten as:

$$\frac{\partial}{\partial X_J} F_{il} S_{lJ} = \frac{\partial}{\partial X_J} F_{il} C_{lJKL} E_{KL} \tag{4.32}$$

Where the Green-Lagrange strain tensor E depends on the physical displacement u.

If FE analysis is to be conducted, the physical displacement field u has to be substituted by the trial function vector u^h in the balance equation inside the strong form 4.23, which would result in an expression called the residual force $r(X;u;t)$. In this case, the above expression 4.32 will also depend on the basis functions N. Carrying out this spatial derivative would imply deriving N, and that would result on discontinuities at the points where N reaches its maximum.

If the spatial derivative could be avoided, the continuity inconsistencies would not have any repercussion and the differential equation of the strong form would be solvable using the FEM.

The weak form does exactly that by converting the differential equation into an integral form which has a lower order and is usually easier to solve than the strong form. Moreover, when transforming the initial differential equation into an integral, one is also considering the boundary conditions in the same equation thanks to the limits of integration.

This alternative formulation makes use of a mathematical construction called test functions (v^h):

$$v^h(X) = N(X)\, c \tag{4.33}$$

Where N is the vector of FE basis functions and c is a vector of coefficients that has the same dimension as the vector of displacement coefficients d. Furthermore, to respect the prescribed displacements ($\bar{u} = 0$), it is imposed that $c_r = 0$, where r refers to the restricted or prescribed degrees of freedom that are derived from the Neumann boundary conditions.

Understanding the entire mathematical analysis behind the weak form is out of the scope of this work. Nevertheless, according to [18], the weak form is a method that tries to nullify the effect of the residual forces, since, in a real problem, they would be nonexistent.
One can understand the test functions as a tool that guarantees the condition of orthogonality between the residual $r(X;u;t)$ and the real displacement field $u(X,t)$.
Since the trial functions u^h are an approximation of u, the residual will never be strictly equal to zero and that is a condition that must be met, according to the strong form 4.23. The test function vector and its consequent orthogonality condition are the mathematical resources which ensure that the work or energy produced by the residual forces $r(X;u,t)$ will be equal to zero, and thus allow the problem to be solved using the FEM.

The weak form is then obtained by integrating the energy produced by the residual forces and using the test function v^h as a *"trick"* to ensure that this energy will be zero.

Making use of the Divergence Theorem to shift the derivatives on the stresses P_{iJ} to the test functions v_i^h, one can finally obtain the expression of the weak form:

$$\text{W.F.} \begin{cases} \text{Given } f : \Omega_0 \times [0,T] \to \mathbb{R}^{n_{sd}}, \bar{t} : \Gamma_{0\sigma} \times [0,T] \to \mathbb{R}^{n_{sd}}, \\ \text{find } u \in \mathcal{S}^h \left(\text{ with } u(X,0) = u^0, \dot{u}(X,0) = v^0 \right) \text{ so that} \\ \int_{\Omega_0} {v^h}^T \rho_0 \ddot{u} d\Omega_0 + \int_{\Omega_0} {v^h}^T \mu_0 \dot{u} d\Omega_0 + \int_{\Omega_0} \left\{\nabla_0 v^h\right\}^T \{P(u^h)\} d\Omega_0 = \int_{\Omega_0} {v^h}^T f d\Omega_0 + \int_{\Gamma_{0\sigma}} {v^h}^T \bar{t}^0 d\Gamma_0 \quad \forall v \in \mathcal{V}^h \end{cases} \tag{4.34}$$

Where the integrals can be physically understood as, from left to right, the inertia forces, the damping forces, the internal forces, and the external forces (consisting on body and traction forces).

$\mathcal{V}^h$ and $\mathcal{S}^h$ are the finite dimensional space of test functions $v^h(X)$ and trial functions $u^h(X,t)$ respectively.

Expressing the velocity $\dot{u}$ and acceleration $\ddot{u}$ as $\dot{u}^h$ and $\ddot{u}^h$,

$$\frac{\partial u^h(X,t)}{\partial t} = N(X)\dot{d}(t) \quad \text{and} \quad \frac{\partial^2 u^h(X,t)}{\partial t^2} = N(X)\ddot{d}(t) \tag{4.35}$$

Substituting the preceding equation 4.35 as well as equation 4.33 into the weak form 4.34, and factoring out

c^T, one gets:

$$c^T \left(\ddot{d} \int_{\Omega_0} \rho_0 N^T N \, d\Omega_0 + \dot{d} \int_{\Omega_0} \mu_0 N^T N \, d\Omega_0 + \int_{\Omega_0} \{\nabla_0 N\}^T \{P(d)\} d\Omega_0 - \int_{\Omega_0} N^T f \, d\Omega_0 - \int_{\Gamma_{0_\sigma}} N^T \bar{t}^0 \, d\Gamma_0 \right) = 0 \tag{4.36}$$

In the FEM literature, the integrals defined after the weak form expression 4.34, are referred as:

- The global mass matrix M, which forms the global vector of nodal inertia forces $M\ddot{d}$:

$$M = \int_{\Omega_0} \rho_0 N^T N d\Omega_0 \tag{4.37}$$

- The global damping matrix D, which forms the global vector of nodal damping forces $D\dot{d}$:

$$D = \int_{\Omega_0} \mu_0 N^T N d\Omega_0 \tag{4.38}$$

- The global vector of nodal internal forces $\hat{F}$:

$$\hat{F}(d) = \int_{\Omega_0} B^T \{P(d)\} d\Omega_0 \tag{4.39}$$

- Global vector of nodal external forces F^{ext}:

$$F^{ext} = \int_{\Omega_0} N^T f d\Omega_0 + \int_{\Gamma_{0_\sigma}} \bar{N}^T \bar{t}^0 d\Gamma_0 \tag{4.40}$$

Introducing all these global nodal forces into expression 4.36, one gets:

$$c^T \left(M\ddot{d} + D\dot{d} + \hat{F}(d) - F^{ext} \right) = 0 \tag{4.41}$$

In order for c^T to vanish from the equation, one must work only with $c \neq c_r$, or in other words, with the unrestricted or free DOFs (c_l). Since c and d have the same dimension, d will also represent the free DOFs (d_l).

Applying these details to equation 4.41, yields the famous semi-discrete equation of motion used in structural dynamic analysis with its corresponding initial conditions and boundary conditions:

$$\boxed{M_l\ddot{d} + D_l\dot{d} + \hat{F}_l(d) = F_l^{ext} \begin{cases} d_l(0) = u_l^0 \quad \dot{d}_l(0) = \mathrm{v}_l^0 \\ d_\mathrm{r}(t) = \overline{u}(t) \end{cases}} \tag{4.42}$$

4.2.5 Gauss Quadrature

Before going through how to solve the previous semi-discrete equation of motion in the time domain, one must understand how to integrate a function, say f, over the physical domain of a given finite element in the

undeformed geometry Ω_0^e:

$$I = \int_{\Omega_0^e} f \, d\Omega_0 \tag{4.43}$$

Since the finite element domain is represented by the parent domain, the preceding integral must be solved using the change of variable 4.26 to go from the physical to the parent domain. Thus

$$I = \int_{\Omega_0^e} f \, d\Omega_0 = \int_{\Omega_{0_\xi}} J^e(\xi) f(\xi) \, d\Omega_{0_\xi} \tag{4.44}$$

Where $d\Omega_{0_\xi} = d\xi d\eta$ (for 2D) and $J^e(\xi)$ is the elemental Jacobian of the transformation defined in equation 4.29.

The Gauss Quadrature is a method of integration that seeks to find a set of m points in the parent domain (ξ_g) and their corresponding weights ω_g such that the integral in equation 4.44 can be approximated as:

$$\int_{\Omega_{0_\xi}} J^e(\xi) f(\xi) \, d\Omega_{0_\xi} \approx \sum_{g=1}^{m} \omega_g J^e(\xi_g) f(\xi_g) \tag{4.45}$$

According to [19], Gauss quadrature gives an exact result if f is a polynomial. Moreover, it has been demonstrated that m Gauss points integrate exactly a polynomial of order $p \leq 2m - 1$.

However, if the function does not meet this requirement, Gauss Quadrature yields an approximate result as represented in the preceding equation. Accuracy improves as more Gauss points are used.

In conformity to what has been discussed in the previous section, all the FE integrals represented in equations 4.37 to 4.40, will be solved via Gauss Quadrature, hence computing $N_\xi(\xi_g)$ and $B_\xi(\xi_g)$ for every Gauss point. The coordinates of the Gauss points ξ_g and their corresponding weights ω_g are found in [20], and depend on the degree of the polynomial f.

Having reach that point, one is faced with n_{el} finite elements, each one of them having m Gauss points and each point having 2 DOFs. To express the FE matrices in a more compact way, the element-free notation is briefly introduced, since it will be necessary for upcoming sections.

The main idea behind it is to create a matrix that includes the information in all of the m Gauss points of an element e. Thus, the element-free matrices for N_ξ, B_ξ, ω_ξ and PK1 stresses are defined as:

$$\mathcal{N}^e = \left[N^e_{\xi_1} N^e_{\xi_2} \dots N^e_{\xi_m}\right] \rightarrow \mathcal{N} = \sum_{e=1}^{n_{el}} \mathcal{N}^e L^e \tag{4.46}$$

Where L^e is boolean connectivity matrix commonly used in FEMs to relate the element nodal variables e with the global vector.

$$\mathcal{B}^e = \left[B^e_{\xi_1} B^e_{\xi_2} \dots B^e_{\xi_m}\right] \rightarrow \mathcal{B} = \sum_{e=1}^{n_{el}} \mathcal{B}^e L^e \tag{4.47}$$

$$\mathcal{W}^e = \begin{bmatrix} \omega_1 J_1^e I & 0 & \dots & 0 \\ 0 & \omega_2 J_2^e I & \dots & 0 \\ \vdots & \vdots & \ddots & \vdots \\ 0 & 0 & \dots & \omega_m J_m^e I \end{bmatrix} \rightarrow \mathcal{W} = diag\left(\mathcal{W}^1,\ \mathcal{W}^2,\ \dots\ , \mathcal{W}^{n_{el}}\right) \tag{4.48}$$

$$\mathcal{P}^e = \begin{bmatrix} \{P(d^e)\}_{\xi_1} \\ \{P(d^e)\}_{\xi_2} \\ \vdots \\ \{P(d^e)\}_{\xi_m} \end{bmatrix} \rightarrow \mathcal{P} = \begin{bmatrix} \mathcal{P}^1 \\ \mathcal{P}^2 \\ \vdots \\ \mathcal{P}^{n_{el}} \end{bmatrix} \tag{4.49}$$

4.2.6 Newmark-Bossak's Time Integration Scheme

As it has been shown, the FEM objective is to solve the semi-discrete equation of motion 4.42 for any moment in a desired time interval $[0,\ T]$.

The essence of any integration scheme used in a FEM is to solve the motion equation at every moment in time, given the value of some variables in the corresponding moment. As it was done with the physical domain, the time domain also needs to be divided into sub-intervals or infinitesimal time steps, so that the motion equation can be solved at each of them. The more number of divisions, the more accurate the result will be.

The first step in the integration method is to divide the interval $[0,\ T]$ into n_{steps}.

Considering that $\dot{d}$ and $\ddot{d}$ refer to the velocity (v) and the acceleration (a) respectively, the residual of the semi-discrete motion equation at the end of any interval $[t_n,\ t_{n+1}]$, can be written as:

$$R_l(d) = M_l \mathrm{a}^{n+1} + D_l \mathrm{v}^{n+1} + \hat{F}_l(d) - F_l^{ext}(t_{n+1}) \tag{4.50}$$

As mentioned, the aim of any time integration scheme is to solve the system of equations $R_l = 0$ at a given time t_{n+1}, i.e find the nodal displacement vector at that time, d^{n+1}. The inputs that are used to solve such system are the nodal external forces vector at time t_{n+1} $(F_l^{ext}(t_{n+1}))$, the prescribed displacements $\bar{u}(t_{n+1})$ and the kinematic variables in the previous step t_n, d^n, v^n and a^n.

There are different kinds of integration methods addressed in chapter 5, but the one that will be carried out in this work is the Newmark-Bossak's method.

The acceleration and velocity expressions invloved in this method will be the same as the ones that are defined in the implicit Newmark β-methods [15].

One the one hand, the acceleration will be computed as follows:

$$\mathrm{a}^{n+1} = \frac{1}{\beta \Delta t_{n+1}^2} \left(d^{n+1} - \tilde{d}^{n+1} \right) \quad \beta > 0 \tag{4.51}$$

Where

$$\tilde{d}^{n+1} = d^n + \Delta t_{n+1} \mathrm{v}^n + \frac{\Delta t_{n+1}^2}{2} (1 - 2\beta) \mathrm{a}^n \tag{4.52}$$

On the other hand, the velocity will be represented as:

$$\mathrm{v}^{n+1} = \tilde{\mathrm{v}}^{n+1} + \gamma \Delta t_{n+1} \mathrm{a}^{n+1} \quad \text{where} \quad \tilde{\mathrm{v}}^{n+1} = \mathrm{v}^n + (1 - \gamma) \Delta t_{n+1} \mathrm{a}^n \tag{4.53}$$

β and γ are scalar parameters which respectively ensure the stability of the algorithm and numerically take the damping condition into account.

Since the main unknown of the FEM is the nodal displacements vector d, it is convenient to express v^{n+1} in terms of d^{n+1}. Substituting equation 4.51 into the preceding equation 4.53, yelds:

$$\mathrm{v}^{n+1} = \frac{\gamma}{\beta \Delta t_{n+1}} d^{n+1} + \left(\tilde{\mathrm{v}}^{n+1} - \frac{\gamma}{\beta \Delta t_{n+1}} \tilde{d}^{n+1} \right) \tag{4.54}$$

The Newmark-Bossak algorithm differs form the mentioned implicit Newmark β-methods with the fact that it uses a third parameter α_b, called the Bossak integration parameter, to obtain a second order scheme of integration. This parameter, as discussed in [21], enables the capturing of the damping effect in the higher modes of vibration, without compromising the accuracy.

Following this integration scheme, the residual in equation 4.50 is written as:

$$R_l(d) = (1 - \alpha_b) M_l \mathrm{a}^{n+1} + \alpha_b M_l \mathrm{a}^n + D_l \mathrm{v}^{n+1} + \hat{F}_l(d) - F_l^{ext}\left(t_{n+1}\right) \tag{4.55}$$

Combining equations 4.51 and 4.54 into the previous residual expression yields:

$$R_l(d) = (1 - \alpha_b)\, M_l \left(\frac{1}{\beta \Delta t_{n+1}^2} d - \frac{1}{\beta \Delta t_{n+1}^2} \tilde{d}^{n+1} \right) + \alpha_b M_l \mathrm{a}^n + D_l \left(\frac{\gamma}{\beta \Delta t_{n+1}} d - \tilde{\mathrm{v}}^{n+1} \right) + \hat{F}_l(d) - F_l^{ext}\left(t_{n+1}\right) \tag{4.56}$$

Gathering all the terms,

$$R_l(d) = \left(\frac{1 - \alpha_b}{\beta \Delta t_{n+1}^2} M_l + \frac{\gamma}{\beta \Delta t_{n+1}} D_l \right) d + \hat{F}_l(d) - M_l \left(\frac{1 - \alpha_b}{\beta \Delta t_{n+1}^2} \tilde{d}^{n+1} - \alpha_b \mathrm{a}^n \right) + D_l \tilde{\mathrm{v}}^{n+1} + F_l^{\mathrm{ext}}\left(t_{n+1}\right) \tag{4.57}$$

For the sake of simplicity, the above residual is said to consist of four different nodal force vectors, where the nodes only refer to the ones containing one or more unrestricted DOFs (l):

- The nodal vector of internal forces $\hat{F}_l$.
- The nodal vector of external forces F_l^{ext}.

- The nodal vector of displacement-dependant forces, $\hat{F}_l^{nb}$, which can be expressed as:

$$\hat{F}_l^{nb}(d) = \left(\frac{1-\alpha_b}{\beta\Delta t_{n+1}^2} M_l + \frac{\gamma}{\beta\Delta t_{n+1}} D_l\right) d \tag{4.58}$$

- And the displacement-independent forces, F_l^{enb}:

$$F_l^{enb} = M_l \left(\frac{1-\alpha_b}{\beta\Delta t_{n+1}^2} \tilde{d}^{n+1} - \alpha_b \mathrm{a}^n\right) + D_l \tilde{\mathrm{v}}^{n+1} \tag{4.59}$$

Thus, the Newmark-Bossak scheme is the same as the implicit Newmark β-method, but adding the terms $\hat{F}_l^{nb}$ and F_l^{enb}:

$$R_l(d) = \left(\hat{F}_l^{nb}(d) + \hat{F}_l(d)\right) - \left(F_l^{enb} + F_l^{ext}\left(t_{n+1}\right)\right) \tag{4.60}$$

According to [22], to achieve an unconditional stability, capture the maximum amount of high-frequency dissipation, and maintain the second order accuracy, one must set the Newmark-Bossak parameters as follows:

$$\begin{aligned} \alpha_b &\leq 0 \\ \gamma &= \tfrac{1}{2} - \alpha_b \\ \beta &= \tfrac{1}{4}\left(1-\alpha_b\right)^2 \end{aligned} \tag{4.61}$$

In this work, α_b is set to -1/3 and will be varied on the go if necessary.

4.2.7 Newton-Raphson's Method

The Newmark-Bossak's leaves one with a nonlinear equation in the unknown d_l. Thus, the Newton-Raphson algorithm is brought into light in order to complement the Newmark-Bossak, by facilitating the convergence of the nonlinear expression.

This numerical algorithm consists on an iterative method which linearly approximates a nonlinear system and solves it at each iteration, updating the tentative solution until a convergence threshold is met.

The statement consists on, as in the Newmark-Bossak case, computing $d_l(t_{n+1})$ given the initial conditions at time step n, as well as the prescribed displacements $d_r(t_{n+1})$ and the external force vector $F^{ext}(t_{n+1})$. Nevertheless, the system of equations to be solved in every iteration k is now linear:

$$R_l\left(d_l^{(k)}\right) + \left[\frac{\partial R_l}{\partial d_l}\right]_{d_l^{(k)}} \left(d_1^{(k+1)} - d_l^{(k)}\right) = 0 \tag{4.62}$$

Where $d_1^{(0)} = d_l\left(t_n\right)$

Notice that, when the unknowns obtained in two successive iterations are the same, the residual will be equal to zero, as desired. Since computationally speaking, the previous statement is not possible, a convergence tolerance is needed. This threshold is the the absolute difference between d_l^{k+1} and d_l^k, and will be set to

10^{-10}.

Considering that $d_l = \mathbb{P}_l d$, and $\boldsymbol{d} = \mathbb{P}_l^T d_l$, (where $\mathbb{P}_l$ is the assembly operator that identifies the global unrestricted DOFs), and making use of the chain rule, the Jacobian matrix $(\partial R_l / \partial d_l)$ is rewritten as:

$$\frac{\partial R_l}{\partial d_l} = \frac{\partial \mathbb{P}_l R}{\partial d} \frac{\partial d}{\partial d_l} = \mathbb{P}_l \overbrace{\frac{\partial R}{\partial d}}^{K} \mathbb{P}_l^T = K_{ll} \tag{4.63}$$

Where K is the global stiffness matrix of the system, which, in the Newmark-Bossak case, is equal to

$$K_{ll} = \frac{\partial \hat{F}_l^{nb}}{\partial d_l} + \frac{\partial \hat{F}_l}{\partial d_l} \tag{4.64}$$

Making use of equation 4.39 and the derivative of expression 4.58, one can write the expression of K as:

$$K_{ll} = \int_{\Omega_0} B^T \frac{\partial \{P\}}{\partial d} \, d\Omega_0 + \left(\frac{1 - \alpha_b}{\beta \Delta t_{n+1}^2} M_l + \frac{\gamma}{\beta \Delta t_{n+1}} D_l \right) \tag{4.65}$$

Where

$$\frac{\partial \{P\}}{\partial \{F\}} = \{\tilde{C}\} \tag{4.66}$$

With that expression in mind and applying the chain rule:

$$\frac{\partial \{P\}}{\partial \{F\}} \frac{\partial \{F\}}{\partial d} = \{\tilde{C}\} B \tag{4.67}$$

According to equation 4.6, the deformation gradient F and its derivative can be written in terms of the FE shape functions as:

$$\{F\} = \frac{\partial u}{\partial X} + \delta = \frac{\partial}{\partial X} N(X) d + \delta = B(X) d + \delta \rightarrow \frac{\partial \{F\}}{\partial d} = B(X) \tag{4.68}$$

Finally, K can be rewritten as follows:

$$K_{ll} = \int_{\Omega_0} B^T \{\tilde{C}^{mat}\} B \, d\Omega_0 + \left(\frac{1 - \alpha_b}{\beta \Delta t_{n+1}^2} M_l + \frac{\gamma}{\beta \Delta t_{n+1}} D_l \right) \tag{4.69}$$

In the small strains regime, $\tilde{C}$, which will be further explained in section 4.3, can be understood as the rotated elastic tensor C. Therefore, in this regime, $\tilde{C}$ only depends on the material and thus $\tilde{C} = \tilde{C}^{mat}$.
As mentioned in the preliminaries (see section 4.1), when the small strains or linear hypothesis is applied and

the material is isotropic, C is linear and defined by Hooke's Law (2D):

$$C = \begin{bmatrix} \lambda + 2\mu & \lambda & 0 & 0 \\ \lambda & \lambda + 2\mu & 0 & 0 \\ 0 & 0 & \mu & 0 \\ 0 & 0 & 0 & \mu \end{bmatrix} \tag{4.70}$$

The lame parameters λ and μ are represented by the following expressions:

$$\lambda = \frac{v\mathrm{E}}{(1+v)(1-2v)} \quad \text{and} \quad \mu = G = \frac{\mathrm{E}}{2(1+v)} \tag{4.71}$$

Where G is the shear modulus of the material.

However, the convergence of the Newton-Raphson method is directly linked with the positive definiteness of K. As it will be later discussed in section 4.3, there is sometimes the possibility that K is non-positive definite, which, physically, can be interpreted as the initiation of buckling instabilities.

4.3 Nonlinear Regime: Large Strains

In the small strain regime, the strain is measured by the Green-Lagrange expression in 4.7, while the stresses are defined by the PK2 equation in 4.15. Under this hypothesis, $\tilde{C}^{mat}$, which is the derivative of the PK1 stresses P with respect to the deformation gradient F, is linear. As mentioned, this tensor is related to the elastic tensor defined by the Hooke's Law (see equation 4.70).
This relation can be expressed as follows [23]:

$$\{C^{mat}\} = T(F)\{C\}T(F)^T \tag{4.72}$$

Where C is the Hookean constitutive elastic tensor, and T is the matrix that relates the PK1 and PK2 stresses:

$$\{P\} = T(F)\{S\} \tag{4.73}$$

This expression is the same as the one given in the preliminaries (see equation 4.16 in section 4.1.3). However, in FE analysis, it is usual to write symmetric tensors, like the ones representing the PK1 and PK2 stresses, in what is called the Voigt notation (see equation 4.1).
$T(F)$ is then the deformation gradient F, but in Voigt notation. With such rearrangement, equation 4.16 can be transformed into the preceding equation 4.73.

In the small strains regime, when F is not very large, T plays the role of a rotation matrix and thus, as it has been previously discussed, $\tilde{C}^{mat}$ is the rotated Hookean constitutive elastic tensor C.

Nevertheless, there are different conditions that can manifest in the real world and which tend to be nonlinear.

On one side, not all materials are isotropic. In this case, Hooke's Law is not applicable anymore, since the constitutive equation that relates the stresses with the strains is not linear.
On the other side, the circumstances introduced at the end of the previous section can also manifest. When a structure has to deal with large strains, the undeformed and deformed configurations differ significantly from one another. In this case the deformed geometry is really different from the original, which translates into a variation of the constitutive properties of the material, such as density or stiffness.

For the sake of simplicity and taking into account that the objective of this work is to get introduced to the nonlinear regime, the material will be maintained isotropic and the only constitutive property that will be affected due to large strains will be the stiffness.
This way, $\tilde{C}$ will now depend not only on the material but also on the geometry:

$$\tilde{C} = \tilde{C}^{mat} + \tilde{C}^{geo} \tag{4.74}$$

The new term ($\tilde{C}^{geo}$), is responsible for the non-linearity and depends on the geometry of the structure.

The nonlinear term of $\tilde{C}$ only depends on the PK2 stress tensor S. In 2D, the expression of $\tilde{C}^{geo}$ is expressed as (Voigt notation on the left and standard notation on the right):

$$\{\tilde{C}^{geo}\} = \begin{bmatrix} \{S\}_1 & 0 & \{S\}_3 & 0 \\ 0 & \{S\}_2 & 0 & \{S\}_3 \\ \{S\}_3 & 0 & \{S\}_2 & 0 \\ 0 & \{S\}_3 & 0 & \{S\}_1 \end{bmatrix} = \begin{bmatrix} S_{11} & 0 & S_{12} & 0 \\ 0 & S_{22} & 0 & S_{12} \\ S_{12} & 0 & S_{22} & 0 \\ 0 & S_{12} & 0 & S_{11} \end{bmatrix} \tag{4.75}$$

As it was previously anticipated in section 4.2.7, the nonlinear regime can result on a non-positive definteness of the stiffness matrix K. $\tilde{C}^{mat}$ is always invariably positive definite, whereas the $\tilde{C}^{geo}$ can sometimes be non-positive definite. As explained, the physical interpretation behind $\tilde{C}^{geo}$ being non-positive definite is related to buckling conditions. However, studying the buckling phenomena is out of the scope of this project and thus, all the simulations conducted under the large strains regime will be far away from this condition.

That being said, the FEM used to solve the large strains simulations will be the same as the small strains, except for the computation of the stiffness matrix K, which will as well have a new nonlinear term:

$$K_{ll} = \int_{\Omega_0} B^T \{\tilde{C}\}^{mat} B \, d\Omega_0 + \int_{\Omega_0} B^T \{\tilde{C}\}^{geo} B \, d\Omega_0 + \left(\frac{1-\alpha_b}{\beta \Delta t_{n+1}^2} M_l + \frac{\gamma}{\beta \Delta t_{n+1}} D_l \right) \tag{4.76}$$

4.4 Modal Decomposition Analysis

So far, the theory behind the FEM in both the linear and nonlinear regimes has been established. However, if one wants to compare the results obtained from those methods with the ones dictated by the continuum mechanics strain theory, it is necessary to solve the semi-discrete equation of motion 4.42 analytically, rather than numerically.

The modal decomposition analysis is a very useful tool to analyse a dynamic system under vibration. This method studies the dynamic behaviour of the structure by formulating the mathematical model with natural frequencies, damping factors and natural modes of vibration.
It solves the eigenvalue problem detailed in section 4.4.1 to extract the different manners in which the structure can vibrate (natural modes), as well as the predominance of each and every one of them and their vibrating natural frequency. The natural modes and their respective frequency of the present cantilever beam can be found in the first section of the Annexes document.

In this sense, it is necessary to conduct a change of variable in the semi-discrete equation of motion 4.42. The nodal displacements vector d, which was the unknown to solve in the FEM, is replaced by $\phi_i q_i(t)$, where ϕ_i denotes the *i-th* vector of mode shapes and $q_i(t)$ is a temporal function that represents the amplitude at which the *i-th* mode manifests along time.
One of the advantages of the modal decomposition analysis is the uncoupling of equations, which enables a better understanding of the vibration of a structure. Furthermore, thanks to the uncoupling, the solution of the problem can be regarded as a combination of natural modes and their respective amplitudes:

$$d = \sum_{i=1}^{n_{modes}} \phi_i q_i(t) = \phi_1 q_1(t) + \phi_2 q_2(t) + ...\phi_{n_{modes}} q_{n_{modes}}(t) \tag{4.77}$$

By conducting the mentioned replacement, one is able to move from a discrete solution to a continuous one, which means that now equation 4.42 is an second order Ordinary Differential Equation (ODE) of the form:

$$M\left(\phi_i \frac{d^2 q_i(t)}{dt^2}\right) + D\left(\phi_i \frac{dq_i(t)}{dt}\right) + K\phi_i q_i(t) = F^{ext}(t) \tag{4.78}$$

Depending on the terms that one considers inside the preceding equation, there are different types of modal analysis, some of which are relevant for this project.
On the one hand, the case in which the external force is not considered ($F^{ext} = 0$) is known as free vibration, whereas the opposite case is referred as forced vibration.
On the other, if the damping effect ($D = 0$) is neglected, one is faced with an undamped vibration.

In order to extract the natural modes and frequencies of a structure, the free undamped vibration problem is to be solved. Nevertheless, since undamped vibrations are an ideal phenomena and this project's intention is to simulate the real response of a structure, the simulations will be based on the forced damped vibrations problem, since they must consider the damping effects as well as the external forces that produce such response.

4.4.1 Free Undamped Vibrations

The ODE that has to be solved in this type of problem is

$$M\left(\phi_i \frac{d^2 q_i(t)}{dt^2}\right) + K\phi_i q_i(t) = 0 \rightarrow M\phi_i \ddot{q}_i + K\phi_i q_i = 0 \tag{4.79}$$

If one analyses this kind of ODE for scalar values instead of matrices, the solution of this equation has the following form

$$q_i^z(t) = A_i cos(\omega_i t) + B_i sin(\omega_i t) \tag{4.80}$$

Thus, returning to the free undamped vibration ODE 4.79 and substituting the second derivative of $q_i(t)$,

$$(-\omega_i^2 M + K)\phi_i q_i(t) = 0 \rightarrow (-\omega_i^2 M + K)\phi_i = 0 \tag{4.81}$$

One is faced with an eigenvalue problem discussed in [24], which solutions of interest are the non-trivial solutions. These consist on an eigenvalue and an eigenvector, which, physically, respectively correspond to a natural frequency (ω_i) and its associated mode of vibration (ϕ_i).
These non-trivial solution satisfy:

$$\omega_i M\phi_i = K\phi_i \quad \text{and} \quad \phi^T M\phi = I \tag{4.82}$$

Moreover, eigenvectors are orthogonal with respect to M and K.

Multiplying equation 4.79 by ϕ^T, and according to the normalization of ϕ described in 4.82, yields:

$$\ddot{q}_i + \phi_i^T K\phi_i \; q_i = 0 \tag{4.83}$$

Moreover, multiplying the first condition in 4.82 by ϕ^T, one gets:

$$\omega^2 = \phi^T K\phi \tag{4.84}$$

With this final consideration, the uncoupled ODE that governs the free undamped vibrations problem, has the following form:

$$\ddot{q}_i + \omega_i^2 q_i = 0 \begin{cases} q_i(0) = q_i^0 = \phi_i^T M d^0 \\ \dot{q}_i(0) = \dot{q}_i^0 = \phi_i^T M \dot{d}^0 \end{cases} \qquad i = 1, 2, 3 \; ... \; n_{modes} \tag{4.85}$$

Using the undetermined coefficients method and solving with generic initial conditions for constants A_i and B_i in equation 4.80, the analytical solution of the free undamped vibrations (fu) problem is:

$$\boxed{q_i^{fu} = q_i^0 cos(\omega_i t) + \frac{\dot{q}_i^0}{\omega_i} sin(\omega_i t) \rightarrow d^{fu} = \sum_{i=1}^{n_{modes}} \phi_i q_i^{fu}(t)} \tag{4.86}$$

4.4.2 Forced Damped Vibrations

As it will be later discussed in chapter 5, to be able to maintain the uncoupling of the modal analysis in the case of damped vibrations, the damping matrix D will be constructed according to the Rayleigh damping hypothesis:

$$D = \bar{\alpha}M + \bar{\beta}K \tag{4.87}$$

With that in mind, the differential equation for the forced damped vibrations problem stands as:

$$M\ddot{d} + \left(\bar{\alpha}M + \bar{\beta}K\right)\dot{d} + Kd = F^{ext}(t) \tag{4.88}$$

Applying the change of variable discussed in the previous section and multiplying the preceding equation by ϕ_i^T yields:

$$\begin{gathered}\overbrace{\phi_i^T M \phi_i}^{I}\ddot{q}_i + \left(\bar{\alpha}\overbrace{\phi_i^T M \phi_i}^{I} + \bar{\beta}\overbrace{\phi_i^T K \phi_i}^{\omega_i^2}\right)\dot{q}_i + \overbrace{\phi_i^T K \phi_i}^{\omega_i^2} q_i = \phi_i^T F^{ext}(t) \\ \downarrow \\ \ddot{q}_i + \left(\bar{\alpha} + \bar{\beta}\omega_i^2\right)\dot{q}_i + \omega_i^2 q_i = \phi_i^T F^{ext}(t)\end{gathered} \tag{4.89}$$

The damping ratio $\bar{\xi}_i$ is defined by:

$$\bar{\xi}_i = \frac{1}{2\omega_i}\left(\bar{\alpha} + \bar{\beta}\omega_i^2\right) \rightarrow 0 \leq \bar{\xi}_i < 1 \tag{4.90}$$

The forced damped vibrations ODE can be finally stated in terms of $\bar{\xi}_i$ and taking the initial conditions into account:

$$\boxed{\ddot{q}_i + 2\bar{\xi}_i\omega_i\dot{q}_i + \omega_i^2 q_i = \phi_i^T F^{ext}(t) \begin{cases} q_i(0) = q_i^0 = \phi_i^T M d^0 \\ \dot{q}_i(0) = \dot{q}_i^0 = \phi_i^T M \dot{d}^0 \end{cases} \quad i = 1, 2 \ldots n_{modes}} \tag{4.91}$$

The homogeneous solution $(q_i^z(t))$ of this ODE corresponds to the free damped vibrations (fd) problem, since it must be imposed that $F^{ext} = 0$. This solution is defined in equation 4.93, where the natural frequency of damped vibration $\bar{\omega}_i$ is expressed as (see [25]):

$$\bar{\omega}_i = \omega_i\sqrt{1 - \bar{\xi}_i^2} \tag{4.92}$$

$$q_i^z(t) = q_i^{fd}(t) = e^{-\bar{\xi}_i\omega_i t}\left(q_i^0 cos(\bar{\omega}_i t) + \frac{\dot{q}_i^0 + \bar{\xi}_i\omega_i q_i^0}{\bar{\omega}_i} sin(\bar{\omega}_i t)\right) \rightarrow d^{fd} = \sum_{i=1}^{n_{modes}} \phi_i q_i^{fd}(t) \tag{4.93}$$

The particular solution $q_i^p(t)$ will depend on the type of external force that is applied to the structure. In this project's study, the external forces that have been considered are mainly sinusoidal functions.

The analytical solution of the forced damped vibrations problem (Fd) is the sum of the homogeneous and the particular solutions. However, $q_i^z(t)$ must have a generic expression different from $q_i^{fd}(t)$ since the evaluation

in the initial conditions will also depend on the expression of $q_i^p(t)$. This way:

$$q_i^{Fd}(t) = e^{-\bar{\xi}_i\omega_i t}\left(A_i cos(\bar{\omega}_i t) + B_i sin(\bar{\omega}_i t)\right) + q_i^p(t) \tag{4.94}$$

In what follows, the particular solutions for different types of $F^{ext}(t)$ will be detailed. These solutions have been computed solving ODE 4.94 using the method of the undetermined coefficients and, for reasons of simplicity, considering that the initial conditions are zero ($q_i^0 = \dot{q}_i^0 = 0$).

As explained in this thesis' methodology, (see section 3.2), the explored external forces are uniformly distributed forces formed by one single sine or by a combination of them.

Harmonic Force

These functions take the form:

$$F^{ext}(t) = \bar{F} sin\left(\Omega t + \varphi\right) \tag{4.95}$$

According to equation 4.91, F^{ext} has to be multiplied by ϕ_i^T. Thus,

$$\phi_i^T F^{ext}(t) = \overbrace{\phi_i^T \bar{F}}^{f_i} sin\left(\Omega t + \varphi\right) = f_i\ sin\left(\Omega t + \varphi\right) \tag{4.96}$$

Where f_i is the force amplitude projected into the *i-th* mode shape.
The particular solution of equation 4.91 for this kind of force results in:

$$q_i^p(t)|_{Sin} = \overbrace{\frac{f_i}{\omega_i^2}\frac{1}{\left(1-\bar{\rho}_i^2\right)^2 + \left(2\bar{\xi}_i\bar{\rho}_i\right)^2}}^{q_i^{max}|_{Sin}}\left[\left(1-\bar{\rho}_i^2\right) sin(\Omega t + \varphi) - 2\bar{\xi}_i\bar{\rho}_i\ cos(\Omega t + \varphi)\right] \tag{4.97}$$

Where q_i^{max} is the maximum amplitude that the *i-th* mode of vibration will reach, and $\bar{\rho}_i$ is the relation between the external frequency Ω and ω_i:

$$\bar{\rho}_i = \frac{\Omega}{\omega_i} \tag{4.98}$$

Constants A_i and B_i take the form:

$$\begin{aligned} A_i|_{Sin} &= q_i^{max}\left(2\bar{\xi}_i\bar{\rho}_i\ cos(\varphi) - (1-\bar{\rho}_i^2)sin(\varphi)\right) \\ B_i|_{Sin} &= \tfrac{1}{\bar{\omega}_i}\left(A_i|_{Sin}\ \bar{\xi}_i\omega_i - q_i^{max}\left((1-\bar{\rho}_i^2)\Omega\ cos(\varphi) - 2\bar{\xi}_i\bar{\rho}_i\Omega\ sin(\varphi)\right)\right) \end{aligned} \tag{4.99}$$

Harmonic Expansion Force

Nevertheless, as previously introduced in the work methodology (see section 3.2 from chapter 3), this project seeks to study the response of a cantilever beam when subjected to the action of the wind. This physical phenomena is a random feature which, apparently, does not have any time function to be introduced as $F^{ext}(t)$ in the forced damped vibration ODE 4.91 and thus, it seems impossible to know the analytical solution of the problem.

However, taking the discrete data from real measurements of wind speed over time, and using the FFT algorithm, one is able to construct a sinusoidal time dependant function which can be later used to construct a valid expression of $F^{ext}(t)$. This Fourier expansion can be modelled as (see section 4.5 for further detail):

$$V_w^2 = \sum_{k=1}^{\infty} \bar{F}_k \ sin(\Omega_k t + \varphi_k) \tag{4.100}$$

Where V_w^2 is the square of the wind speed. Chapter 6 explains why it is interesting to compute the square instead of the actual wind speed (see section 6.4).

The particular solution for this case of interest is similar to the case of a single sine (see expression 4.97), except that the number of sines is now infinite. On the other side, the homogeneous solution remains the same except for constants A_{i_k} and B_{i_k}.
Carrying out the same approach that has been conducted for sinusoidal, polynomial and exponential forces, the analytical solution, i.e $q_i^z(t) + q_i^p(t)$, for the forced damped vibrations caused by the action of the wind, can be regarded as:

$$\boxed{d = \sum_{i=1}^{n_{modes}} \sum_{k=1}^{\infty} \phi_i q_{i_k}^{max} \left\{ e^{-\bar{\xi}_i \omega_i t} \left(A_{i_k} cos(\bar{\omega}_i t) + B_{i_k} sin(\bar{\omega}_i t) \right) + (1 - \bar{\rho}_{i_k}^2) sin(\Omega_k t + \varphi_k) - 2\bar{\xi}_i \bar{\rho}_{i_k} cos(\Omega_k t + \varphi_k) \right\}} \tag{4.101}$$

Where

$$q_{i_k}^{max} = \frac{\overbrace{\phi_i^T \bar{F}_k}^{f_{i_k}}}{\omega_i^2} \frac{1}{\left(1 - \bar{\rho}_{i_k}^2\right)^2 + \left(2\bar{\xi}_i \bar{\rho}_{i_k}\right)^2} \qquad \bar{\rho}_{i_k} = \frac{\Omega_k}{\omega_i} \tag{4.102}$$

And

$$\begin{aligned} A_{i_k} &= q_{i_k}^{max} \left(2\bar{\xi}_i \bar{\rho}_{i_k} \ cos(\varphi_k) - (1 - \bar{\rho}_{i_k}^2) sin(\varphi_k) \right) \\ B_{i_k} &= \frac{1}{\bar{\omega}_i} \left(A_{i_k} \ \bar{\xi}_i \omega_i - q_{i_k}^{max} \left((1 - \bar{\rho}_{i_k}^2) \Omega_k \ cos(\varphi_k) - 2\bar{\xi}_i \bar{\rho}_{i_k} \Omega_k \ sin(\varphi_k) \right) \right) \end{aligned} \tag{4.103}$$

4.5 Fourier Analysis

As it has been described, the Fourier analysis is key for conducting the main study of this project. Hence, this section's intention is to briefly introduce the Fourier Transform and, more precisely, the Discrete Fourier Transform DFT and its fast and efficient computation, the Fast Fourier Transform FFT.

4.5.1 Fourier Transform

In Fourier analysis, when a function $f(x)$ is periodic and piecewise smooth, it can be written in terms of a Fourier Series, which is an infinite sum of sines and cosines that have increasing frequencies. For a L-periodic $f(x)$, i.e periodic in the interval $[0,\ L)$, the corresponding Fourier Series is given by [26]:

$$f(x) = \frac{a_0}{2} + \sum_{k=1}^{\infty} a_k cos\left(\frac{2\pi k}{L} x\right) + b_k sin\left(\frac{2\pi k}{L} x\right) \tag{4.104}$$

Where

$$a_k = \frac{2}{L}\int_0^L f(x)cos\left(\frac{2\pi k}{L}x\right)\ dx$$
$$b_k = \frac{2}{L}\int_0^L f(x)sin\left(\frac{2\pi k}{L}x\right)\ dx \tag{4.105}$$

When $f(x)$ is not periodic, the Fourier Series are extrapolated to a more general method called the Fourier Transform, which is essentially the limit of a Fourier Series when the domain goes to infinity. This allows to define a function on $(-\infty,\ \infty)$ that only repeats once, as it is depicted in figure 4.2:

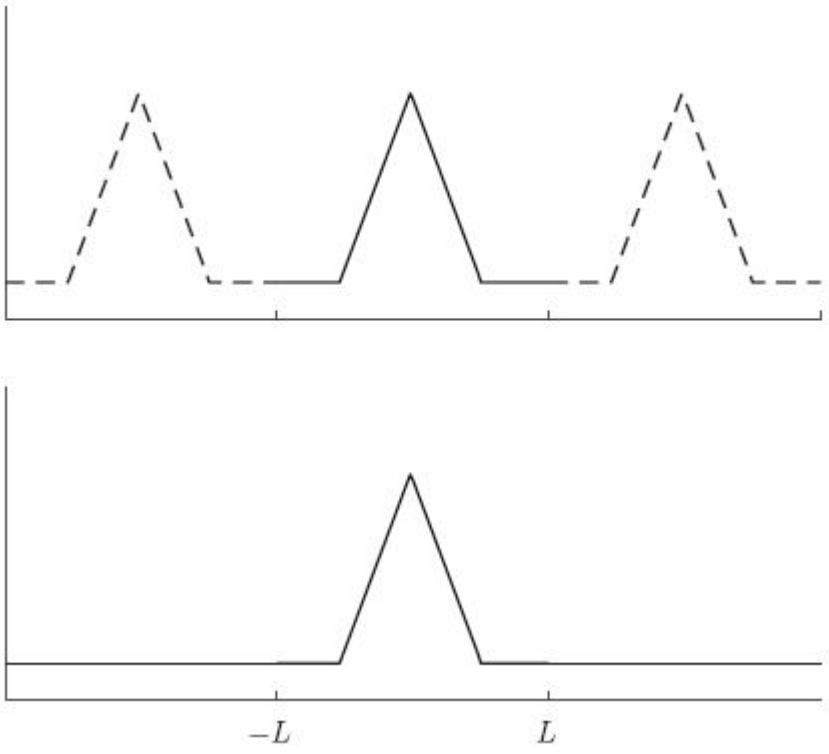

Figure 4.2: (Top) Fourier Series for a periodic function on a finite domain $[L,\ L)$ vs (Bottom) Fourier Transform for a non-periodic function.
Source: Extracted from [1].

In such case, and taking into account the Euler formula $e^{ikx} = cos(kx) + i\ sin(kx)$, equation 4.104 can also be written as:

$$f(x) = \sum_{k=-\infty}^{\infty} c_k\ e^{ikx} \tag{4.106}$$

Where c_k is given by the inner product of $f(x)$ and an infinite-dimensional orthogonal function space spanned by sines and cosines, $e^{-ik\pi\xi/L\xi} = cos(\frac{k\pi}{L}\xi) - i\ sin(\frac{k\pi}{L}\xi)$.

$$c_k = \frac{1}{2L}\int_{-L}^{L} f(x)e^{-ik\pi\xi/L}\ d\xi = \alpha_k + i\ \beta_k \tag{4.107}$$

According to 4.107, the discrete set of frequencies that are present in a Fourier Transform can be regarded as $\omega_k = k\pi/L$. If one takes the domain to infinity, i.e $L \to \infty$, this discrete set becomes continuous and the

frequency increase $\Delta\omega = \pi/L$, tends to zero in equation 4.106:

$$f(x) = \lim_{\Delta\omega\to\infty} \sum_{k=-\infty}^{\infty} \frac{\Delta\omega}{2\pi} \int_{-\pi/\Delta\omega}^{\pi/\Delta\omega} \underbrace{f(\xi)e^{-ik\Delta\omega\xi}\, d\xi}_{\hat{f}(\omega)}\, e^{ik\Delta\omega x} \tag{4.108}$$

Where $\hat{f}(\omega)$ is the Fourier Transform of $f(x)$, which will be represented by $\mathcal{F}(f(x))$.

Finally, equation 4.108 is converted to the widely known Fourier Transform pairs, represented by the Riemann integrals in equation 4.109. As stated by [1], this conversion is possible if the summation in equation 4.108 is done with weight $\Delta\omega$.

$$\begin{aligned} f(x) &= \mathcal{F}^{-1}\left(\hat{f}(\omega)\right) = \tfrac{1}{2\pi}\textstyle\int_{-\infty}^{\infty} \hat{f}(\omega)e^{i\omega x}\, d\omega \\ f(\omega) &= \mathcal{F}\left(f(x)\right) = \textstyle\int_{-\infty}^{\infty} f(x)e^{-i\omega x}\, dx \end{aligned} \tag{4.109}$$

Where $\omega = k\pi/L$.
This pair is more commonly referred as, from top to bottom, the Inverse Fourier Transform (IFT) and the Fourier Transform (FT). Generally speaking, these techniques serve as a way to transform signals from the continuous time domain to the frequency domain and vice versa.

However, these expressions are only valid for continuous functions. In this study's case, one is faced with discrete data from wind speed measurements, which suggests that the tool to be used should be the Discrete Fourier Transform.

4.5.2 The DFT and the FFT

The DFT is widely used in the engineering industry since it is able to approximate the Fourier Transform on discrete vectors of real-data, making it really useful for numerical approximation and computation.
The Discrete Fourier Transform is given by:

$$\hat{f}_k = \sum_{j=0}^{N-1} f_j e^{-i2\pi jk/N} \tag{4.110}$$

Where f_j is the function value, which in this project will be the wind speed V_w, at sample j. The total number of samples is N.
The inverse procedure or IDFT is given by:

$$f_k = \frac{1}{N} \sum_{j=0}^{N-1} \hat{f}_j e^{i2\pi jk/N} \tag{4.111}$$

Generally speaking, the DFT is a linear operator that makes it possible to identify which frequencies $\omega_k = 2\pi jk/N$ better represent the data set using a Fourier Series. All these frequencies are multiples, by means of k, of the natural frequency ω_n:

$$\omega_n = e^{-i2\pi/N} \tag{4.112}$$

To better understand the DFT, it is represented in its matrix format:

$$\underbrace{\begin{bmatrix} \hat{f}_1 \\ \hat{f}_2 \\ \hat{f}_3 \\ \vdots \\ \hat{f}_N \end{bmatrix}}_{\hat{f}(\omega)} = \underbrace{\begin{bmatrix} 1 & 1 & 1 & \dots & 1 \\ 1 & \omega_n & \omega_n^2 & \dots & \omega_n^{N-1} \\ 1 & \omega_n^2 & \omega_n^4 & \dots & \omega_n^{2(N-1)} \\ \vdots & \vdots & \vdots & \ddots & \vdots \\ 1 & \omega_n^{N-1} & \omega_n^{2(N-1)} & \dots & \omega_n^{(N-1)^2} \end{bmatrix}}_{F} \underbrace{\begin{bmatrix} f_1 \\ f_2 \\ f_3 \\ \vdots \\ f_N \end{bmatrix}}_{f(x)} \tag{4.113}$$

Since the DFT matrix F is a complex-valued matrix, the vector of Fourier coefficients $\hat{f}$ has both magnitude and phase. The physical interpretation behind them, which will be later explained in section 6.3, is fundamental to convert a discrete set of data into a Fourier expansion.

When working with the DFT, it is essential for the gathered data to be sampled with a constant sampling ratio. Otherwise, $\Delta\omega$ would never be constant and all that has been discussed so far would not be applicable.

Despite all of the above mentioned benefits, carrying out the DFT matrix system of equations in 4.113 involves $\mathcal{O}(N^2)$ operations.
The Fast Fourier Transform is a revolutionary algorithm capable of computing the DFT matrix multiplication with an order of $\mathcal{O}(N\ log(N))$. These algorithm is essentially a more efficient way of computing the DFT, since, for large amounts of data (N), the process scales almost linearly thanks to the logarithm.
In the real world, the need of coping with enormous quantities of data (also known as Big Data) is rapidly increasing in recent years. In this context, the FFT comes into play bringing with it a huge range of applications, being audio and image compressing or signal processing among others.

To achieve a computational reduction of such order, it is optimal, but not fundamental, that the number of samples N is a power of 2. Thanks to a careful reorganization of the terms in expressions 4.110 and 4.113 as even and odd terms, the DFT can be written as [1]:

$$\hat{f} = F_N f = \begin{bmatrix} I_{N/2} & -D_{N/2} \\ I_{N/2} & -D_{N/2} \end{bmatrix} \begin{bmatrix} F_{N/2} & 0 \\ 0 & F_{N/2} \end{bmatrix} \begin{bmatrix} f_{\text{even}} \\ f_{\text{odd}} \end{bmatrix} \tag{4.114}$$

Where $I_{N/2}$ is de $N/2 \times N/2$ identity matrix and $D_{N/2}$ is a diagonal matrix given by:

$$D_{N/2} = \begin{bmatrix} 1 & 0 & 0 & \dots & 0 \\ 0 & \omega_n & 0 & \dots & 0 \\ 0 & 0 & \omega_n^2 & \dots & 0 \\ \vdots & \vdots & \vdots & \ddots & \vdots \\ 0 & 0 & 0 & \dots & \omega_n^{N/2-1} \end{bmatrix} \tag{4.115}$$

The essential idea is that this reorganization process expressed in 4.114 is repeated from $F_{N/2}$ to $F_{N/4}$, $F_{N/8}$, $F_{N/16}$, etc. until, eventually, F is a 2×2 order matrix, which has a really fast computation.
If the vector of data samples is not a power of 2, it is completed with zeros until the requirement is met.
In such circumstances, the matrix system in 4.113 can be solved much more efficiently by interleaving even and odd indices of sub-vectors of $f(x)$ and transforming 4.113 into multiple 2×2 systems of equations.

4.6 Reduced Order Models

To conclude the theoretical background that is necessary to understand this work, this section will go through the importance of the Reduced Order Models (ROMs) and will also glance over the formulation and computation behind them.

4.6.1 Introduction

The main motivation of any ROM is to reduce the operational cost associated to the assembly of the nodal internal forces vector $\hat{F}$ in a FEM. This can happen, for example, when the FE mesh must be really refined and thus it requires a high amount of elements and, consequently, an even higher number of Gauss points to integrate. Furthermore, in dynamic problems, the time parameter forces the equations to be solved for every element but also at every time step. If the time domain is large, the computational effort can be really compromised.
As a first approach and as it was done in section 4.4 with the modal decomposition analysis, the FEM can be conducted via space-time decomposition. In such case, the basis functions of the FEM (Φ) will then have the same function as the natural mode shapes ϕ defined in the Modal Analysis.
Similarly to what was stated in the small strains problem (see 4.2), the only inputs that change along time are the nodal external forces $F^{ext}(t)$ and the prescribed displacements $\bar{u}(t)$. Hence, the space-time decomposition of both inputs is given by:

$$\begin{aligned} F^{ext}(t) &= \Phi\alpha(t) \\ \bar{u} &= D^u\beta^u(t) \end{aligned} \tag{4.116}$$

Where Φ is considered as a fixed spatial pattern and $\alpha(t)$ is a scalar-valued function that depends on the loading parameter t like, for example, the sinusoidal function discussed in section 4.4.2. D^u and $\beta^u(t)$ are the same concepts (spatial pattern and time functions) but they only refer to the prescribed displacements.

This way, the nodal displacement vector can be written as

$$d = \begin{bmatrix} \Phi q \\ D^u \beta^u \end{bmatrix} = \underbrace{\begin{bmatrix} \Phi & 0 \\ 0 & D^u \end{bmatrix}}_{\bar{\Phi}} \underbrace{\begin{bmatrix} q \\ \beta^u \end{bmatrix}}_{\bar{q}} = \begin{bmatrix} \bar{\Phi}_l & 0 \\ 0 & \bar{\Phi}_r \end{bmatrix} \begin{bmatrix} \bar{q}_l \\ \bar{q}_r \end{bmatrix} \tag{4.117}$$

Where q is the scalar-valued time function that describes the nodal displacement amplitude along time.

To obtain the reduced vector of internal forces $\hat{F}^*$, it is necessary to define an optimal number of modes. In a dynamic problem, the state of the system not only depends on the displacements but also on the velocities. Thus, the basis matrix Φ must capture both variables within a certain degree of accuracy. In consequence, some modes that may be negligible in terms of displacement amplitude q may contrarily become relevant to velocities, since $\mathrm{v} = \omega q$ (see equation 4.80 in section 4.4).
Once the optimal number of modes has been established, one is faced with a reduced basis matrix $\bar{\Phi}$ which represents a reduced-order space. The process to obtain the basis matrix Φ is explained at the end of this section.

Likewise in the modal decomposition analysis, the FE semi-discrete equation of motion in 4.42 is brought into light. This time however, the equation is replaced with the reduced-space variables:

$$\delta q^T \bar{\Phi}^T \left(M_l \bar{\Phi} \ddot{\bar{q}} + D_l \Phi \dot{\bar{q}} + \hat{F}_l(\bar{q}) - F_l^{ext} \right) = 0 \begin{cases} \bar{q}(0) = \bar{\Phi}^T d^0 \\ \dot{\bar{q}}(0) = \bar{\Phi}^T \mathrm{v}^0(0) \end{cases} \tag{4.118}$$

As in the modal analysis, the unknown is q. However, as the preceding equation is used for FE analysis, the unknown is now a discrete variable (one value for each node at each time step).

The reduced-order counterpart of the original mass and damping matrices, as well as the external and internal forces vectors, are defined as:

$$\begin{aligned} M^* &= \bar{\Phi}^T M \bar{\Phi} \\ D^* &= \bar{\Phi}^T D \bar{\Phi} \\ \hat{F}^* &= \bar{\Phi}^T \hat{F} \\ F^{ext\,*} &= \bar{\Phi}^T F^{ext} \end{aligned} \tag{4.119}$$

Hence, semi-discrete equation of motion is rewritten in terms of the reduced-order coordinates as

$$M_l^* \ddot{\bar{q}} + D_l^* \dot{\bar{q}} + \hat{F}_l^* - F_l^{ext\,*} = 0 \tag{4.120}$$

$$M_l^* \ddot{\bar{q}} + D_l^* \dot{\bar{q}} + \hat{F}_l^* - F_l^{ext\,*} = 0 \begin{cases} M^* = \bar{\Phi}^T M \bar{\Phi} \\ D^* = \bar{\Phi}^T D \bar{\Phi} \\ \hat{F}^* = \bar{\Phi}^T \hat{F} \\ F^{ext\,*} = \bar{\Phi}^T F^{ext} \end{cases} \tag{4.121}$$

This ROM has less equations to be solved than the initial semi-discrete equation of motion. Nevertheless, according to expression 4.39, the term $\hat{F}$ is still related to the FE mesh, since it still requires the computation of the PK1 stresses at all Gauss points of the mesh.
Instead, this project seeks to overcome this computational bottleneck by trying to reduce the number of Gauss points needed to compute $\hat{F}^*$ within a certain level of accuracy.

Computation of Φ

The basis matrix Φ belongs to a $\mathbb{R}^{n_{el} n_{sd} \times n}$ space, where n is the optimal number of modes needed to reduce the dimension of the problem within a given accuracy tolerance.
Thus:

$$\Phi = \begin{bmatrix} \Phi_1 & \Phi_2 & \dots & \Phi_n \end{bmatrix} \tag{4.122}$$

This basis matrix is normalized such that $\Phi^T M \Phi = I$, where the geometric matrix is equal to the identity $M = I$ in cases where the mesh is regular. Hence, in this work, $\Phi^T \Phi = I$.

The basis matrix is obtained in two subsequent stages: the training and the dimensionality reduction.

- **Training**: The FE equations are solved for the corresponding inputs of the problem and its solutions (displacements and PK2 stresses at each time step), are stored in snapshot matrices A^d and A^s, respectively. These matrices take the following form:

$$A^d = \begin{bmatrix} d_l(t_1) & d_l(t_2) & \dots & d_l(t_{n_{steps}}) \end{bmatrix} \tag{4.123}$$

$$A^s = \begin{bmatrix} S(t_1) & S(t_2) & \dots & S(t_{n_{steps}}) \end{bmatrix} \tag{4.124}$$

- **Dimensionality Reduction**: the basis matrix is computed as a linear combination of the columns of A^d, or, in other words, Φ is a subspace of the column space of A^d.
  As stated above, the idea is to obtain the smallest sumber of columns of Φ while retaining the essential information from the solution (A^d and A^s). For such, error thresholds for each solutions are defined (ϵ^d and ϵ^s).
  Φ is then obtained by solving the following system:

$$\begin{aligned} ||A^d - \Phi\Phi^T A^d|| \leq \epsilon^d ||A^d|| \quad \text{with } 0 \leq \epsilon^d < 1 \\ ||A^s - A^s_\Phi|| \leq \epsilon^s ||A^s|| \quad \text{with } 0 \leq \epsilon^s < 1 \end{aligned} \tag{4.125}$$

Where $||\ ||$ is the Frobenius norm and A^s_Φ is the snapshot matrix of the PK2 stresses produced by $d_\Phi = \Phi^T \Phi d$, i.e the displacements projected onto the span of Φ.

The preceding matrix system 4.125 is solved with the help of a Truncated Singular Value Decomposition (SVD), which is fundamental to compute A^s_Φ in an efficient way.
The SVD is computed so as to meet the first equation in 4.125:

$$A^d = \sum_{i=1}^{r} U_i \lambda_i V_i^T + E \tag{4.126}$$

Where U_i, λ_i and V_i are the left singular vectors, singular values and right singular vectors, respectively [26]. The desired basis matrix will be $\Phi = U$. Furthermore, r is the level of truncation (i.e the number of rows that are included from the entire SVD) and E is the truncation term, which Forbenius norm is given by:

$$||E||^2 = \underbrace{\sum_{i=1}^{P} \lambda_i^2}_{||A^d||^2} - \sum_{i=1}^{r} \lambda_i^2 = \sum_{i=r+1}^{P} \lambda_i^2 \tag{4.127}$$

The level of truncation r is therefore chosen according to:

$$\sum_{i=r+1}^{P} \lambda_i^2 \leq (\epsilon^d)^2 \sum_{i=1}^{P} \lambda_i^2 \tag{4.128}$$

As previously mentioned, in a dynamic problem, the state of the system is determined by the velocities too. This issue is either solved by constructing a mix snapshot matrix of displacements and velocities instead of only displacements, or progressively decrease the SVD tolerance until the error is below the prescribed threshold. In the present work, the first option is the one that has been considered in the code.

Finally, A^s_Φ can be computed to check whether the second constraint of the matrix system 4.125 is met. The snapshot matrix of projected displacements is given by:

$$A^d_\Phi = \Phi \Phi^T A^d = U U^T A^d \tag{4.129}$$

And thus, A^s_Φ will be the PK2 stresses produced by A^d_Φ:

$$A^s_\Phi = S\left(A^d_\Phi\right) \tag{4.130}$$

System 4.125 is to be solved until the convergence is met. In practical terms, it has to be iteratively solved until the truncation level r satisfies the convergence tolerances ϵ^d and ϵ^s.

4.6.2 Hyperreduction

This study will cover a ROM known as the Hyperreduction Order Model (HROM), whose main idea is based on a property of integrals that states that if the integrand lies in a subspace of dimensions r, then the required

number of integration points is of order of magnitude $\mathcal{O}(r)$. According to [13], exactly integrating p integrand modes Φ (plus the volume) requires $m = p + 1$ points.

As previously advanced, this method seeks to compute the reduced vector of nodal internal forces $\hat{F}^*$ by using the minimum amount of Gauss points and their respective positive weights, required to respect an arbitrary accuracy tolerance. To do so, it is interesting to express the assembly of this vector in terms of all the Gauss points (see section 4.2.5):

$$\hat{F}^* = \sum_{e=1}^{n_{el}} \bar{\Phi}^{e^T} \hat{F}^e = \sum_{e=1}^{n_{el}} \sum_{g=1}^{m} \mathcal{W}_g^e \left(\bar{\Phi}^{e^T} \hat{f}_g^e \right) = \sum_{e=1}^{n_{el}} \sum_{g=1}^{m} \mathcal{W}_g^e \hat{f}_g^{*e} \tag{4.131}$$

According to the definition of $\hat{F}$ in 4.39 and applying it to every Gauss point in a finite element, $\hat{f}_g^{*e}$ is given by:

$$\hat{f}_g^{*e} = \bar{\Phi}^{e^T} B^{e^T} \left(X(\xi_g) \right) \; P\left(X(\xi_g) \right) \tag{4.132}$$

Where P refers to the PK1 stress at every Gauss point.

Since this project does not contemplate the effect of follower loads, the hyperreduction stage is posed only in terms of the internal forces.

The HROM can be conducted in two different ways: Element-based or Point-based HROM (see chapter 5). As mentioned, the approach that will be carried out in this study is the Point-based HROM, which allows to find a set of points $\bar{X}_1,\ \bar{X}_2 \dots \bar{X}_{\bar{m}}$ and their associated positive volumetric weights $\omega_1,\ \omega_2 \dots \omega_{\bar{m}}$:

$$\hat{F}^* = \sum_{g=1}^{\bar{m}} \omega_g \hat{f}^* \left(\bar{X}_g \right) = \sum_{g \in \mathbb{Z}} \omega_g \hat{f}_g^* \tag{4.133}$$

Where $\bar{m}$ is the number of desired Gauss points extracted from the set of all Gauss points, with $\bar{m} << m \cdot n_{el}$. This subset of points is referred as $\mathbb{Z}$.

$\hat{f}_g^*$ is the *g-th* entry of the vector formed by stacking the internal forces per unit volume at all Gauss points. Thus, the vector containing all $\hat{f}_g^*$ is given by $\hat{\mathcal{F}}_l^*(t)$ in the element-free notation (see section 4.2.5):

$$\hat{\mathcal{F}}_l^*(t) = \begin{bmatrix} \hat{f}_l^* \left(X_1^1, t \right) \\ \hat{f}_l^* \left(X_2^1, t \right) \\ \vdots \\ \hat{f}_l^* \left(X_m^1, t \right) \\ \hat{f}_l^* \left(X_1^2, t \right) \\ \vdots \\ \hat{f}_l^* \left(X_{m-1}^{n_{el}}, t \right) \\ \hat{f}_l^* \left(X_m^{n_{el}}, t \right) \end{bmatrix} = \begin{bmatrix} (\mathbf{\Phi}_l^{1^T} B^{1^T}(X_1^1)) \; P(X_1^1, t) \\ (\mathbf{\Phi}_l^{1^T} B^{1^T}(X_2^1)) \; P(X_2^1, t) \\ \vdots \\ (\mathbf{\Phi}_l^{1^T} B^{1^T}(X_m^1)) \; P(X_m^1, t) \\ (\mathbf{\Phi}_l^{2^T} B^{2^T}(X_1^2)) \; P(X_1^2, t) \\ \vdots \\ (\mathbf{\Phi}_l^{n_{el}^T} B^{n_{el}^T}(X_{m-1}^{n_{el}})) \; P(X_{m-1}^{n_{el}}, t) \\ (\mathbf{\Phi}_l^{n_{el}^T} B^{n_{el}^T}(X_m^{n_{el}})) \; P(X_m^{n_{el}}, t) \end{bmatrix} \tag{4.134}$$

Hence, for each time step, one is faced with a block matrix $\hat{\mathcal{F}}^*(t)$ that has as many rows as Gauss points per element and as many columns as modes in Φ:

$$\hat{\mathcal{F}}^*(t) = \left[\hat{\mathcal{F}}_1^*(t)\ \hat{\mathcal{F}}_2^*(t)\ \dots\ \hat{\mathcal{F}}_{n_{modes}}^*(t)\right] \tag{4.135}$$

Thus, $\hat{F}_l^*$ given in equation 4.119 is rewritten as:

$$\hat{F}_l^*(t) = \Phi^T \hat{F}_l(t) = \mathcal{F}^{*^T}(t)\mathcal{W} \quad \text{with} \quad \mathcal{W} = \left[\mathcal{W}_1^1,\ \mathcal{W}_1^2 \dots \mathcal{W}_m^{n_{el}}\right] \tag{4.136}$$

4.6.3 Empirical Cubature Method

Henceforth, the procedure of finding the subset of $\mathbb{Z}$ points and their associated weights (α) will be briefly covered. As mentioned in the state of the art review, the algorithm that has been selected to conduct the point selection problem is called the Empirical Cubature Method (ECM).

To better deal with the large amount of data that a space-temporal problem involves, the snapshot matrix of reduced internal forces is constructed as follows [27]:

$$A^f = \left[\hat{\mathcal{F}}^*\left(t_1\right),\ \hat{\mathcal{F}}^*\left(t_2\right),\ \dots,\ \hat{\mathcal{F}}^*\left(t_{n_{steps}}\right)\right] \tag{4.137}$$

For the point selection problem, the following condition must be met:

$$A^{f^T}\mathcal{W} = A^f\left(\mathbb{Z},:\right)^T\omega \tag{4.138}$$

Where the index $(\mathbb{Z},:)$ refers to all the columns of the rows represented by $\mathbb{Z}$.
In cases where $A^{f^T}\mathcal{W} \approx 0$, to avoid the trivial solution $\omega = 0$ in the preceding equation 4.138, it is necessary to introduce a second constraint:

$$\sum_{g=1}^{\bar{m}} \omega_g = \sum_{g=1}^{m}\sum_{e=1}^{n_{el}} \mathcal{W}_g^e = V \tag{4.139}$$

Where V is the volume of the undeformed domain Ω_0.

According to [28], the point selection problem should be addressed with respect to an orthogonal matrix (Q) of the column space of A^f.
Thus, Q must satisfy $A^f = QR$ (where $R = Q^T A^f$), and is used to rewrite equation 4.138 as:

$$R^T Q^T \mathcal{W} = R^T Q\left(\mathbb{Z},:\right)^T\omega \tag{4.140}$$

Taking into account the fact that Q spans the column space of A^f, the preceding equation is equivalent to

$$Q^T\mathcal{W} = Q\left(\mathbb{Z},:\right)^T\omega \tag{4.141}$$

In practice, Q is approximated using a relative truncation error ϵ^f as:

$$||A^f - QQ^T A^f|| \leq \epsilon^f ||A^f|| \tag{4.142}$$

Where the norm is calculated with the vector of Gauss points weights $\mathcal{W}$.
With this in mind, equation 4.141 is reformulated as:

$$\bar{A^f}^T \sqrt{\mathcal{W}} = \bar{A}^f (\mathbb{Z}, :)^T \underbrace{\left(\sqrt{\mathcal{W}(\mathbb{Z})} \circ \omega\right)}_{\alpha} \tag{4.143}$$

Where $\circ$ is the element-wise matrix multiplication or Hadamard multiplication and $\bar{A}^f$:

$$\bar{A}^f (:, l) = A^f (:, l) \circ \mathcal{W} \tag{4.144}$$

The approximation of Q is achieved thanks to the Truncated Singular Value Decomposition (SVDT) of $\bar{A}^f$, the level of truncation of which is imposed by ϵ^f. The process to conduct the SVDT is exactly the same as the one used to obtain the displacement snapshot matrix A^d in section 4.6.1.
If the problem involves $A^f \mathcal{W} \approx 0$, Q is expanded with an extra column (a) that corresponds to the extra constraint regarding the volume of Ω_0 (see equation 4.139):

$$a = \sqrt{W} - QQ^T \sqrt{W} \tag{4.145}$$

Finally, one can compute the matrix G, which is fundamental to determine the subset of Gauss points $\bar{m}$ and their respective positive weights α:

$$G^T = \begin{cases} \left[Q \frac{a}{||a||}\right] & \text{if } A^f \mathcal{W} \approx 0 \\ Q & \text{otherwise} \end{cases} \tag{4.146}$$

The ECM takes as inputs G, $\mathcal{W}$ and a convergence tolerance of 10^{-8} referred as TOL in [28] and [27]. Its objective is to compute the $\mathbb{Z}$ indices of G and their weights α so that:

$$G (:, \mathbb{Z})\, \alpha = G \sqrt{\mathcal{W}} \tag{4.147}$$

$\bar{m}$ is equal to the number of columns of G and the desired positive weights are extracted from $\alpha = \omega \circ \sqrt{\mathcal{W}(\mathbb{Z})}$.
The indices of the desired Gauss points $\mathbb{Z}$ are the same as those $\mathbb{Z}$ columns of G.

Thus, the ECM consists on a greedy selection algorithm that uses ML techniques to be able to find the absolute minimum (exact integration) of the optimization problem arising from the above-mentioned decomposition of A^f into its component along the range of the integral operator, and its component along the nullspace [13].

Chapter 5

Consideration of the solution adopted with respect to other approaches

In this chapter, the author intends to cover some alternatives that could have been performed in order to reach the same objectives that this project seeks to achieve. Moreover, the author will also provide the reader with arguments that justify the reasons why these alternative paths have not been considered.

The approach that have been used, which is detailed in chapter 4, has been the same from the very beginning and therefore, the alternatives explained in this chapter must not be understood as discarded approaches.

All of these alternatives are related to the different hypothesis and techniques that can be used inside a structural vibrations finite element analysis. They will be divided into three different categories: Problem Statement, Computational Techniques and Hyperreduction alternatives.

5.1 Problem Statement

The alternatives that are given in this section are related to the physical statement of the structural vibrations problem.

5.1.1 Isotropy

Isotropy is a property of same materials which indicates that their properties do not depend on the direction in which they are measured. For example, an isotropic material will offer the same resistance against either an axial or tangential stress.
All simulations conducted inside this project consider the aluminium described in table 3.1 as isotropic.

However, one could also have opted for an anisotropic material. Considering this choice would add effort

and complexity to the pre-process, since one would have to search for the properties in table 3.1 for each direction. Furthermore, the FE code would have to be adapted, as it would have to verify which type of direction does every stress have, thus significantly increasing the computational effort.
Since this project by itself already requires an important computational effort, adding the anisotropic effect to it is considered unnecessary, since the solution that would yield from it would not provide added value to the chosen solution.

5.1.2 Frame of Reference

Choosing a rotating frame of reference instead of the selected inertial frame would imply reformulating the entire model of both small and large strains (sections 4.2 and 4.3 respectively). Rotating frames also involve rotating matrices that would translate into a new type of displacement known as straining displacement, which represents the strain that the structure suffers when it rotates. In addition, the fact that there is rotation also complicates the FE formulation.

On top of that, the simulations that are ran in this project only consider distributed forces which are applied on the top surface of the beam. This means that the beam will only suffer a 2D bending motion that can be fully captured using an inertial frame of reference.

5.1.3 Rayleigh Damping

In the modal decomposition analysis, the Rayleigh damping hypothesis has been used (see equation 4.87). This statement is used in order for the damping matrix D to be a linear combination of the mass matrix M and the stiffness matrix K. This hypothesis enables the system to be decoupled, which indicates that every ODE can be solved independently.
This greatly facilitates the process of obtaining the analytical solution, since it consists on a linear combination of all the uncoupled solutions (as explained in section 4.4).

Even so, other damping models could also be used to find an analytical solution. These models try to counteract the main drawbacks from the Rayleigh damping, such as the need for small time steps or the induced body forces for motion at a constant velocity. One example is the Maxwell damping, which, according to [29], is widely used to approximate frequency independent damping in time-domain seismic deformation analyses.

5.1.4 Buckling Phenomena

Although not included in this project's scope, the buckling phenomena would be a nonlinear feature that would indeed add extra value to the simulations. Being able to detect a plastic failure in a structure is of utmost importance in the field of structural analysis.

However, as it happened with the isotropy, including buckling would imply searching for the plastic behaviour of the material and reformulate the FE pre-process. Furthermore, in cases where buckling is reached, the state equations that govern the problem would vary drastically and thus would further complicate matters.

To avoid it, the chosen solution is intentionally subjected to conditions under which buckling does not occur.

5.2 Computational Techniques

This section's aim is to cover alternative computational approaches that could have been used instead of the selected ones.

5.2.1 Time Integration Scheme

As explained in chapter 4, section 4.2.6, the method that is followed during this study when it comes to temporal integration is the Newmark-Bossak integration scheme.
According to [22], *"Because the higher modes of semi-discrete structural equations are artifacts of the discretization process and not representative of the behavior of the governing partial differential equations, it is generally viewed as desirable and often is considered absolutely necessary to have some form of algorithmic damping present to remove the participation of the high-frequency modal components"*. Removing high frequency modes involves increasing the value of the Newmark parameter γ, which at the same time, results in an accuracy drop.

Thus, implicit Newmark β-methods like the ones described in [15] are not of interest for this study, since the damping effect is a feature that must be considered and analysed.

The Newmark-Bossak scheme though, is one of the methods that have been developed with the objective of algorithmically computing the damping effect in higher frequencies without compromising the accuracy.

5.2.2 Finite Element Basis

All FEMs are based on finite-dimensional approximations. Although there is a wide range of approximation methods, there are two of them that are specifically used for academic purposes.

The first one and most simple, is to solve the FE equations for every node in every element. In this case, the outcome is a series of discrete data that corresponds to the solution of each node. Although this method could be appropriate for this work, the accuracy clearly depends on the mesh, since it must be quite refined in order to obtain a seemingly continuous solution.

The second approach, which is the one chosen for this work, is the Galerkin's approximation method. As seen in chapter 4, section 4.2.3, this technique assigns what is known as shape function $N(x, y)$ to every single node in the mesh. By doing so, the solution that corresponds to this node can be extrapolated to all the physical domain of the corresponding finite element. Considering that for every node, the solution becomes piecewise smooth and can be seen as continuous, is a great advantage for post-process matters.
These shape functions consist on polynomials known as basis FE functions. The higher the degree of the basis function, the higher the accuracy of the FEM, while, on the other hand, the more complicated does the FE formulation get.
Since the simulations included in this work do not contain conditions (i.e external forces, boundary conditions

or material properties) that could lead to complex and highly nonlinear responses, choosing linear FE basis as shape functions is held to be legitimate.

Nonetheless, there exist other approximations like the Petrov-Galerkin method, which, according to [30], employs different types of shape functions for trial and test functions (u^h and v^h - see section 4.2.4).

5.2.3 FFT Alternative

Regarding the wind-response analysis, there are two distinctive ways of obtaining the external force that the wind produces and formulate it in the FE code.

On the one side, and the most obvious one, would be to manually introduce the wind speed measurements into the code and directly calculate the lift force that the wind produces on the structure at every time step. However, the way in which the code has been thought to operate is to introduce the external forces as temporal functions. Moreover, the manner in which the code stores the variables for their general use in any function also complicates the fact of manually introducing the data.

On the other side, as previously discussed in section 4.5, the FFT can be used to transform discrete data into a time domain function consisting on a Fourier expansion, which is exactly what the original code has been thought to cope with.
Although it requires more effort than the first option, once the code to compute the FFT is created, it can be applied to any series of data, which is better if more simulations are to be conducted using real measurements.

5.3 Hyperreduction

To conclude this chapter, other possibilities regarding the HROM techniques are exposed along this section. Taking into account that Artificial Intelligence is a disruptive field that is nowadays exploding more than ever, it must be noted that there is a large number of alternatives to data compression, dimensionality reduction, optimization, etc.
Nonetheless, some of these alternatives are still in their infancy, and many theoretical and practical aspects still remain unaddressed.

That being said, this section will only cover some of the relevant ML techniques in this work and their possible alternatives.

5.3.1 Element-based HROM

Alternately to the point-based HROM, this method's aim is to choose a reduced set of FE elements $\mathbb{E} \in \{1,\ 2,\ \dots\ ,\ n_{el}\}$ and thus, their respective Gauss points too. This approach is by far the less intrusive methodology and it is more suited for cases in which the FE implementation does not allow the extraction and storage of information at the Gauss point level. According to [31], numerical experience states that the number of required entities, i.e elements or points, is practically the same either with the point-based or the

element-based methods. Hence, the number of Gauss points selected in the element-based approach is m times larger than the one obtained with the point-based.

The downside of this approach is, a part from the larger number of chosen Gauss points, the fact that it is also less efficient than the point-based HROM, since the rank of the snap hot matrix is higher.

5.3.2 Updatable Basis

The HROM with updatable basis is an alternative to the chosen approach, since it makes use of what is called the k-means clustering algorithm (see, for instance, [32], [33], [21]). This is a ML algorithm that essentially divides the given set of snapshots A^d and A^s into clusters that exhibit similar features. By doing so, the nodal displacements are approximated using local basis for each region or cluster instead of being obtained with a single global basis matrix.

Nevertheless, this kind of approach is used in problems where the dimension of the input space, i.e the external forces, is much smaller than the FE space dimension and/or in problems where the solution is also of dimension much smaller than the FE space.

In the case of study, none of those hypothesis apply.

Chapter 6

Description of the Study and Discussion of the Results

As it has been advanced in the foregoing, this project includes a series of studies, which will be pertinently covered in this chapter. The two principal studies are:

- Analysis of the dynamic linear response of the cantilever beam under the action of the wind. Comparison of the FEM, the modal decomposition analysis and the HROM.
- Analysis of the dynamic nonlinear response of the cantilever beam under the action arbitrary forces. Comparison of the FEM and the HROM.

As explained in chapter 4, section 4.2, the FEM equations will be integrated using a combination of the Newmark-Bossak integration scheme and the Newton-Raphson method. Furthermore, all the equations used for the modal approach have been deduced in section 4.4, and the HROM background is found in section 4.6, both sections in the aforementioned chapter.

Initially, the code which is used to conduct the analysis is only capable to work with a specific external force. As explained in 3, this external force is a single harmonic distributed force like the one represented in equation 3.1. Therefore, the code must be adapted and/or modified gradually, with the objective of being able to launch simulations no matter the external force or the regime to which the structure is responding.

To ensure that the code gives out legitimate results and that the adaptations are not affecting its functionality and efficiency, it is necessary to conduct some preliminary simulations that will serve to corroborate that everything is in order.
Hence, these intermediate simulations will also be included in this chapter.

Moreover, since computing the time function of the wind speed requires using the FFT, the only piece of code that has been created from scratch by the author is the one discussed in section 6.3.

It is worth mentioning that the majority of work behind this thesis comes from the analysis and discussion of

the simulations results but, most of all, it comes from the process of iteratively adapting and fixing the code until the right results are obtained.

6.1 Forced Undamped Vibrations

As described in section 4.4.1, this is the simplest case, since the response of the system does not depend on the velocity of vibration and damping effects are not included.

In the beginning of this thesis, the initial code was already capable of solving these problem for the case of a uniformly distributed external force consisting of one single sinusoidal function given by:

$$F^{ext}(t) = \bar{F}\ sin(\Omega t) \tag{6.1}$$

Since the study seeks to analyse the dynamic response of the structure in an environment that simulates reality to the fullest extent possible, these case of study is only used for getting familiar with the code methodology. This way, the student is able to understand the code and how it operates, and makes it more intuitive to adapt it to the following cases of studies.

6.2 Forced Damped Vibrations

Considering that the code can only be faced with external forces like the one described in equation 6.1 when the problem is under the hypothesis of undamped conditions, the code must suffer some adjustments. The final objective of this case of study is being able to correctly compute the dynamic response of the cantilever beam under the forced damped vibration problem hypothesis detailed in section 4.4.
Moreover, the results will be discussed for 2 different types of uniformly distributed external forces, also explained in section 4.4: external force consisting on a single sine (harmonic force), and external force consisting on a harmonic expansion. These forces, as well as all the forces contemplated on this work, are distributed on the top surface of the beam.

Before beginning with the actual simulations, it is important to define the general inputs that will be used in all of them, as well as the reasons behind their choice.

6.2.1 Code Inputs and Considerations

Since the damping effect is addressed, one must consider the Rayleigh damping hypothesis defined in section 4.4.2, equation 4.87:

$$D = \bar{\alpha}M + \bar{\beta}K$$

Bearing in mind that no rigorous method to estimate $\bar{\alpha}$ and $\bar{\beta}$ has been explored in chapter 4, it is more suitable to follow the author's criteria.

If one considers equation 4.90, the damping ratio $\bar{\xi}$ is a function of both the damping parameters $\bar{\alpha}$ and $\bar{\beta}$:

$$\bar{\alpha} + \bar{\beta}\omega_i^2 = 2\bar{\xi}_i\omega_i \tag{6.2}$$

Where ω_i and $\bar{\xi}_i$ are the natural frequency and damping ratio of the *i-th* natural mode of the structure.

It is actually simpler to estimate the damping ratio than the damping parameters $\bar{\alpha}$ and $\bar{\beta}$, since the damping ratio is a property of utmost importance in any structure: every structural study or analysis refers to the damping ratio when addressing any issue related to the damping effect. Thus, finding values of $\bar{\xi}$ for similar cases of study is not as complex as doing it for $\bar{\alpha}$ and $\bar{\beta}$.
The procedure that is followed to compute the damping parameters is to select an arbitrary value of $\bar{\xi}$ for the first natural mode of the structure. In this case, the first natural mode is also the first and most important bending mode. Since uniformly distributed forces applied on the top surface of the beam only produce bending motion, it seems coherent to define the damping ratio of the main mode of vibration and extract the values of $\bar{\alpha}$ and $\bar{\beta}$ from it. The rest of $\bar{\xi}_i$ can be then calculated with equation 6.2.

Strictly speaking, the stiffness matrix represented in equation 4.87 is the initial stiffness matrix K_0, i.e K when the displacements are zero, which happens to be the initial condition of the cantilever beam. Hence, as the structure finds itself in equilibrium in the initial condition, it does not suffer any stiffening effect and thus, one can consider $K_0 = 0$.
It is important to notice that this hypothesis can be formulated only when the viscosity effects are introduced directly in the constitutive equation, i.e the damping effect is incorporated into the relationship between the stresses and strains (see equation 4.17). Since the Green-Lagrange strain tensor $\{E\}$ includes the viscosity or damping effect, K_0 can be neglected.

This way, $\bar{\beta}$ can be disregarded and one is only faced with $\bar{\alpha}$, which, according to equation 6.2, is given by:

$$\bar{\alpha} = 2\bar{\xi}_i\omega_i \tag{6.3}$$

In order to avoid overdampng, underdamping or critical damping, the chosen value of $\bar{\xi}$ has been established to 0.02 and thus, considering the natural frequency of the first mode $\omega_1 = 109.309\ rad/s$ (see section 1 from the Annexes document), $\bar{\alpha} = 4.372$.

The code uses, 20 modes by default in the modal decomposition analysis (ϕ), see section 4.4. For the hyperreduced order stage, see section 4.6, the basis modes (Φ), are determined by the code itself in accordance with the error tolerances that are arbitrarily defined.
Furthermore, the HROM stage will only be performed in the wind and nonlinear studies (see sections 6.4 and 6.5 respectively), since all the other cases do not involve a considerable computational effort and, thus, running the HROM stage would not make an appreciable difference.

The time domain of the simulation is considered 20 times the first natural period, i.e $20T_1 = 40\pi/\omega_1 = 1.150\ s$. The number of time steps is considered to be of 200 steps per first natural period. Although it may seem

as an excessive value, it will later be seen that, in order to capture the damping effects in the vibration of the structure, the number of time steps must be higher than usual, since those effects translate into small perturbations inside each oscillation.
In such case, since the time domain is equal to 20 times the first natural period, the default number of time steps ascends to 4000.

Finally, it must be highlighted that, in order to use the analytical solutions deduced with the modal decomposition analysis in section 4.4, the initial conditions d^0 and v^0, i.e when $t = 0\ s$, are considered zero in every single simulation to be launched in this chapter.

The inputs related to the external forces will be addressed in what follows.

6.2.2 Harmonic Force

According to section 4.4.2, the external force has the upcoming form (extracted from equation 4.95):

$$F^{ext}(t) = \bar{F}\ sin(\Omega t + \varphi)$$

In contrast with equation 6.1, this harmonic force also includes a phase shift φ. This parameter is intentionally included with an eye on the FFT, which, as further explained in section 6.3, gives out phase shifts for every single frequency.

Low Frequency Sine

The first simulation seeks to represent the dynamic response of the structure under the effect of a uniformly distributed force which consists on a harmonic force like the one depicted in figure 6.4.
The parameters that define this harmonic function are given by:

$$\begin{gathered} \bar{F} = 0.1\ MPa \\ f = \tfrac{1}{3}\ Hz \rightarrow \Omega = \tfrac{2\pi}{3}\ rad/s \\ \varphi = \tfrac{\pi}{4}\ rad \end{gathered} \tag{6.4}$$

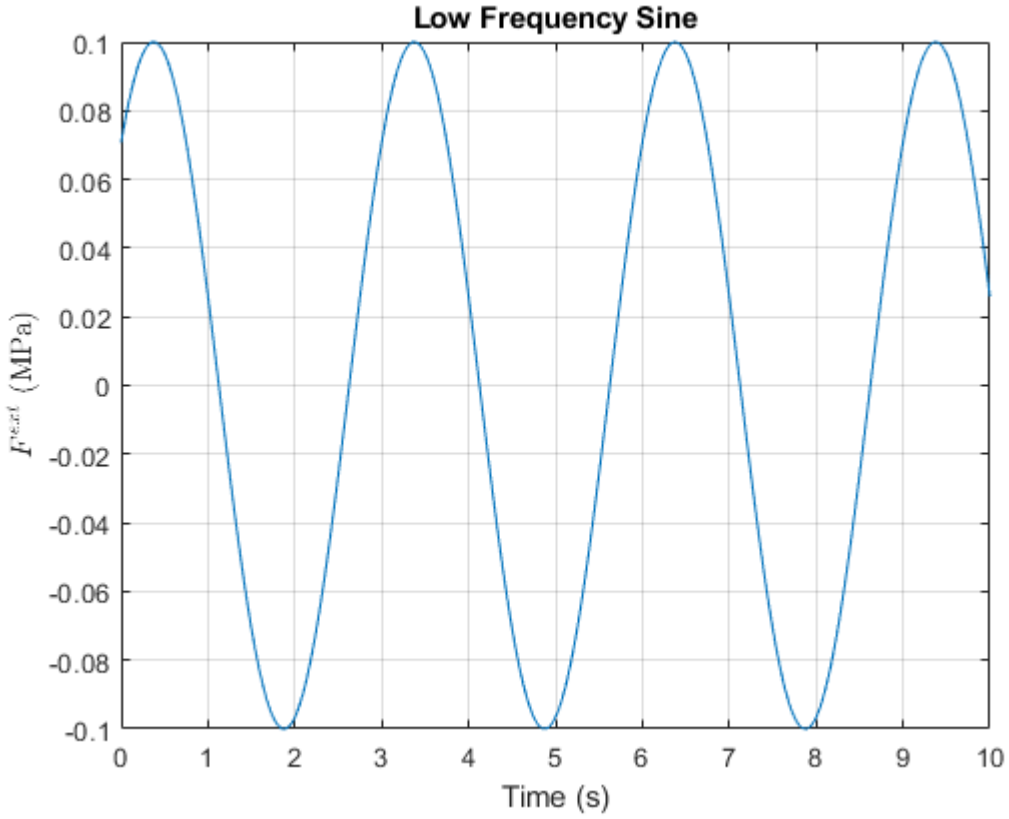

Figure 6.1: Time evolution of an external force consisting on a single low-frequency sinusoidal function. *Source: Own elaboration.*

It is worth mentioning that this sine is the first one of the expansion that will be addressed in the next section 6.2.3.

With all the inputs defined in the present section and section 6.2.1, the simulation is launched and the following is obtained:

Firstly, it is interesting to visualize the portion of the external force represented in 6.1, since the time domain is cut to just 1.15 seconds:

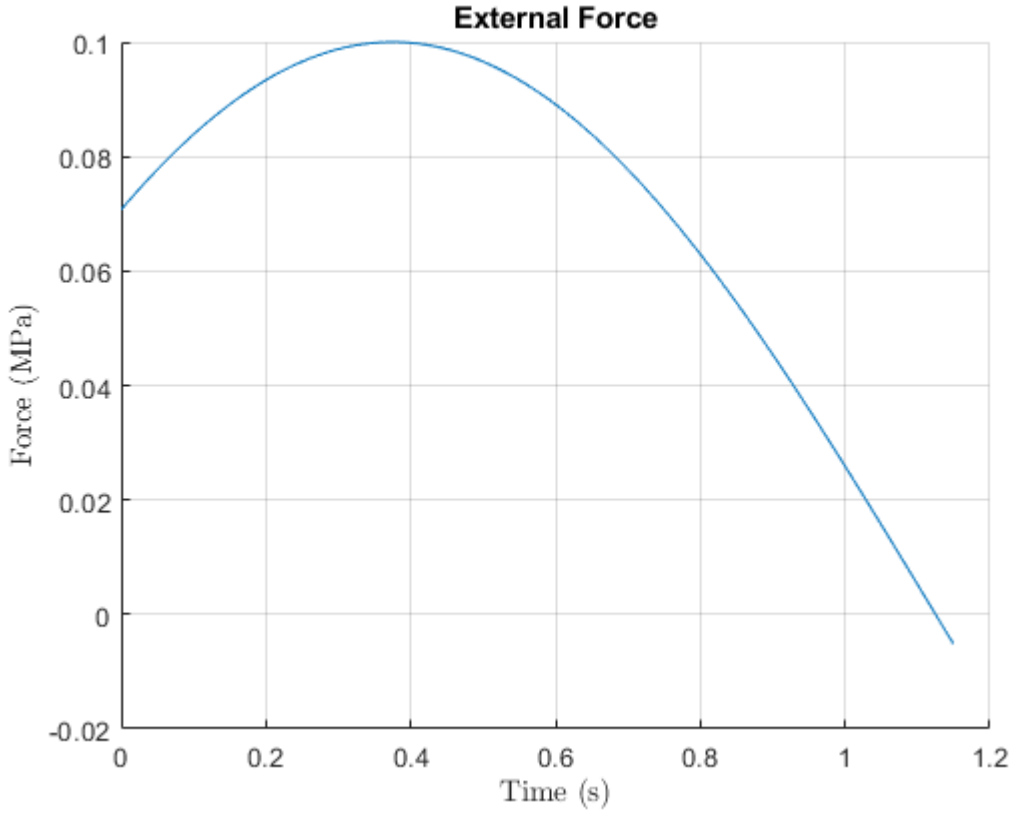

Figure 6.2: Representation of the external force applied in this case of study.
Source: Own elaboration.

To analyse both the displacement and the velocity of vibration of the structure, it has been decided to represent them on a node situated at the free end of the beam (see figure 6.3), since it is located on the section that experiences the maximum displacement and velocity.
Considering that it is a 2D problem and that the external forces that are to be applied only contribute to producing bending motion, the only degree of freedom of interest is the vertical movement, i.e along the y axis. Thus, the corresponding degree of freedom will be number 2814, which corresponds to node 1407.

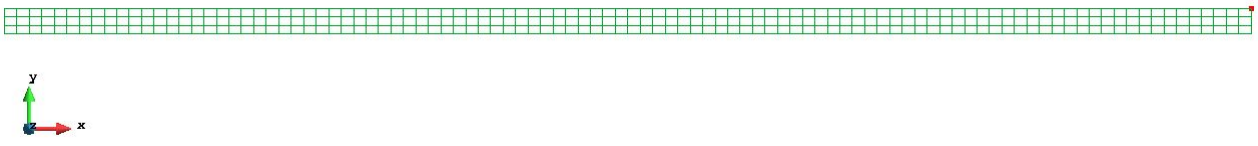

Figure 6.3: Identification of the 1407^{th} node in the GiD mesh of the structure.
Source: Own elaboration.

That being said, the displacement and velocity of DOF 2814 obtained after launching the FE study are the upcoming:

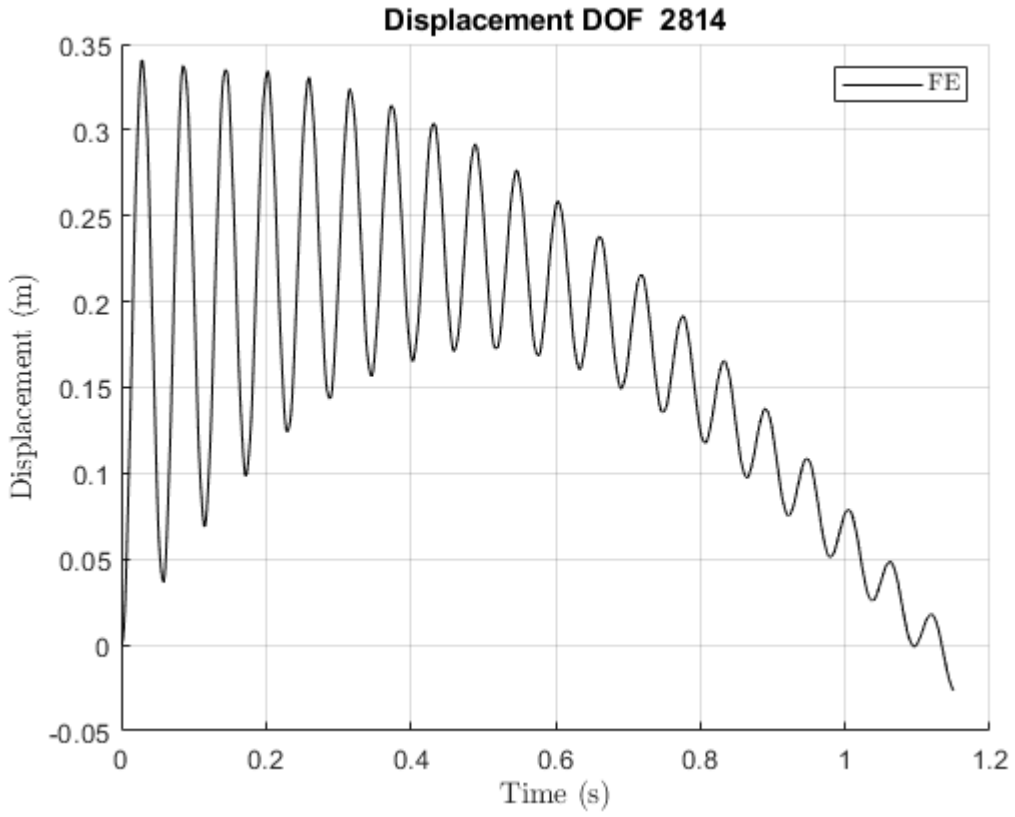

Figure 6.4: Displacement of DOF 2814 through time, caused by the external force represented in figure 6.2. *Source: Own elaboration.*

Regarding the displacement evolution, one can easily identify the damping effect explained in section 4.4.2: the movement's amplitude decreases over time. Given the fact that the damping effect is proportional to the velocity of vibration and thus looking at figure 6.5, the damping phenomena depicted in figure 6.4 must be strongly present at the beginning of the motion, where the velocity is higher.

Furthermore, once the damping effect weakens, the structure behaviour becomes steady. This steadiness is determined by the external force, since it is then the only responsible for exciting the movement of the structure. Hence, if one compares the external force represented in figure 6.2 with the steady stage of the displacement curve 6.4, it can be noted that the structure vibrates in concordance with the external force.

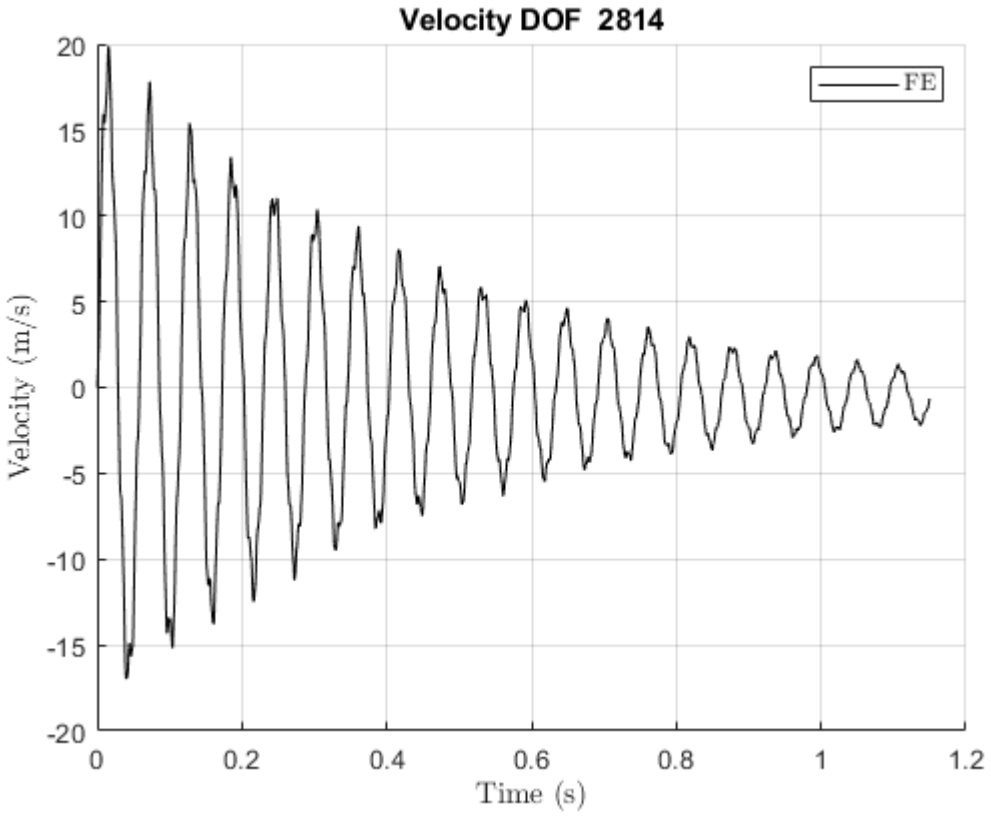

Figure 6.5: Velocity of DOF 2814 thorugh time, caused by the external force represented in figure 6.2. *Source: Own elaboration.*

In terms of the velocity, both the damping effect and the steady response are also clearly visible. However, the steady response is different from the one in figure 6.4, since it is defined by the derivative of the external force.

To assess the possible error of the simulation, it is also useful to plot the total energy of the response, which can be obtained by summing up both the kinetic and the strain energy. Bearing in mind that those energies are obtained from squaring the velocity and displacement respectively, spotting an error would be easier in this case as it would also be squared up.
In matrix format, the kinetic and strain energy can be computed as:

$$\mathcal{K} = \frac{1}{2}\mathrm{v}^T M \mathrm{v} \tag{6.5}$$

$$\mathcal{U} = \frac{1}{2} d^T K d \tag{6.6}$$

Where K and M are the mass and stiffness matrices respectively.

Hence, the energy of the system results in:

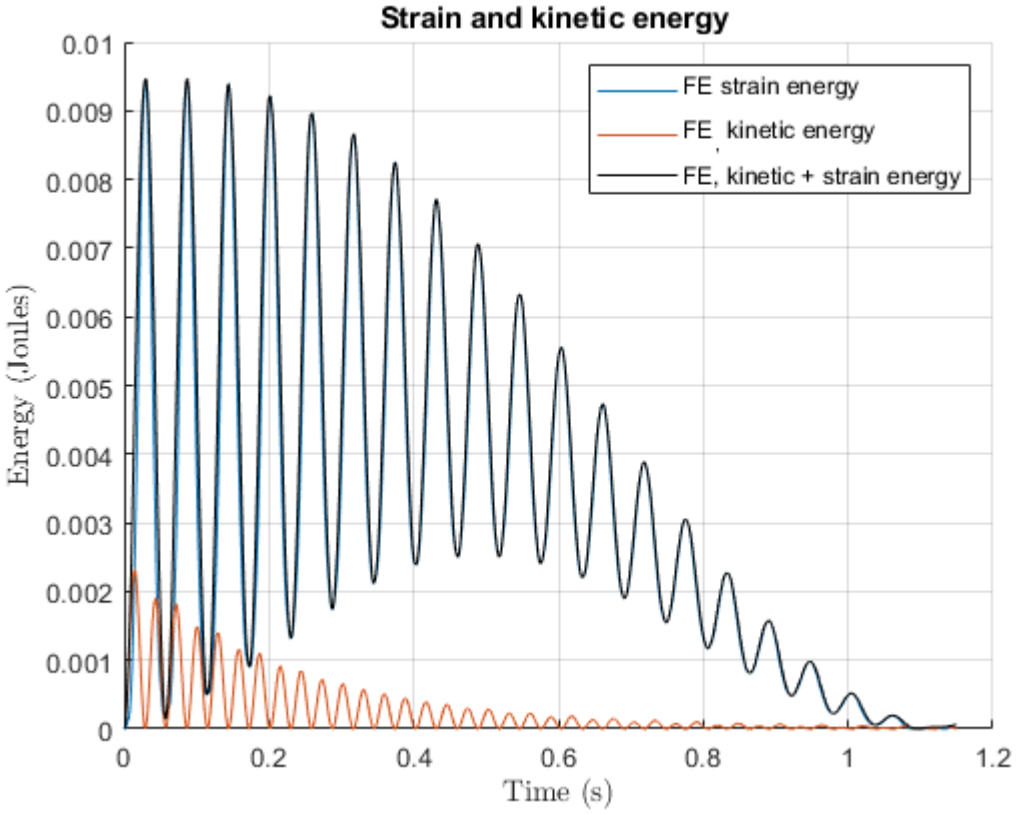

Figure 6.6: Strain, kinetic and total energy of the system through time.
Source: Own elaboration.

According to the preceding figure, the strain energy is significantly higher than the kinetic energy, which suggests that the stiffness of the material is considerably larger than its density. According to table 3.1, aluminium is a really resistant material with a high Young modulus, and it is also really light thanks to its low density.

To assess the precision of the FE analysis, it is necessary to have the real response of the structure. Since the student does not count on such information, it must be calculated analytically.
As mentioned in previous sections, the analytical solution that is used to check the accuracy of the FE analysis is the one obtained with the modal analysis decomposition in section 4.4.

The solution of the forced damped vibrations problem is expressed in equation 4.94, and it is composed of a homogeneous solution (which depend on constants A_i and B_i) and a particular solution that will depend on the external force.
Section 4.4.2 deduces the particular solution for an external force formed by a single harmonic function, i.e one single sine. Substituting the particular solution expressed in equation 4.97 in 4.94, yields:

$$q_i(t) = q_i^{max}\left(e^{-\bar{\xi}_i\omega_i t}\left(A_i cos(\bar{\omega}_i t) + sin(\bar{\omega}_i t)\right) + \left(1-\bar{\rho}_i^2\right) sin(\Omega t+\varphi) - 2\bar{\xi}_i\bar{\rho}_i\, cos(\Omega t+\varphi)\right) \tag{6.7}$$

And, according to equation 4.77, the nodal displacements vector is computed as (only for the unrestricted

DOFs):

$$d_l = \sum_{i=1}^{n_{modes}} \phi_{l_i} q_i^{max} \left(e^{-\bar{\xi}_i \omega_i t} \left(A_i cos(\bar{\omega}_i t) + sin(\bar{\omega}_i t) \right) + \left(1 - \bar{\rho}_i^2 \right) sin(\Omega t + \varphi) - 2\bar{\xi}_i \bar{\rho}_i \, cos(\Omega t + \varphi) \right) \tag{6.8}$$

The velocity response is obtained by deriving the previous equation.

Relaunching the simulation with the modal analysis added to the code one can compare the results:

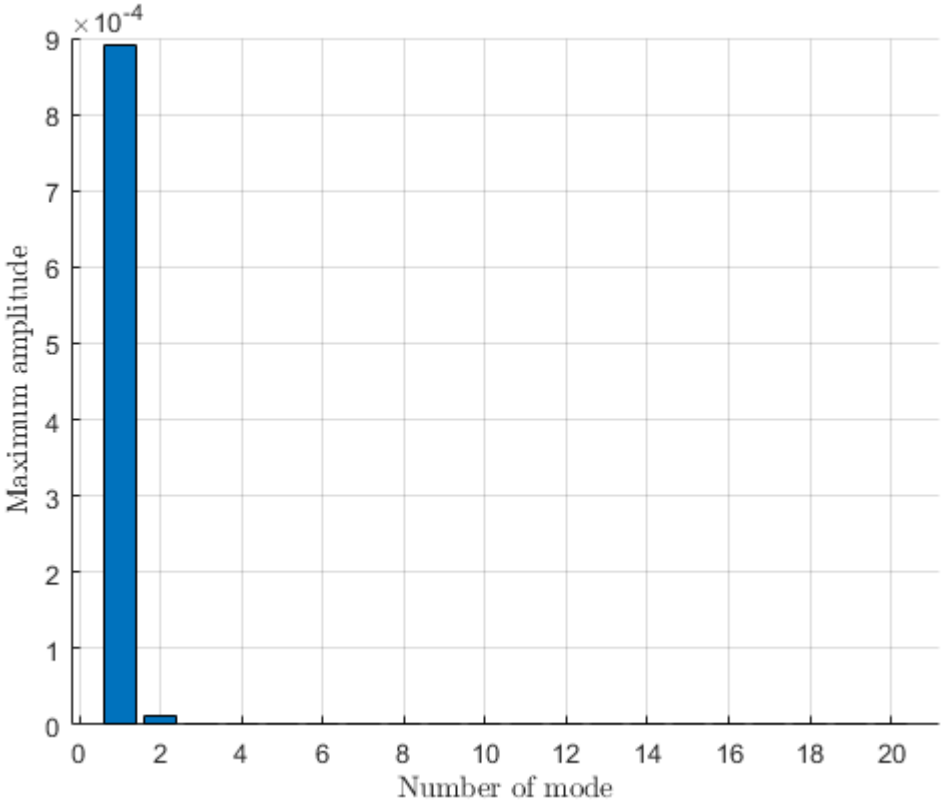

Figure 6.7: Maximum amplitude q_i^{max} of each mode of vibration ϕ_i.
Source: Own elaboration.

One of the main advantages of the modal decomposition analyses is that, as depicted in figure 6.7, one is able to know which natural modes of vibration of the structure are triggered.

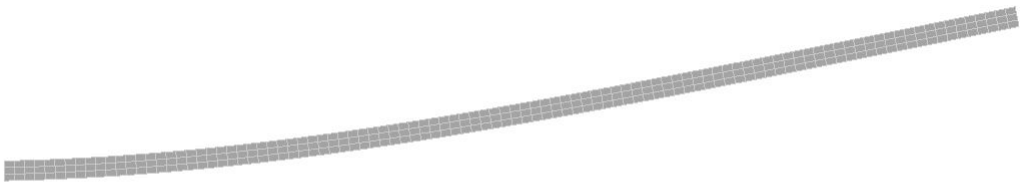

Figure 6.8: Snapshot of the 1^{st} natural mode of the structure.
Source: Own elaboration.

In this case, only the two first modes are activated, being the first one the most dominant one by far. The reason behind it is that the frequency of the external force, i.e 1/3 Hz, is closer to the first natural frequency of the structure than to any of the other natural frequencies.

These modes, as one would expect, represent bending motion (every mode shape is included in section 1 of the Annex document), which suggests that the structure will vibrate periodically and slightly reducing its amplitude of movement due to the damping effect that can be observed in figure 6.4.

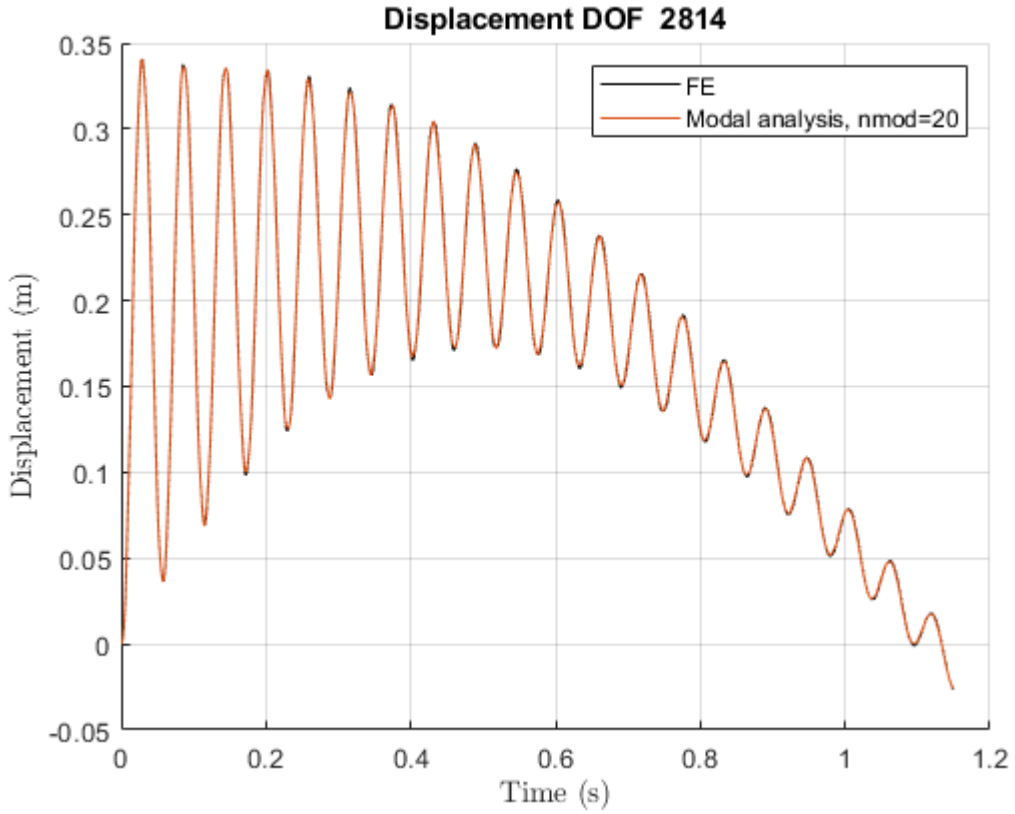

Figure 6.9: Comparison between the 2814^{th} DOF displacement obtained by the FE analysis and the one deduced from the modal decomposition analysis.
Source: Own elaboration.

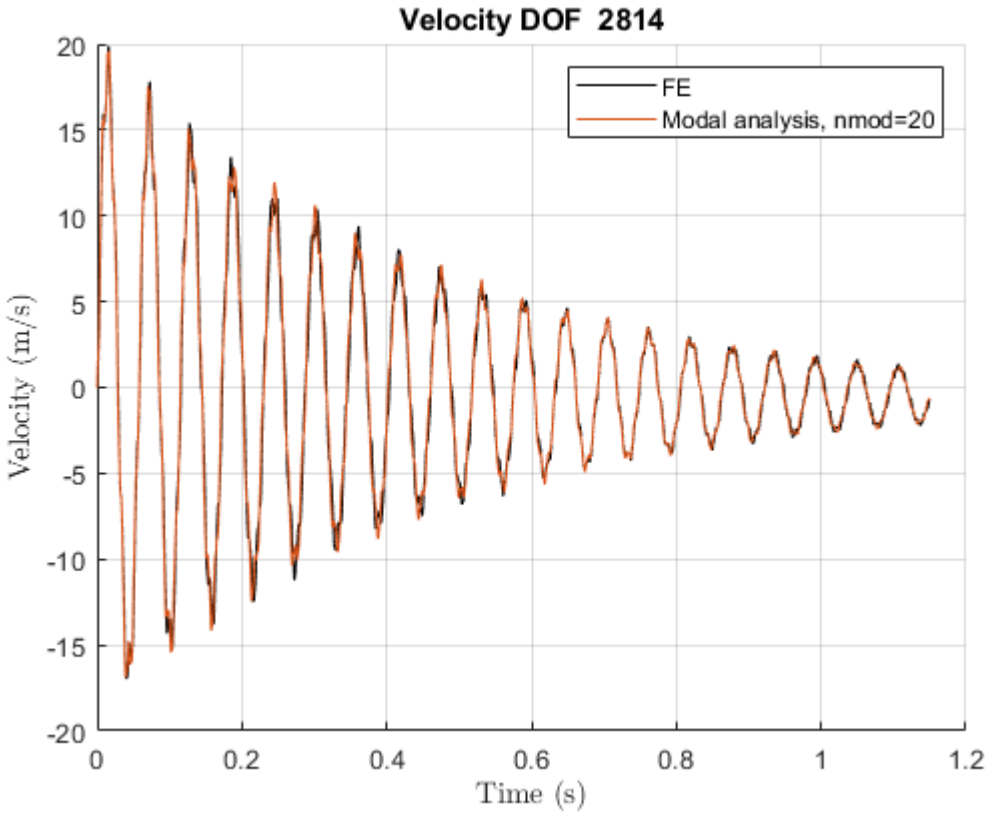

Figure 6.10: Comparison between the 2814^{th} DOF velocity obtained by the FE analysis and the one deduced from the modal decomposition analysis.
Source: Own elaboration.

Taking a look into both figures 6.9 and 6.10, one can observe two distinct features.

On the one hand, the transient and steady responses are also captured by the modal decomposition analysis, and can be explained with equation 6.8: the transient stage is associated to the homogeneous solution while the steady stage corresponds to the particular solution.

On the other hand, both methods match perfectly, which, in principle, would indicate that the FE analysis is a legitimate tool to compute the dynamic response of the structure under the conditions specified in this case of study.
Nonetheless, the energies will also be compared to assure that the preceding statement is correct. To avoid overloading the plot with too many curves, only the total energy is compared.

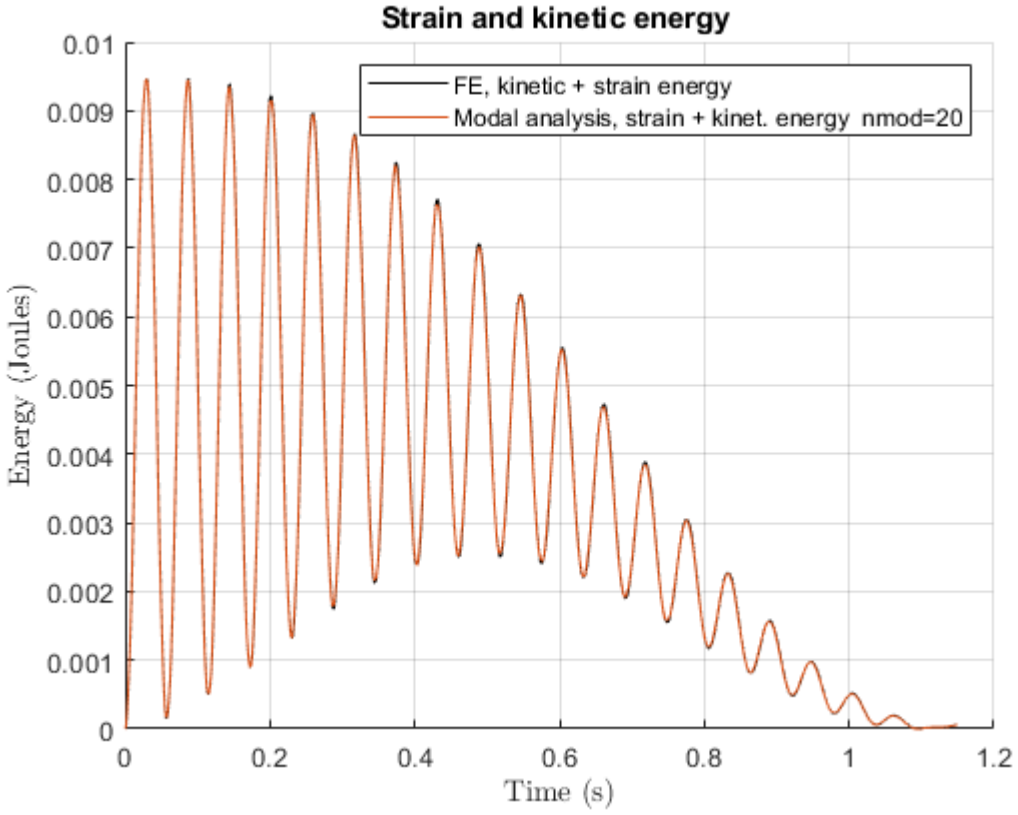

Figure 6.11: Comparison between the 2814^{th} DOF energy obtained by the FE analysis and the one deduced from the modal decomposition analysis.
Source: Own elaboration.

According to [34], the time constant τ is a widely used concept to study in damped systems. It essentially indicates how much time must elapse for the response to have decayed by approximately 63.2%. In other words, when τ is reached, the energy of the system is roughly a 36.8% of its maximum value.
In a second order ODE, the time value τ is given by:

$$m\frac{d^2x}{dt^2} + b\frac{dx}{dt} + kx = 0 \rightarrow \tau = \frac{2m}{b} \tag{6.9}$$

Comparing the form of this ODE with the forced damped vibrations ODE (see equation 4.91), and according to equation 6.2, τ is estimated as:

$$\tau = \frac{2m}{b} = \frac{2}{2\bar{\xi}_i\omega_i} = \frac{2}{\bar{\alpha}} = 0.457\ s \tag{6.10}$$

As detailed below, the amplitude of the displacement oscillation that takes place around 0.457 seconds is approximately 0.116 meters, whilst the maximum amplitude of the displacement, which is given at the beginning of the response, is roughly 0.339.
Since the energy of a sinusoidal wave can be estimated with its amplitude, the energy of the oscillation that occurs around 0.457 is 34.27% the energy of the maximum amplitude.
Given that the above-mentioned procedure relies on big approximations to obtain a visual idea of the energy

decrease, the precision is considered acceptable and thus the value of τ for the FEM response is accepted as approximately 0.457 seconds.

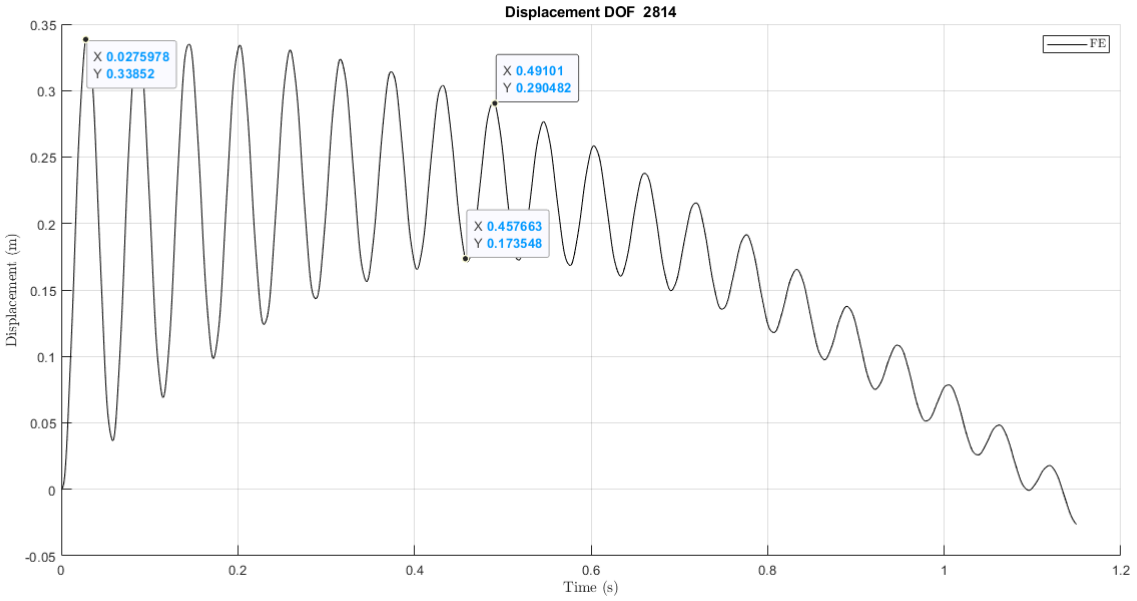

Figure 6.12: Representation of the energy of the system computed by the FEM at different instants. *Source: Own elaboration.*

It is now clear that the FEM is legitimate when trying to study the dynamic response of the structure when the external force is formed by a low frequency sine.

Nevertheless, since one of the main objectives of the project is to study the structure response to the wind, one must assure that the FEM is also successful when faced with external forces that consist on a combination of several sinusoidal functions.
It must be noted that, when working with Fourier expansions, the combination of different frequencies can produce narrow-width peaks, which are characteristic of higher frequency sines. Thus, high frequencies are also of interest and it is convenient to take them into account when defining the optimal number of time steps.

6.2.3 Harmonic Expansion Force

Once the foundations have been laid, one can consider launching a simulation with an external force constituted by a combination of sines with increasing frequencies Ω.
As it has been repeated, this case of study is done in order to simulate how the code would behave when a combination consisting on a larger number of sines is introduced (i.e the Fourier Series extracted from the FFT results in the following section 6.3).

The resulting external force function is illustrated in figure 6.13 and is formed by the sum of 10 different sines, which have the upcoming characteristics (being the first one the low frequency sine analysed in the

previous section 6.2.2):

$$\bar{F} = \begin{bmatrix} 0.1 & 0.02 & 0.005 & -0.6 & 0.9 & 1.2 & 0.03 & -0.7 & 0.8 & -1.1 \end{bmatrix}$$

$$\Omega = 2\pi f = 2\pi \begin{bmatrix} 1/3 & 2 & 10 & 50 & 120 & 350 & 400 & 680 & 830 & 1010 \end{bmatrix} \tag{6.11}$$

$$\varphi = \pi \begin{bmatrix} 1/4 & 0 & 1/2 & 7/4 & 8/7 & 3/2 & 0 & 5 & 1/6 & 9/5 \end{bmatrix}$$

Hence, the external force applied on the structure's top surface is given by:

$$F^{ext}(t) = \sum_{k=1}^{10} \bar{F}_k \; sin(\Omega_k t + \varphi_k) \tag{6.12}$$

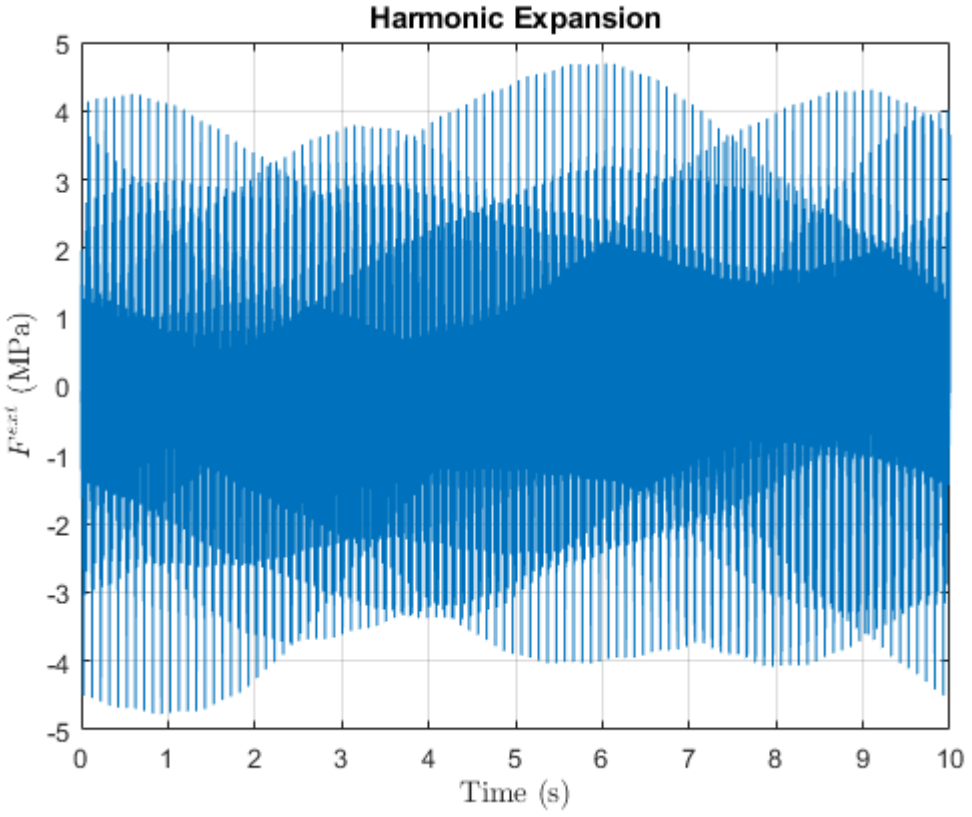

Figure 6.13: Time evolution of an external force consisting on the combination of sinusoidal functions detailed in expression 6.11.
Source: Own elaboration.

Given the fact that the simulation will initially cover a time domain of less than 2 seconds, figure 6.13 is zoomed in to better appreciate this mentioned interval:

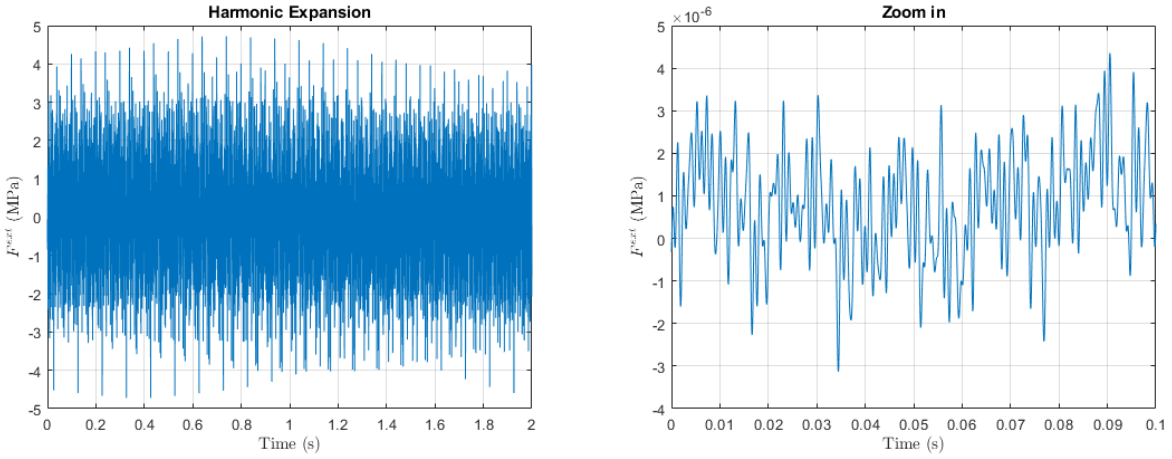

(a) External Force

(b) Zoom in

Figure 6.14: Enlargement of figure 6.13 in the 0-2 seconds domain (a), and zoom in of the external force (b). *Source: Own elaboration.*

Notice that, since the frequency is much higher than in the preceding case, the time domain has been drastically cut to just 0.01 seconds in order to better visualize the narrow oscillations.

Combining a set of sines with different frequencies translates into a noisy and aperiodic function that contains much more oscillations during the same period of time in comparison to the low frequency sine studied in the previous section. Hence, more time steps are required in order to capture those narrow-peaked oscillations. To determine the optimal number of steps, one can define an appropriate number of points that would define a sinusoidal wave. According to figure 6.15, 10 points seem to be the best idea.

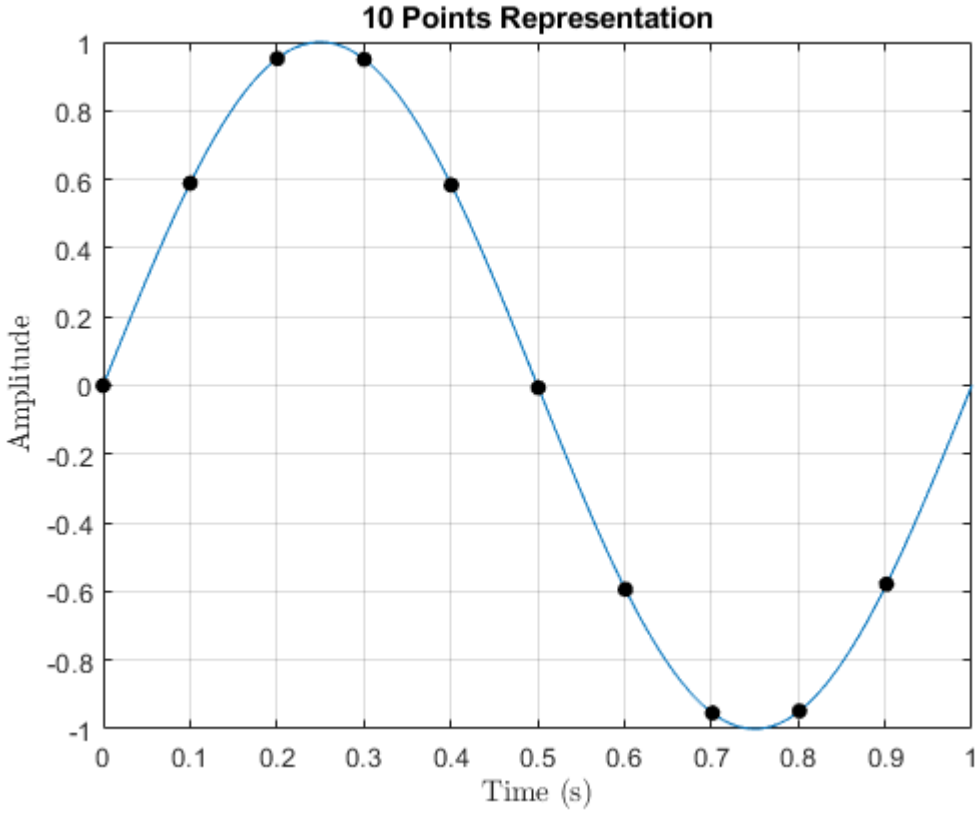

Figure 6.15: Location of the 10 points that optimally represent a sinusoidal wave.
Source: Own elaboration.

Less points could imply too few information in simulations where the time domain is short and the frequency of external force is low, like in the previous case 6.4. If that happened, the code could interpret the external force as a linear function.
On the contrary, too many data points would translate into a greater computational effort and a waste of valuable time when launching simulations.

Hence, the method to estimate the required number of time steps, which will be carried out hereinafter, consists on multiplying the number of oscillations that occur during the specified time domain by 10, the number of data points that will determine every oscillation.
Taking a look into figure 6.14, one can easily calculate the number of oscillations of the external force by t_{end}/T, where t_{end} is the time domain of 1.15 seconds and T is the period of the external force. The 10 point criteria is applied to the sine with the greatest frequency of the combination, i.e 1010 Hz.
Hence, the number of oscillations is 1161.5 and, consequently, the number of time steps must increase from 4000 to 11615.

The analytical solution given by the modal decomposition analysis for the case of an external force formed by a sine expansion can be found in equation 4.101 (see section 4.4.2).

Updating the inputs and adapting the code to make it able to cope with an external force represented by equation 6.12, the dynamic response is synthesized in the following figures. To avoid repeating simulations, the FEM and modal results will be hereafter represented in the same plot, except if a more in-depth analysis of a result is required.

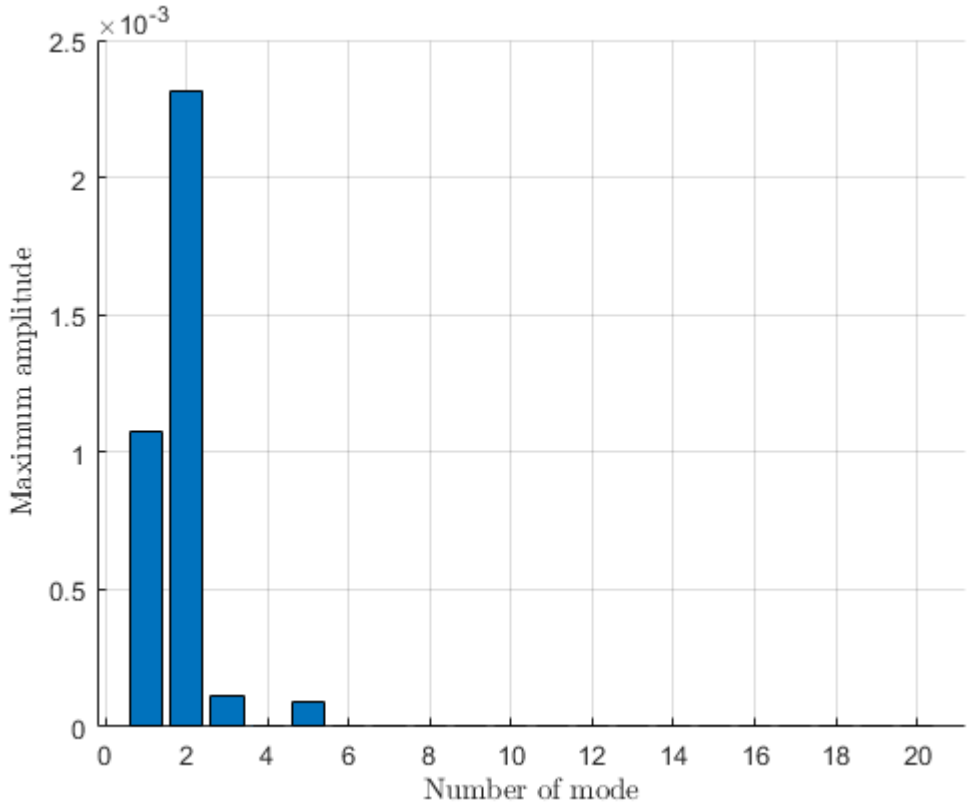

Figure 6.16: Maximum amplitude q_i^{max} of each mode of vibration ϕ_i.
Source: Own elaboration.

In this case, as the external force consist on a combination of sines with different frequencies Ω, figure 6.16 shows that the dynamic response is formed by 4 different modes of vibration.

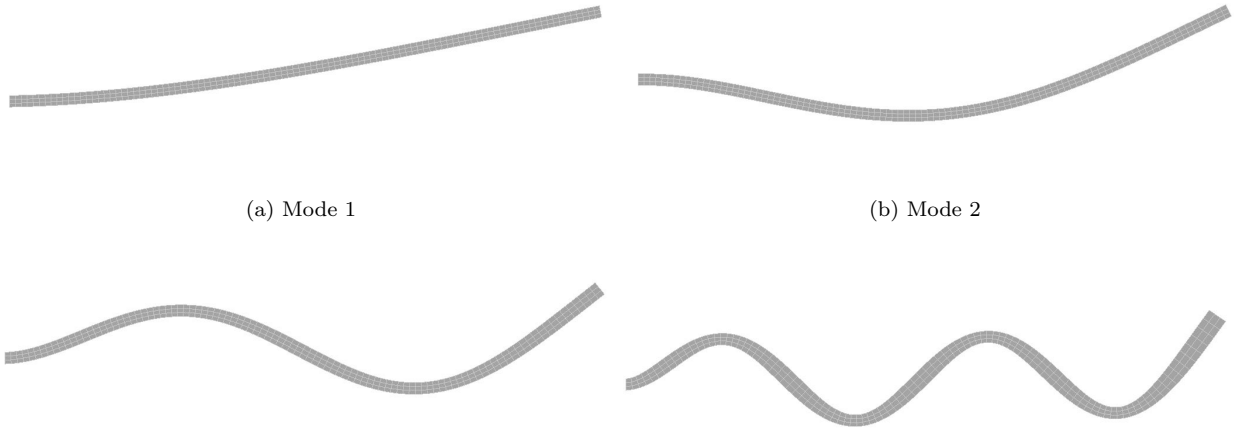

(a) Mode 1

(b) Mode 2

(c) Mode 3

(d) Mode 5

Figure 6.17: Snapshot of the 4 different natural modes of vibration that contribute to the dynamic response of the beam.
Source: Own elaboration.

Likewise in the other simulations, these modes all represent bending motions.

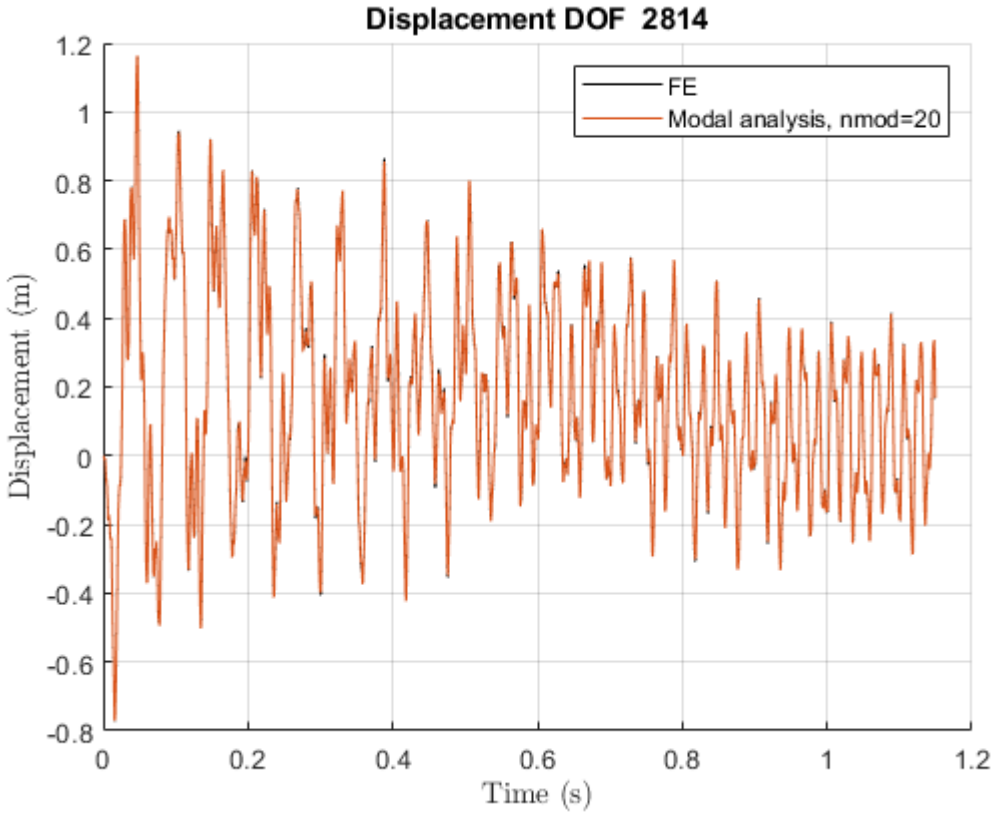

Figure 6.18: Comparison between the 2814^{th} DOF displacement obtained by the FE analysis and the one deduced from the modal decomposition analysis.
Source: Own elaboration.

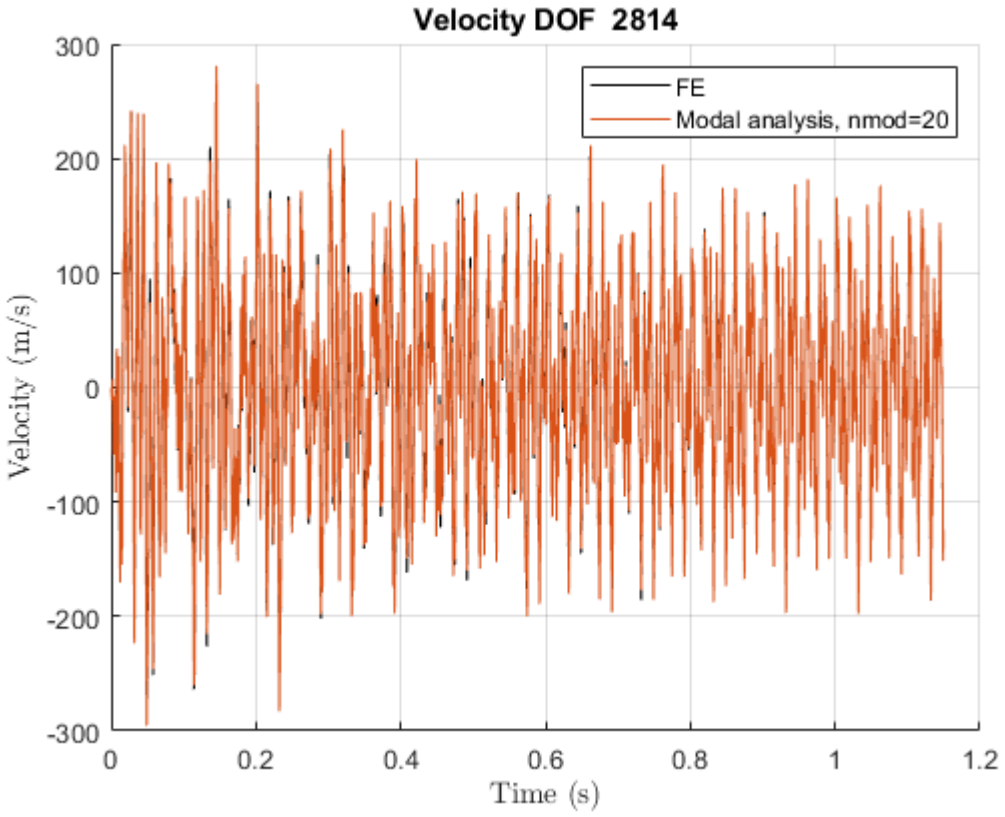

Figure 6.19: Comparison between the 2814^{th} DOF velocity obtained by the FE analysis and the one deduced from the modal decomposition analysis.
Source: Own elaboration.

As observed in figures 6.18 and 6.19, considering a sine combination instead of only one sine contributes to the creation of noisy and aperiodic responses.

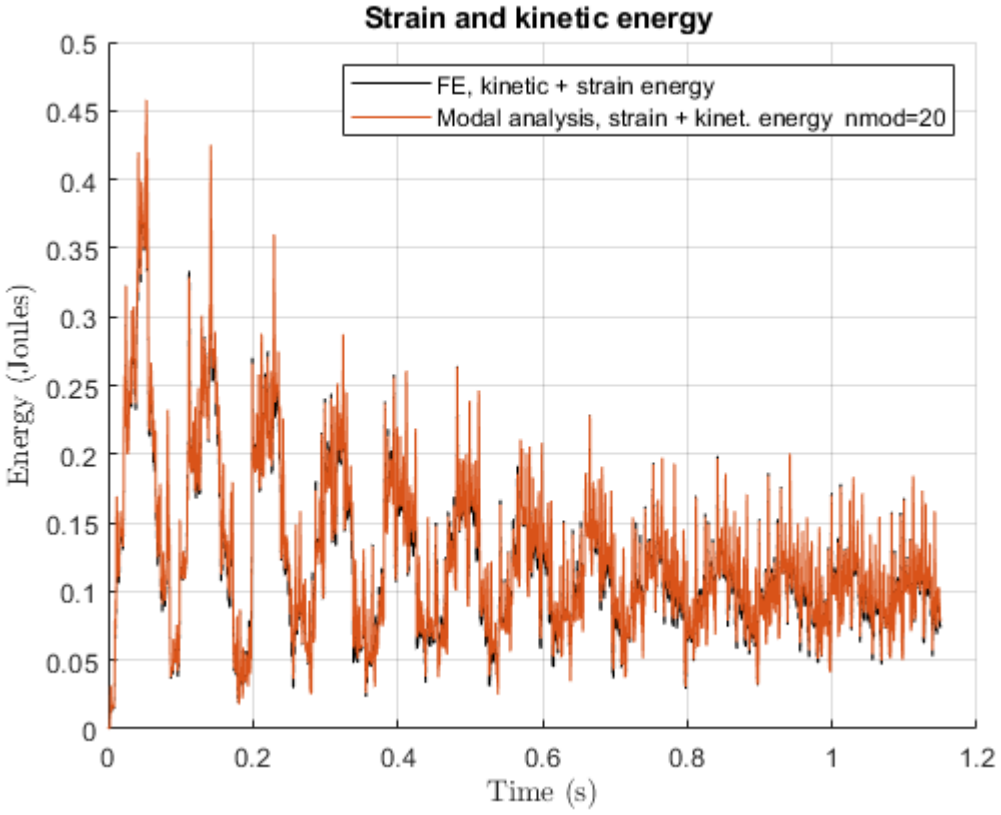

Figure 6.20: Comparison between the 2814^{th} DOF energy obtained by the FE analysis and the one deduced from the modal decomposition analysis.
Source: Own elaboration.

According to figure 6.20, the FEM matches almost perfectly with the modal analysis for 11615 time steps. The mismatch that can be seen in figures 6.19 and 6.20, although seeming insignificant, must to be taken into account.

The noisy and narrow-peaked shape of sine combination functions facilitate the formation of peaks with widths even narrower than the ones associated to the sine with the greatest frequency (in this case $\Omega_{10} = 2020\pi\ rad/s$). Hence, it appears that, for sine combinations, the 10 point criteria that has been defined in this section for estimating the time steps should be increased if more precision was desired.

In such context, the code is considered capable of obtaining the dynamic response of the structure caused by the wind action. However, an intermediate step is needed in order to introduce the wind data as code input, since it requires external forces to be represented by continuous time-dependant functions.

6.3 Fourier Expansion

As explained in section 4.5, the DFT and its computationally efficient computation, the FFT, can be used to depict a discrete set of data in the time domain into its equivalent frequency domain representation.

Its main application in this thesis is its potential to convert empirical measurements of real gusts of wind

speed into continuous time-dependant function represented by a Fourier expansion.

All the procedures that will be detailed in the following sections are included in the Fourier code (see chapter 2 in the Annexes document).

6.3.1 From FFT to Fourier Expansion

According to section 4.5, this Fourier expansion is similar to the one in equation 4.104, but in the time domain:

$$g(t) = \frac{a_0}{2} + \sum_{k=1}^{\infty} a_k cos\left(\frac{2\pi k}{L}t\right) + b_k sin\left(\frac{2\pi k}{L}t\right) = \frac{a_0}{2} + \sum_{k=1}^{\infty} a_k cos\left(2\pi \mathrm{f}_k t\right) + b_k sin\left(2\pi \mathrm{f}_k t\right) \tag{6.13}$$

Where f_k is the frequency in Hertz of each sine/cosine combination and $\Omega_k = 2\pi \mathrm{f}_k$. However, since $g(t)$ will be extracted from the outputs of the FFT algorithm, the preceding equation must be slightly adapted.
For reasons of convenience that will be later justified, it is more convenient to write the Fourier expansion exclusively with sines, since the previous simulations in section 6.2 have been dealing with sines instead of cosines.
Considering that any sine and cosine combination can be represented by a single sine as:

$$a_k cos(\Omega t) + b_k sin(\Omega t) = A_k sin(\Omega t + \varphi) \tag{6.14}$$

$g(t)$ is then given by:

$$g(t) = A_0 + \sum_{k=1}^{\infty} A_k sin\left(\Omega_k t + \varphi_k\right) \tag{6.15}$$

Where $A_0 = a_0/2$.

According to equation 4.113 in section 4.5, the system of equations that one is faced with when conducting a Fourier Transform has complex-valued results ($\hat{f}$ vector). The physical interpretation behind $\hat{f}$, which will be detailed below, enables one to extract an amplitude A_k, and a phase φ_k that fit perfectly with the adapted Fourier expansion in 6.15.

As mentioned, the interpretation of $\hat{f}$ is of utmost importance if one wants to construct a time-dependant function from the real data.
The magnitude of the Fourier coefficient is related to the amplitude of the sine or cosine. This amplitude can be computed as [35]:

$$A_k = \frac{1}{N}\|\hat{f}_k\| \tag{6.16}$$

Where N is the number of samples.

On the other side, the phase identifies how much of a sine/cosine behaviour has the corresponding frequency. In other words, the phase indicates how shifted is the sine or cosine, and it is obtained by taking the imaginary part of $\hat{f}$:

$$\varphi_k = \mathrm{Im}(\hat{f}_k) \tag{6.17}$$

Provided that $\hat{f}$ belongs to the frequency domain, its magnitude and phase are usually represented with frequency spectrum similar to the ones depicted in figures 6.21 and 6.22. Such figures are obtained from the FFT of the following signal:

$$f(t) = sin(4\pi t) + 3sin(10\pi t) \tag{6.18}$$

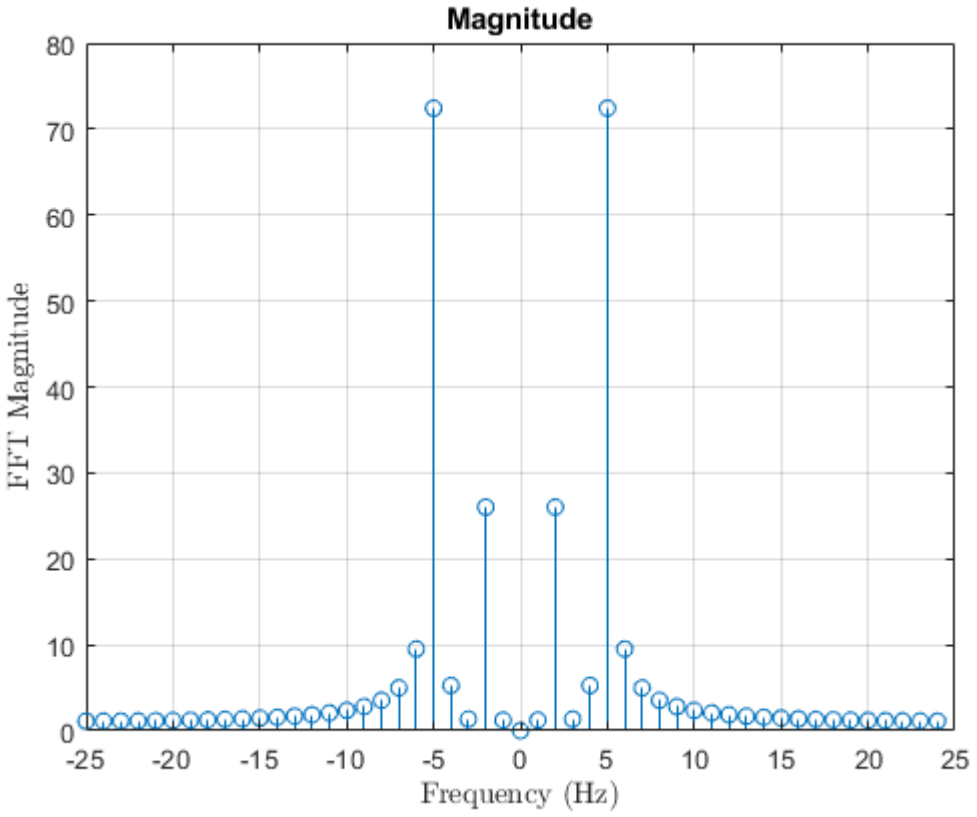

Figure 6.21: Representation of the magnitude $||\hat{f}_k||$ of each frequency f_k.
Source: Own elaboration.

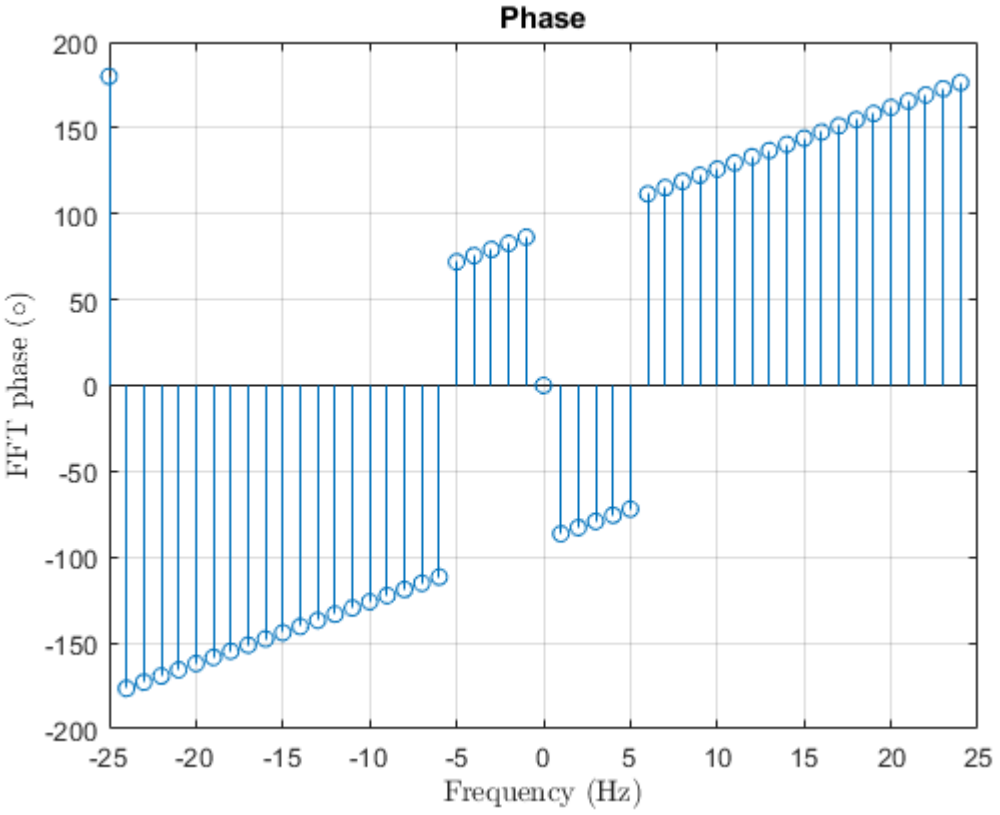

Figure 6.22: Representation of the phase φ_k of each frequency f_k.
Source: Own elaboration.

As it can be seen, the spectrum indicates the magnitude and phase associated to each frequency. These frequencies are symmetrically distributed, being $f = 0\ Hz$ the point of symmetry. In the spectrum, the point of symmetry is found in the $N/2 + 1$ index.
Moreover, f is not an output of the FFT, and is instead arbitrarily constructed, keeping in mind that the zero frequency must be located at index $N/2 + 1$:

$$f = \frac{f_s}{N}\left[-\frac{N}{2} \quad -\frac{N}{2}+1 \quad \dots \quad 0 \quad \dots \quad \frac{N}{2}-2 \quad \frac{N}{2}-1\right] \tag{6.19}$$

Where f_s is the sampling rate, or the number of measurements performed in a second. To guarantee that the FFT gives out satisfactory results, it is indispensable for the real data to be measured at a constant rate f_s. If this requirement is respected, the sampling rate can be calculated as:

$$f_s = \frac{N_T}{T} \tag{6.20}$$

Where T is the period of the signal and N_T is the number of samples per period. In aperiodic signals like the one selected for this study (see figure 6.24), the entire time domain is considered their actual period T and $N_T = N$. Hence, the FFT gives out the amplitudes and phases of a signal which has the same shape as the original discrete representation and which is periodic at intervals of T seconds.

Considering that negative frequencies do not have any physical sense, in a practical way, the only *k-indices* that must be considered are $k \in [0,\ \infty)$.
To avoid losing fundamental information from the FFT spectrum after carrying out the truncation of the DFT for only positive frequencies, equation 6.16 must be reformulated as:

$$A_k = \begin{cases} \frac{1}{N}\|\hat{f}_k\| & \text{for} \quad \Omega_k = 0 \\ \frac{2}{N}\|\hat{f}_k\| & \text{for} \quad \Omega_k > 0 \end{cases} \tag{6.21}$$

Notice that, for $\Omega_k = 0$, the amplitude is not doubled. This is due to the symmetry in the spectrum of $\hat{f}$ that has been noted in figure 6.21: since $\Omega_k = 0$ is the symmetry point, its associated information is only computed once.
Moreover, regarding the DFT matrix F in equation 4.113, the zero frequency corresponds to the first row of the mentioned matrix and, thus, $\hat{f}_1 = \sum_{k=1}^{N} f_k$.
By dividing $\hat{f}_1$ by the total number of samples N, one is essentially computing the mean value of the total data set, i.e the offset (A_0) of the signal $g(t)$ in equation 6.15.

According to [36], this method of approaching the FFT would result in a Fourier cosine expansion. Therefore, and considering that $cos(x) = sin(x + \pi/2)$, equation 6.15 must be readapted a final time as follows:

$$g(t) = A_0 + \sum_{k=1}^{N-1} A_k\ sin\left(\Omega_k t + \varphi_k + \frac{\pi}{2}\right) \tag{6.22}$$

6.3.2 Wind Speed Signal Considerations

The selected wind speed data has been obtained from [37]. This paper studies the effects of wind speed fluctuations on the short and long-term power fluctuations that occur in wind turbines.
Figure 6.24 represents the measurements of the wind speed (V_w) in a single point of the turbine's rotor disk during a short period of time.

The conditions that a wind turbine blade faces are similar to the circumstances that this study wants to simulate, i.e real wind gusts applied in nearly sea level and during a relatively short period of time.
Hence, after carefully researching through different articles and researches, it has been concluded that the particular data set represented in the upcoming figure is the most suitable for this thesis.

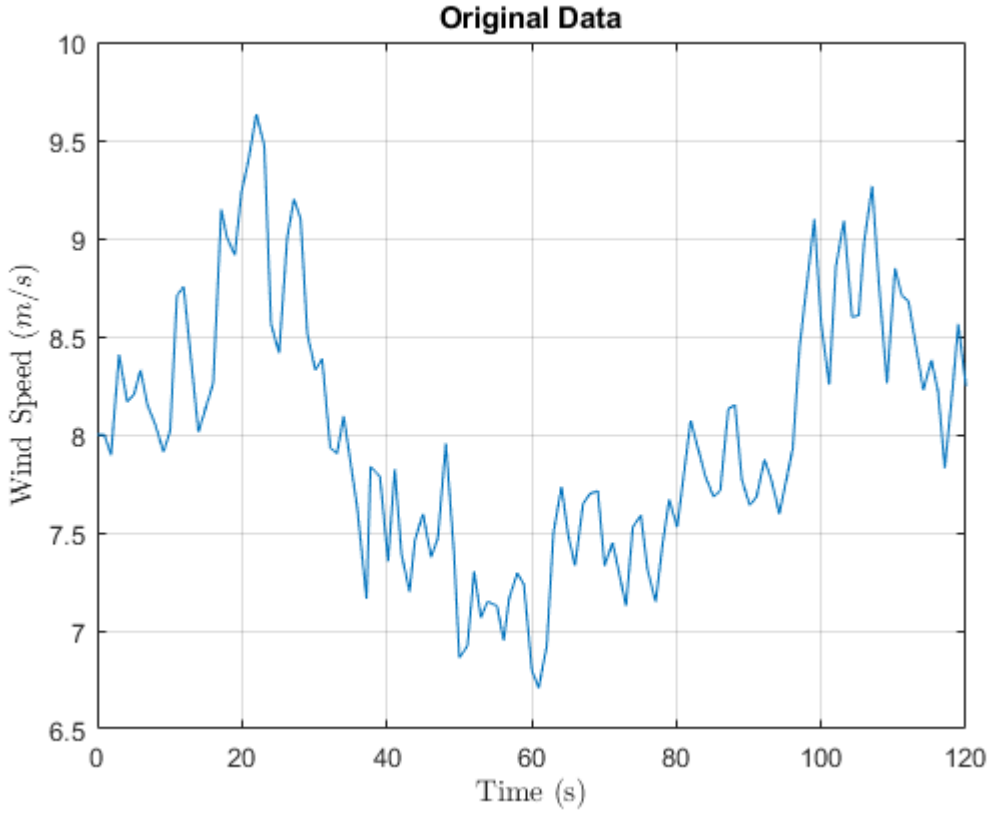

Figure 6.23: Wind speed gusts measured in a single point of a wind turbine rotor disk.
Source: Data extracted from [37].

As it will be further explained in section 6.4, the force produced by the wind is proportional to the square of its speed, i.e V_w^2. That being said, the original discrete signal that will be transformed into a continuous time-dependant function is:

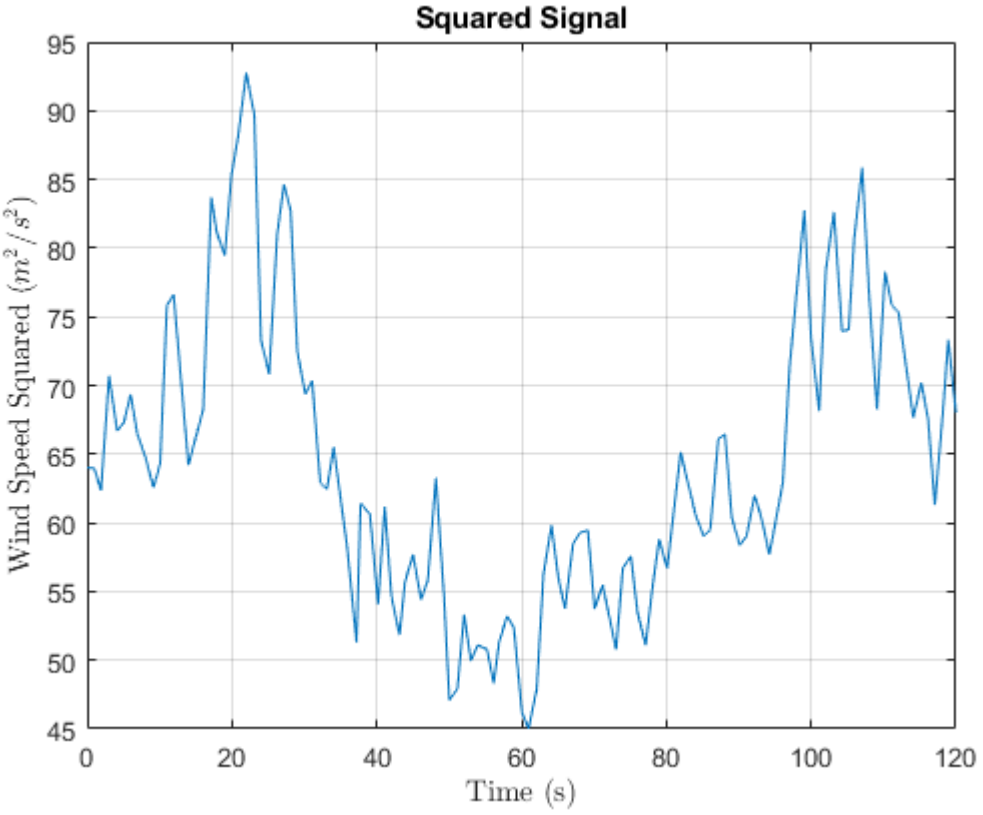

Figure 6.24: Square of the original wind speed data represented in figure 6.23
Source: Data extracted from [37].

After analysing the data set in a deeper sense, one can see that the sampling rate of the signal is not constant and the number of samples (113) is not even.
Such issues complicate the FFT stage, since, as it has been mentioned in the present section and also section 4.5, in order for the FFT to function properly, the number of samples must be even and the sampling rate constant.

To deal with both requirements at the same time, the author has come with a solution which involves interpolating. With this solution, the data set N is reshaped by defining the signal period T and the desired sampling rate f_s.

Adjusting the values of T and f_s based on the characteristics of the signal, requires creating a new time vector t and thus a new vector representing the square of the wind speed measurements V_w^2 at these moments in time. Both V_w^2 and t will then have a dimension N defined by equation 6.20. Thus:

$$N = T\mathrm{f}_s \tag{6.23}$$

Since the signal in figure 6.24 is clearly aperiodic, T is set to 120 seconds and $\mathrm{f}_s = 10\ samples/s$. In such circumstances, the new vectors of time and wind speed will have $N = 1200$ elements, which is intentionally an even value.

Once N is redefined, the time vector is given by:

$$t = \begin{bmatrix} 0 & \frac{1}{\mathrm{f}_s} & \frac{2}{\mathrm{f}_s} & \frac{3}{\mathrm{f}_s} & \dots & \frac{N-1}{\mathrm{f}_s} \end{bmatrix} \tag{6.24}$$

Finally, the new vector of squared wind speed is obtained from a cubic interpolation with the original data set and the new vector of time defined in the previous equation.
This cubic interpolation is possible thanks to the *spline()* Matlab function, which essentially computes the values of V_w^2 that the original signal in figure 6.24 would have for the corresponding values of the new time vector.

To better visualize the approach, figure 6.25 shows the comparison between the original and the interpolated signal, as well as the original data set and the new one:

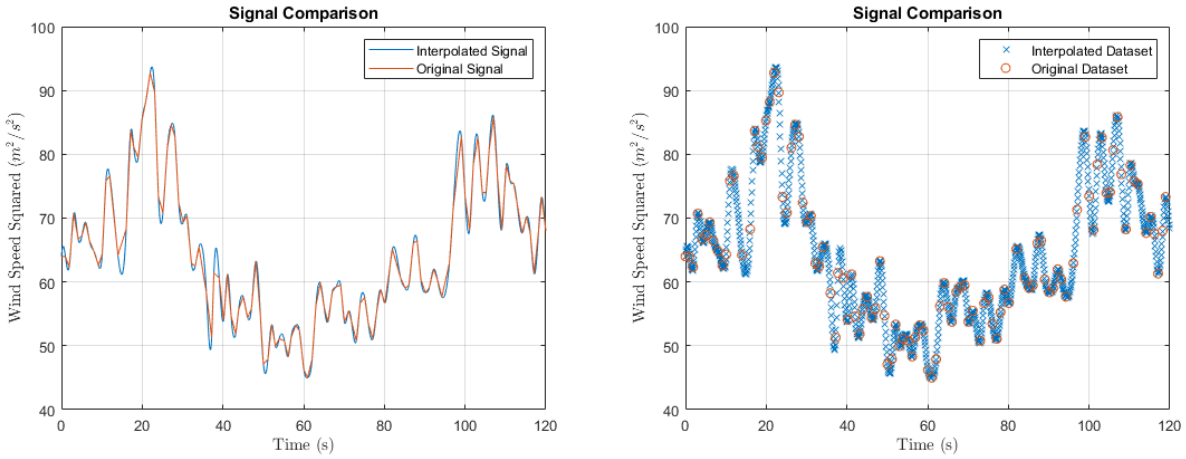

(a) Signal

(b) Dataset

Figure 6.25: Comparison between the original and the interpolated signal (a) and Representation of the original dataset of $N = 113$ and the interpolated dataset of $N = 1200$ (b).
Source: Own elaboration.

As it can be observed, the cubic interpolation is considered legitimate to conduct the FE study, since the mismatches that take place in the previous figure are not sufficient enough to be appreciable in the dynamic response of the structure.
Furthermore, the fact that the interpolated signals finishes at 120 seconds is due to the arbitrary definition of the T parameter. From this instant, the signal repeats itself with intervals of 120 seconds.

Such an approach makes it really easy to extend the procedure to a general point of view. In other words, by defining the period and the sampling rate for subsequently interpolating the signal, one can ultimately achieve a new data set equivalent to the original but much more adequate for the FFT algorithm.
With this pre-process technique, the FFT can be applied to any signal, no matter its shape or periodicity, since the arbitrary values of T and f_s reshape and adapt the original data set into what the FFT requires for the corresponding situation.

Noisy and narrow-peaked signals like the one in the present case require higher sampling frequencies, while smoother signals with lower frequencies can be captured with less samples per second.

6.3.3 Resulting Signal

Running the Fourier code with the interpolated signal, the magnitude and phase spectrum obtained are the following:

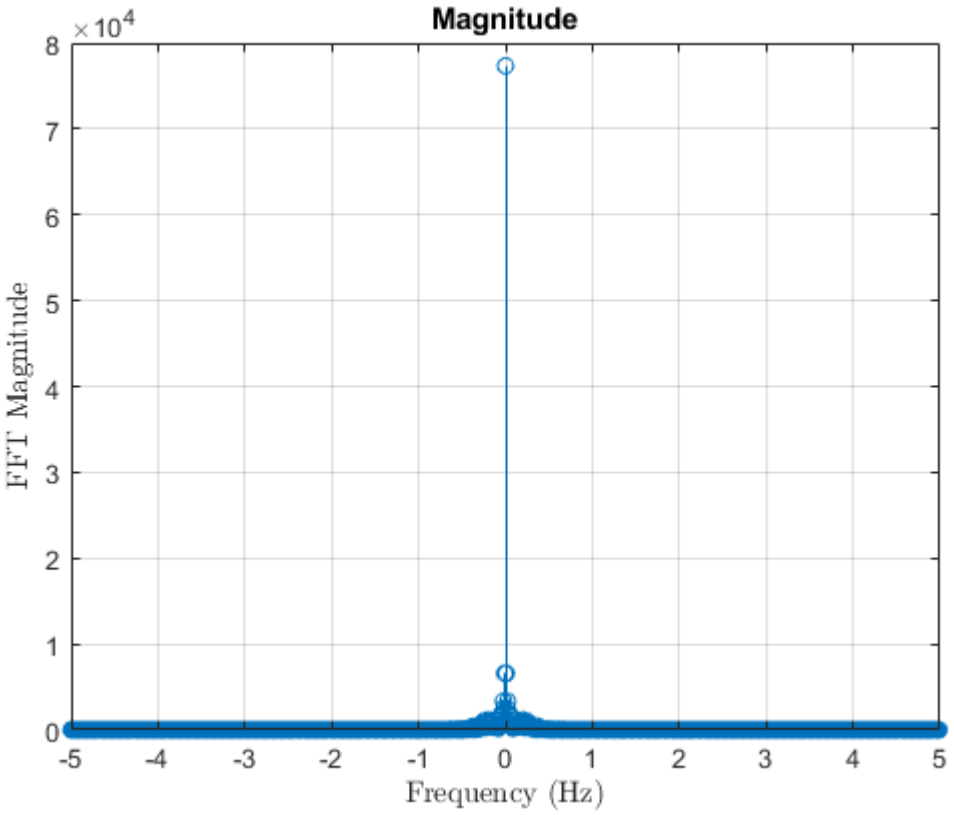

Figure 6.26: Magnitude spectrum of the wind data FFT.
Source: Own elaboration.

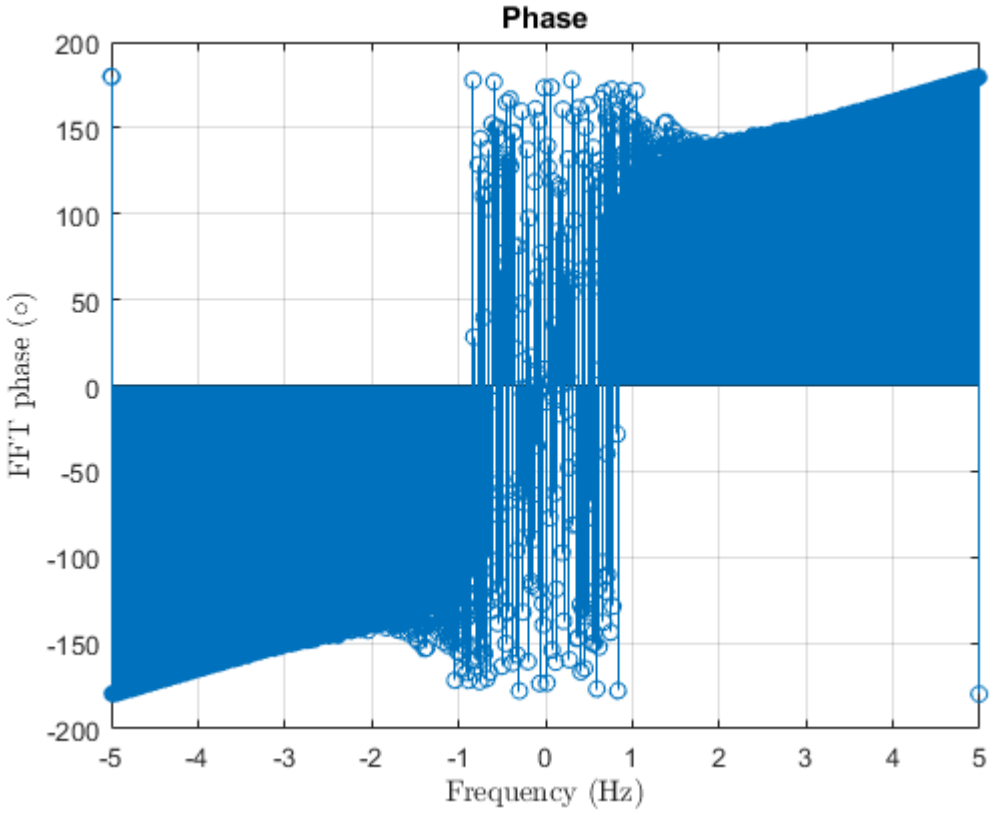

Figure 6.27: Phase spectrum of the wind data FFT.
Source: Own elaboration.

Since the number of samples is $N = 1200$, the Fourier expansion that would result from these results would consist on a combination of 1200 sines.

Launching a simulation with an external force that is formed by such a large amount of sines would be extremely demanding in terms of computational effort. Hence, it is convenient to filter the results.

Taking a look into figure 6.26, one is faced with a really high value of $\hat{f}_1$, which corresponds to the zero frequency.

To give relevance to the rest of the signal, one can get rid of $\hat{f}_1$ and plot the rest of magnitudes:

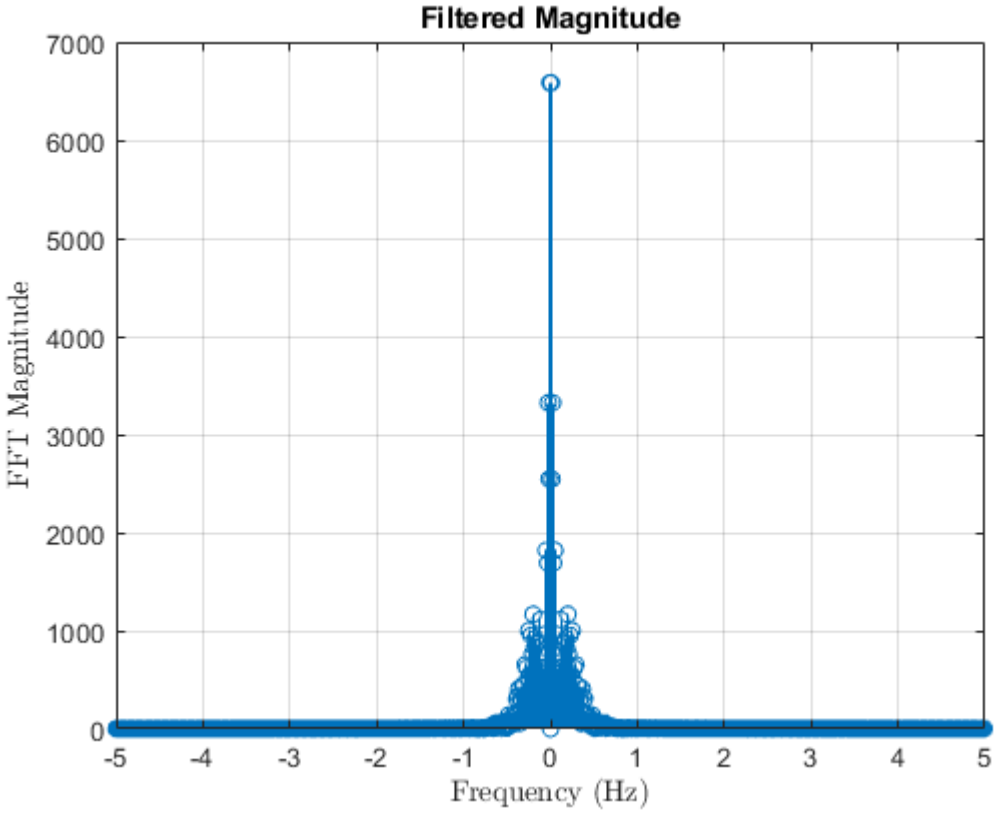

Figure 6.28: Representation of the magnitude spectrum when $\hat{f}_1$ is omitted.
Source: Own elaboration.

After iteratively trying different filtering thresholds and according to figure 6.28, it is determined that all the $\hat{f}$ magnitudes smaller than 200 will be discarded. Therefore, the only *k-indices* that will be considered for the Fourier expansion are the ones that meet the following condition:

$$||\hat{f}_k|| \geq 200 \tag{6.25}$$

Thus, applying this tolerance to equation 6.21, only amplitudes greater than 0.167 will be included.

Applying this criteria, the number of sines is reduced from 1200 to just 43, which represents a 96% decrease. Furthermore, and according to figure 6.29 the resulting filtered signal's accuracy is almost the same as the one obtained with the whole 1200 samples, which, as it can be seen, matches perfectly with the original $N = 113$ dataset (the one represented in figure 6.24).

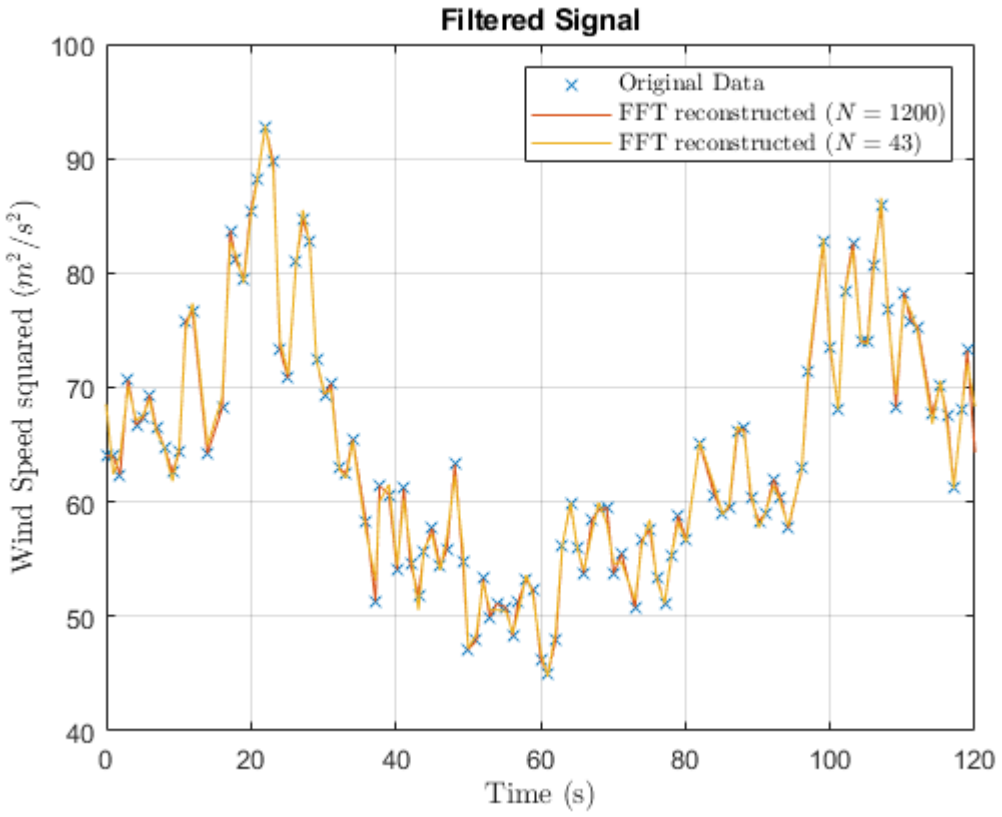

Figure 6.29: Filtered signal, i.e $N = 43$, obtained from the FFT analysis in contrast with the one obtained with $N = 1200$ and the original data.
Source: Own elaboration.

Thus, one is be able to see that the cubic interpolation and the $\hat{f}$ filtering have not contributed to creating a big difference between the final time-dependant function obtained from the FFT and its original discrete form.

Hence, it can be concluded that the approach carried out to obtain the continuous representation of discrete wind speed data does not degrade the original signal and, moreover, it is also quite advantageous in terms of computation, since going from 1200 to 43 sines will save a great deal of time when launching the definite simulation.

6.4 Wind Analysis

This section's objective is to transfer all the valuable data obtained by the FFT analysis into the FE main code, in order to launch a simulation similar to those in section 6.2.

To do so, the problem must be properly formulated, going through the different hypothesis assumptions that need to be adopted.

6.4.1 Problem Statement

In aerodynamics, when a body moves inside a fluid (in this case, the air), there is a good chance that this fluid will cause more pressure on some locations of the body. This pressure gradient is caused mainly because the fluid moves slower at some regions, thus increasing the amount of static pressure, given that the energy has to remain constant (see equation 6.26).

This phenomena is explained with the Navier-Stokes equations. For the sake of simplicity, it is considered that, in this simple case of study, the fluid can be addressed as ideal, i.e incompressible, irrotational, inviscid, and subjected to conservative forces. With such hypothesis and according to [38], the Navier-Stokes equation of energy can be reduced to the famous Bernoulli expression.

It states that the total energy per unit volume of a streamline (P_R), which is equal to the sum of the dynamic pressure q (or the kinetic energy per unit volume), the static pressure P_0 and the potential energy per unit volume U, must be kept constant:

$$P_R = \mathrm{q} + P_0 + \mathrm{U} = \frac{\rho V_w^2}{2} + P_0 + \rho g z \tag{6.26}$$

Where ρ is the air density at a given altitude z. As mentioned, ρ takes the value corresponding to sea level altitude ($\rho_0 = 1.225 kg/m^3$) and, since the fluid is ideal, $\rho = constant$ through the entire simulation.

As it has been observed in the different simulations conducted in section 6.2, the maximum displacements of the structure dynamic response, which are produced at the beam's free end, are not large enough so as to consider noticeable changes in gravity. Therefore, U can be neglected in the above equation.

Moreover, to further simplify the formulation, it is assumed that the structure finds itself in near vacuum conditions. Thus, P_0 can be also ignored.

With such considerations, the expression that describes the energy of the fluid that comes into contact with the beam can be simplified from equation 6.26 to:

$$P_R = \mathrm{q} = \frac{\rho V_w^2}{2} \tag{6.27}$$

The energy of the fluid and consequently, the energy of the beam dynamic response, only depends on the dynamic pressure that the wind applies on the structure. Hence, the external force that the beam will have to withstand, will be proportional to the square of the wind speed V_w^2.

In the previous section, the student has been able to obtain a continuous time-dependant function that describes how does the square of the wind speed behave along time. Since the external force is uniformly distributed on the top surface of the beam, the squared wind speed represented on figure 6.29 is considered to be a constant function in space, i.e the wind gusts are the same at any point of the top surface.

If wind gusts are subjected to the top surface of the beam, there is clearly a pressure gradient between the top and bottom surfaces of the structure and thus, there must be a force trying to return the system to its equilibrium position.

This stress is the result of the high pressure zone trying to compensate the pressure increase and thus trying

to reach the low pressure zone.

In aerodynamics, this resultant force is usually projected into two perpendicular axis, in this case the parallel and perpendicular axis (relative to the wind direction), to form the lift and drag forces respectively:

$$\begin{aligned} L &= \mathrm{q}SC_L \\ D &= \mathrm{q}SC_D \end{aligned} \tag{6.28}$$

Where S refers to the cross section of the structure that the flows sees when projected to the L and D axis, and C_L and C_D are coefficients that indicate the aerodynamic efficiency of the structure.

Technically, the wind speed is only perpendicular to the surface of the beam in the equilibrium position, meaning that when the beam is bending there is a small drag contribution that appears due to the angle between the direction of the wind and the unit outward vector of the surface of the beam (see figure 6.30).

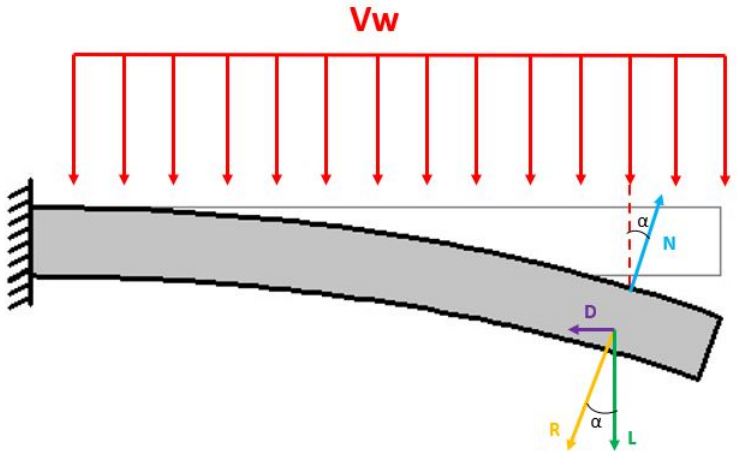

Figure 6.30: Schematic representation of the aerodynamic forces acting on the structure.
Source: Own elaboration.

As it has been already observed in the linear regime, the bending motion that is derived from a uniformly distributed external force produce relatively small displacements. Thus, such displacements are small enough to disregard this previously mentioned drag contribution, since the lift effect is several orders of magnitude greater.

That being said, the only external force present in this problem will be the lift force that is derived from the pressure gradient that the wind speed produces on the structure.

As it is a distributed force along the top surface of the beam, its expression must have units of force per unit surface. Thus:

$$F^{ext}(t) = \frac{L}{S} = \frac{1}{2}\rho V_w^2 C_L \tag{6.29}$$

Since the aerodynamic analysis of the beam is out of the scope of this thesis, it has been supposed that $C_L = 1$.

Furthermore, in order to match the external force units with the code requirements, F^{ext} must be in units of

mega Pascals (MPa). Since the above equation 6.29 has Pascal units ($Pa = N/m^2$), the air density must be scaled by a factor of 10^{-6}, or, in other words, must have units of kg/cm^3.

Introducing the amplitudes A_k, phases φ_k and frequencies Ω_k of the 43 sines that represent the continuous form of V_w^2 and which have been extracted from the FFT in the preceding section, the external force is rewritten as:

$$F^{ext}(t) = \frac{\rho}{2} \sum_{k=1}^{43} A_k sin\left(\Omega_k t + \varphi_k + \frac{\pi}{2}\right) \tag{6.30}$$

6.4.2 Simulation

Likewise in section 6.2.3, the simulation to be launched to estimate the response of the beam under the action of the wind is also addressed with an external force consisting on a sinusoidal combination. In this particular case however, the number of sines is 43 instead of 10, and the properties of those sines, i.e $\bar{F}_k$, φ_k and Ω_k, are determined by the Fourier analysis described in section 6.3.

As a first approach, the inputs are maintained unchanged from those in section 6.2.3 with the exception of the time domain and, consequently, the number of time steps.
As seen in figure 6.24, the wind speed measurements have a duration of approximately 120 seconds, which is almost 120 times larger than the 10 sine expansion simulation in section 6.2.3. Considering that the number of time steps required in that simulation was 11615, the total number of time steps in the present case should be about 120 times that amount, which entails a huge computational effort.
Furthermore, in section 6.2.3 it was found that for sine expansions the optimal number of time steps per period, which was originally considered as 10, should be increased in order to enhance precision.

To avoid laptop overheating, the time domain of the this case of study is cut to 20 seconds and its consequent number of time steps is iteratively estimated to be 23000 after performing several simulations. With this amount of time steps, the computational expense has been 1032.39 seconds, or 17 minutes and 12 seconds (this information will be useful when later comparing the FEM with the HROM).
Taking these considerations in mind, the external force that appears in such time domain in represented below:

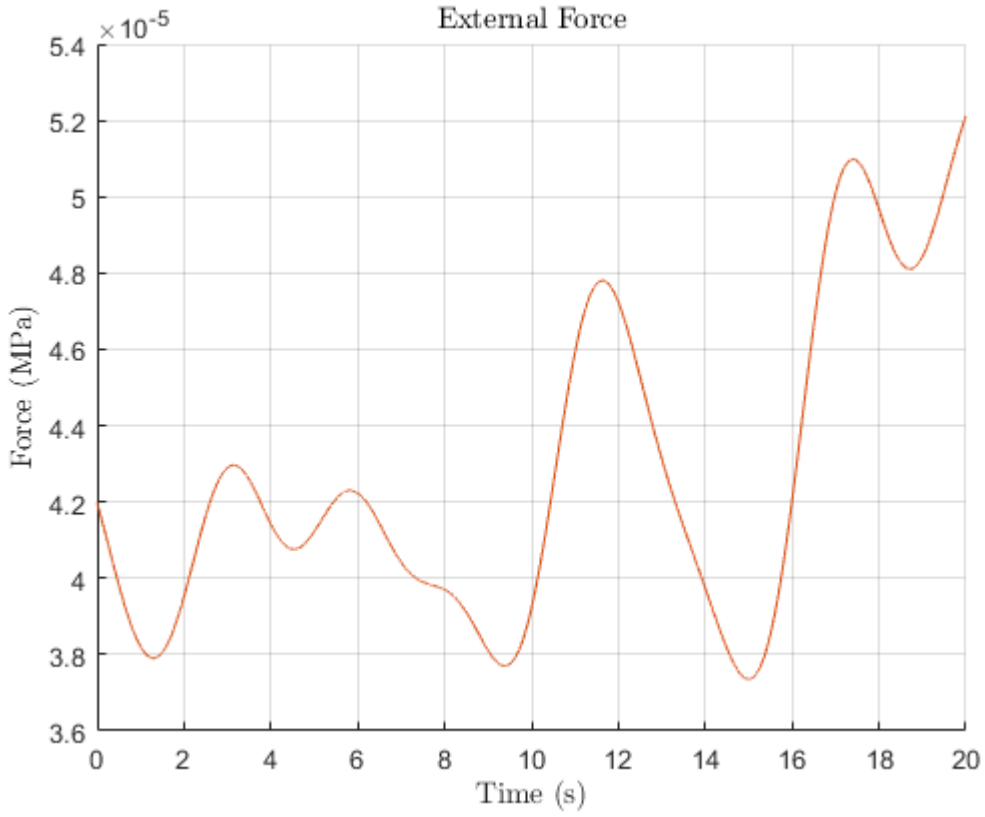

Figure 6.31: Representation of the external force applied in this case of study.
Source: Own elaboration.

And the simulation results in what follows.

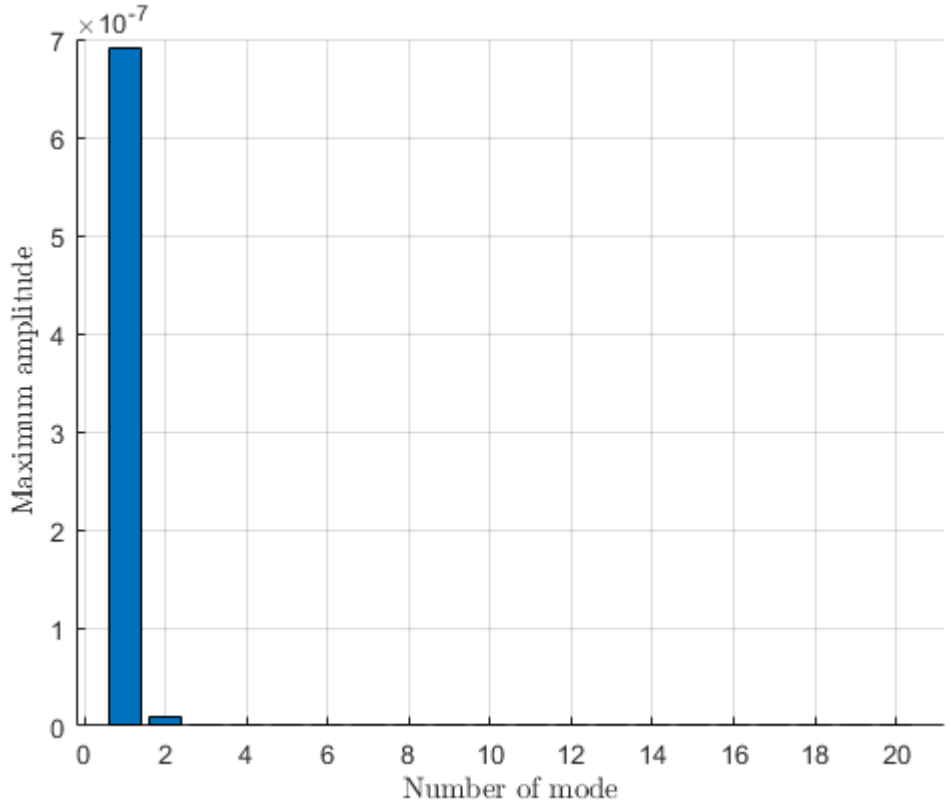

Figure 6.32: Maximum amplitude q_i^{max} of each mode of vibration ϕ_i.
Source: Own elaboration.

In this case, only the first two modes are activated, being the first one the most dominant one by far. This mode, as one would expect, represents bending motion (see figure 6.17).

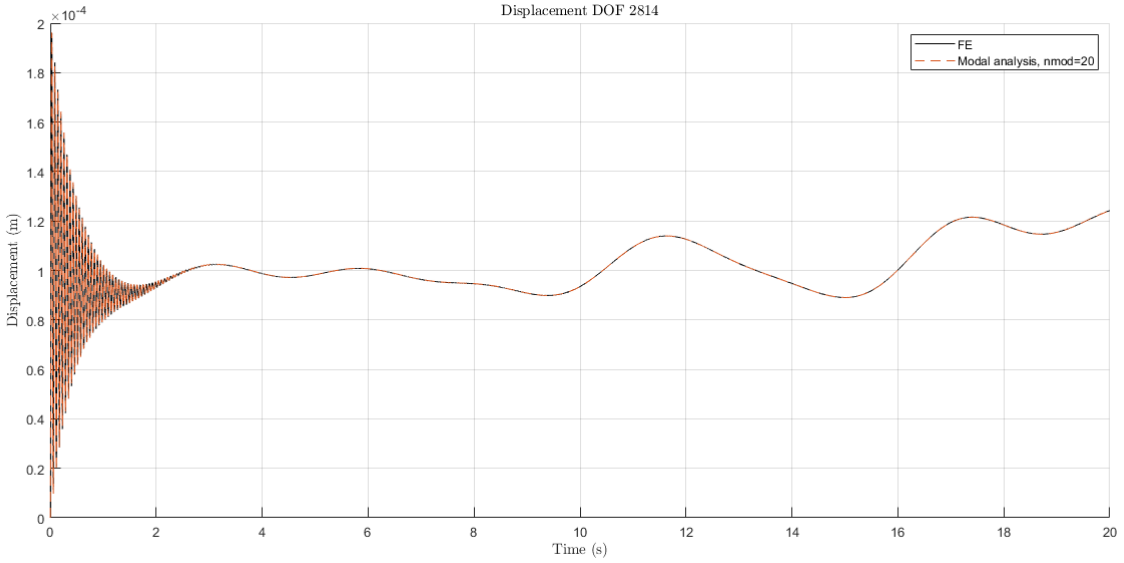

Figure 6.33: Comparison between the 2814^{th} DOF displacement obtained by the FE analysis and the one deduced from the modal decomposition analysis.
Source: Own elaboration.

Regarding the modal analysis, the analytical solution is the same as in 6.12 but with the exception that, for the wind, the number of sines increases from 10 to 43 and thus $k = 43$.

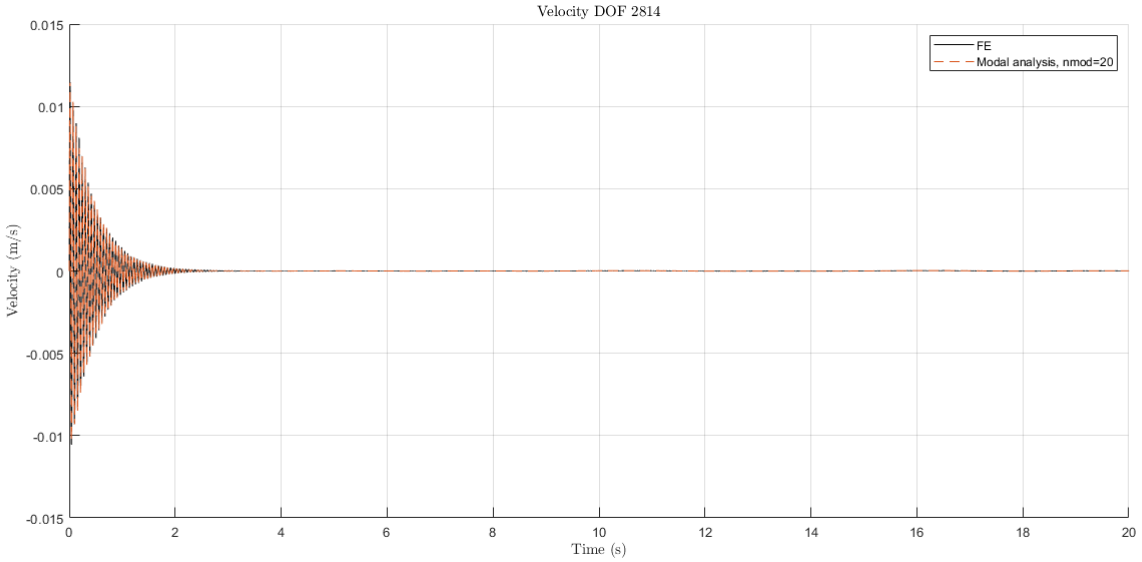

Figure 6.34: Comparison between the 2814^{th} DOF velocity obtained by the FE analysis and the one deduced from the modal decomposition analysis.
Source: Own elaboration.

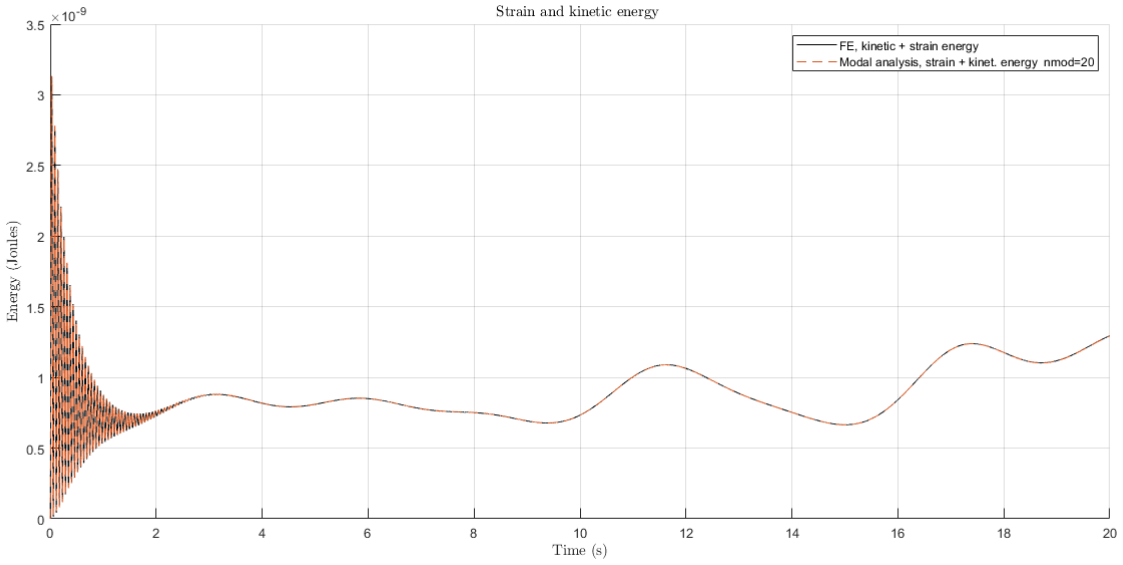

Figure 6.35: Comparison between the 2814^{th} DOF energy obtained by the FE analysis and the one deduced from the modal decomposition analysis.
Source: Own elaboration.

Likewise in the sine combination of section 6.2.3, the FEM matches perfectly with the modal analysis. Moreover, given that the time domain is larger in this simulation, the time constant τ discussed in section 6.2.2 can be better visualized in figure 6.33.

6.4.3 Hyperreduction Stage

In addition to what has been addressed so far, this section also seeks to analyze the outcome of the HROM stage. After including the computational implementation of this technique, which is detailed in section 4.6, in the code and running it, one is faced with figures 6.36, 6.37 and 6.38.

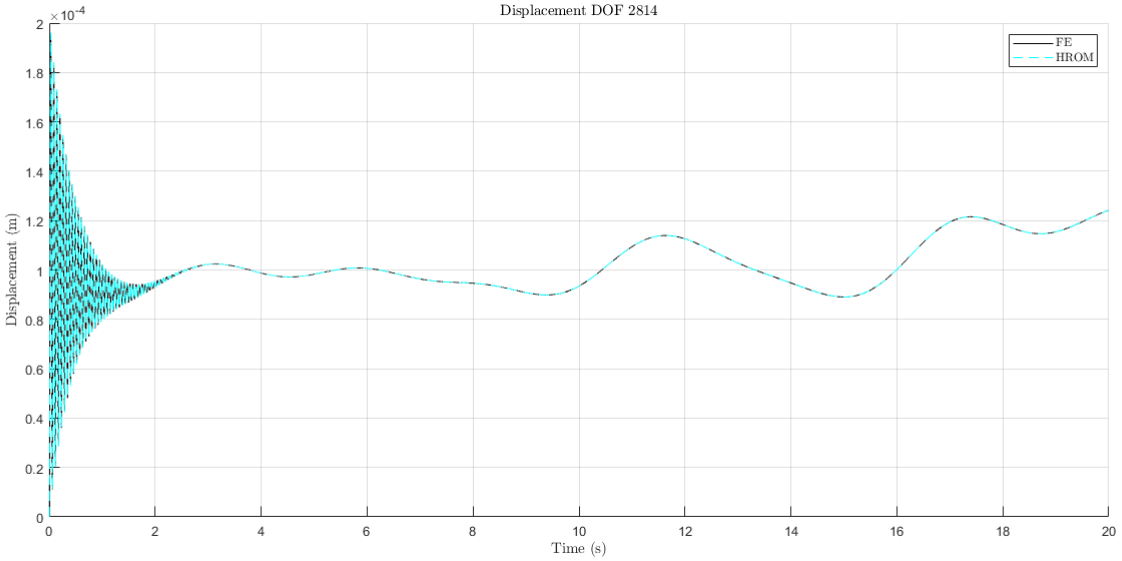

Figure 6.36: Comparison between the 2814^{th} DOF displacement obtained by the FE analysis and the one extracted from the HROM.
Source: Own elaboration.

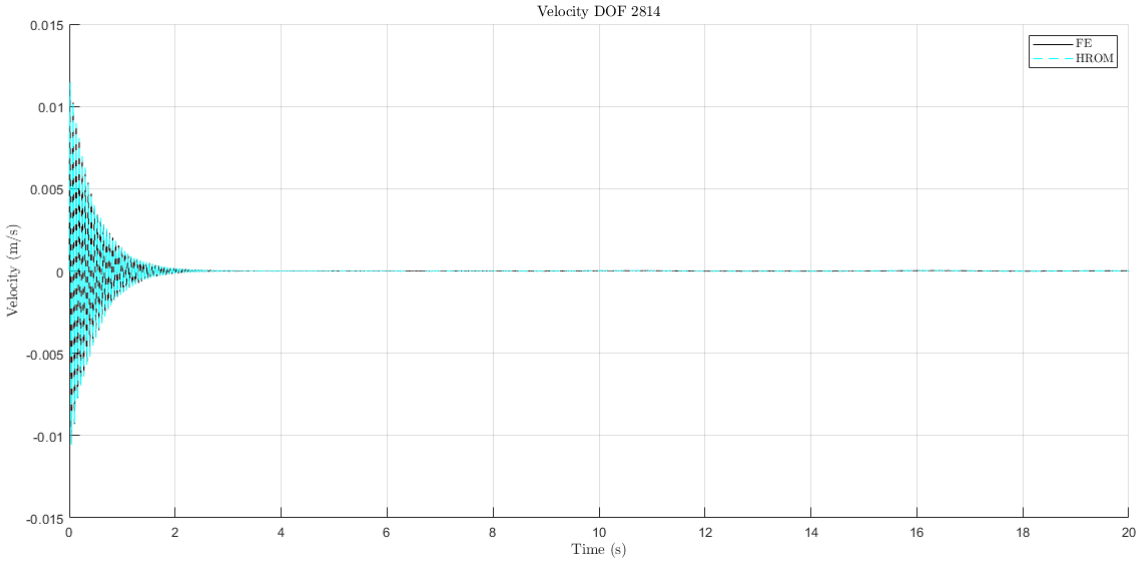

Figure 6.37: Comparison between the 2814^{th} DOF velocity obtained by the FE analysis and the one extracted from the HROM.
Source: Own elaboration.

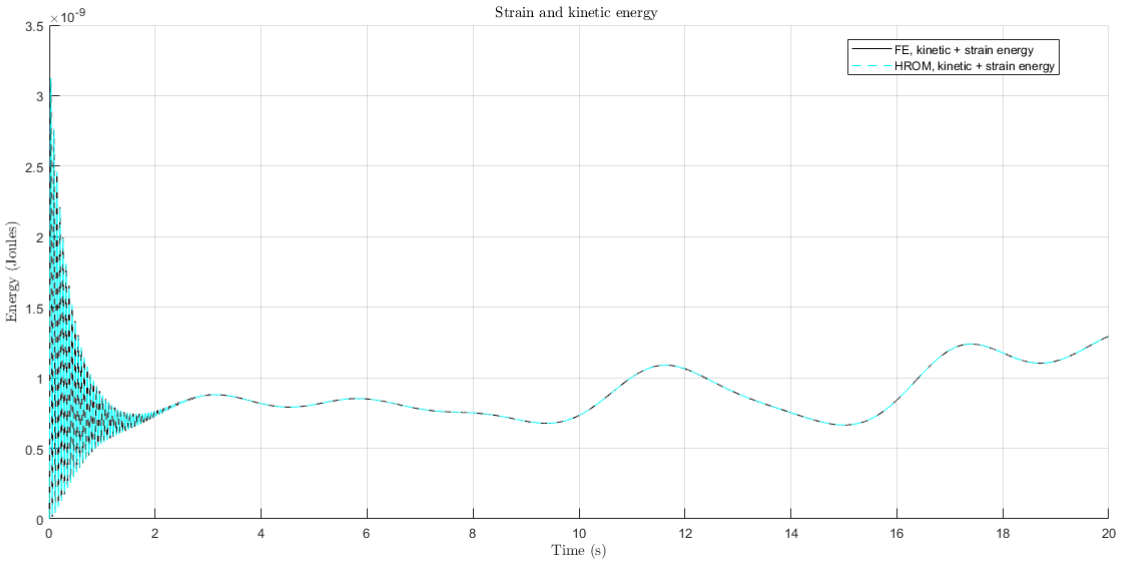

Figure 6.38: Comparison between the 2814^{th} DOF energy obtained by the FE analysis and the one extracted from the HROM.
Source: Own elaboration.

Figures 6.36, 6.37 and 6.38 show that the HROM matches perfectly with the FEM. Moreover, to further support the previous statement, the code calculates both the displacement and PK2 stresses errors of the HROM with respect to the FEM. In this simulation the error in the displacement has been of 1.01×10^{-3}, whilst for the PK2 stresses 6.49×10^{-3}.

Besides recognizing that the results obtained from both the FEM and the HROM are matched, it is more convenient to analyze the computational aspects to check whether the HROM, in addition of having a satisfactory precision, is also more efficient than the FEM.

- Firstly, the computational effort is reduced from 1032.39 seconds in the FEM to 34.18 seconds, which represents a 96.69% decrease.
- In second place, the number of modes Φ required has been only 2 for the displacements, the PK1 stresses and for the PK2 stresses.
- Finally, the number of Gauss points selected by the ECM to integrate the internal forces has been just 4, which only represent a 0.28% of the total 1407 nodes of the mesh. These points, as depicted in figure 6.39, are located in 4 different finite elements of the beam's mesh.

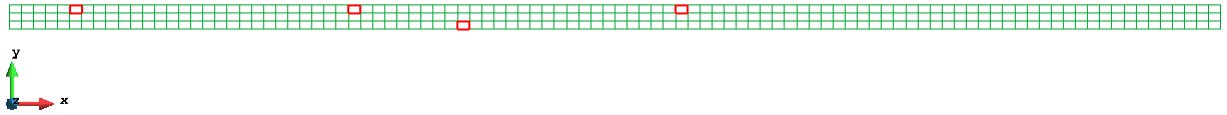

Figure 6.39: Location of the elements containing the 4 ECM selected Gauss points required to integrate the internal forces in the reduced order space.
Source: Own elaboration.

If one wished to obtained a smaller error, the number of modes could be arbitrarily defined as an input of the code instead of being obtained by the HROM stage. For example, imposing a number of modes of 6, the displacement error is reduced by two orders of magnitude (from 1.01×10^{-3} to 2.42×10^{-5}), whilst for the PK2 stresses the decrease is not as remarkable (from 6.49×10^{-3} to 2.3×10^{-3}).
Nonetheless, an increase in accuracy also brings an increase in computational effort, since with 6 modes, the computational duration is 32.29 seconds longer and the number of Gauss points rises up to 22.

It can be concluded that the HROM is significantly more efficient than the FEM and, additionally, it does not involve a decrease in accuracy.
Nevertheless, these results have been obtained under the small strains hypothesis. Hence, it would also be interesting to evaluate how does the HROM behave in nonlinear systems.

6.5 Nonlinear Analysis

Until this point, all the different simulations and studies that have been conducted were under the small strains hypothesis, i.e linear regime.
Since one of the objectives of this thesis is to get introduced to the nonlinear regime, it has been decided to launch a simple but yet illustrative simulation.
Hence, the analysis to be conducted will study the dynamic response of the beam when subjected to an external force formed by a single sine, just like in section 6.2.2. However, the phase shift φ will not be included in the external force. Thus, the external force expression can be extracted from equation 6.1:

$$F^{ext}(t) = \bar{F} sin(\Omega t)$$

To assess the results and compare them to the linear regime, each simulation will be launched in both the linear and the nonlinear regime. More precisely, and to better visualize the difference between the linear and nonlinear analysis it has been chosen to conduct two studies: one with an external force that would cause a relatively small maximum displacement, and the other with a greater force, one which would create a maximum displacement large enough to force the system response to be nonlinear.

With that in mind, $\bar{F}$ will be estimated depending on the desired maximum displacement of the beam whilst Ω will remain constant along this section. To avoid a large number of time steps, it has been supposed that $\Omega = 30\ rad/s$. The number of time steps and time domain are set to 4000 and 1.15 seconds respectively, just

like in section 6.2.2.

Moreover, since the modal decomposition analysis has only been addressed for linear systems, the upcoming simulations will only include the FE and HROM analysis.

6.5.1 Small Strains

To estimate the maximum displacement that the force will cause, one must look at $\bar{F}$, since the frequency of the harmonic does not have any effect on the amplitude of the displacement.
Taking a look into the analytical method of study, i.e the modal decomposition analysis, see equation 4.77, the vector of nodal displacements d is given by:

$$d = \sum_{i=1}^{n_{modes}} \phi_i q_i \tag{6.31}$$

For the case of damped vibrations produced by a harmonic external force like the one defined in equation 6.1 (see section 4.4.2), q_i is given by:

$$q_i = q_i^{max} \left\{ e^{\bar{\xi}_i \omega_i t} \left[A_i cos(\bar{\omega}_i t) + B_i sin(\bar{\omega}_i t) \right] + (1 - \bar{\rho}_i^2) sin(\Omega t) - 2\bar{\xi}_i \bar{\rho}_i cos(\Omega t) \right\} \tag{6.32}$$

Since this case of study does not contemplate any phase shift, constants A_i and B_i of the homogeneous solution are the same as the ones in expression 4.99, but making $\varphi = 0$. Thus:

$$\begin{aligned} A_i &= 2\bar{\xi}_i \bar{\rho}_i \\ B_i &= \tfrac{1}{\bar{\omega}_i} \left(A_i \, \bar{\xi}_i \omega_i - (1 - \bar{\rho}_i^2) \Omega \right) \end{aligned} \tag{6.33}$$

In all the simulations that have been conducted, the maximum displacement is given at the beginning of the response (almost when $t = 0\ s$). That means that the exponential and the sines in the above equation 6.32 can be neglected.
Therefore, the maximum displacement of the response can be estimated with q_i^{max}, which, according to equation 4.97, is given by:

$$q_i^{max} = \frac{f_i}{\omega_i^2} \frac{1}{\left(1 - \bar{\rho}_i^2\right)^2 + \left(2\bar{\xi}_i \bar{\rho}_i\right)^2} = \frac{\phi_i^T \bar{F}}{\omega_i^2} \frac{1}{\left(1 - \bar{\rho}_i^2\right)^2 + \left(2\bar{\xi}_i \bar{\rho}_i\right)^2} \tag{6.34}$$

Since the dynamic response of the structure under this kind of force is a combination of bending modes, it is interesting to analyze which of these modes are triggered by Ω and $\bar{F}$.
To identify them, the modal response of the structure is analysed using an arbitrary value of $\bar{F}$, say $\bar{F} = 1$. (the mode excitation is dictated by Ω while the mode maximum amplitude is related to $\bar{F}$). Then:

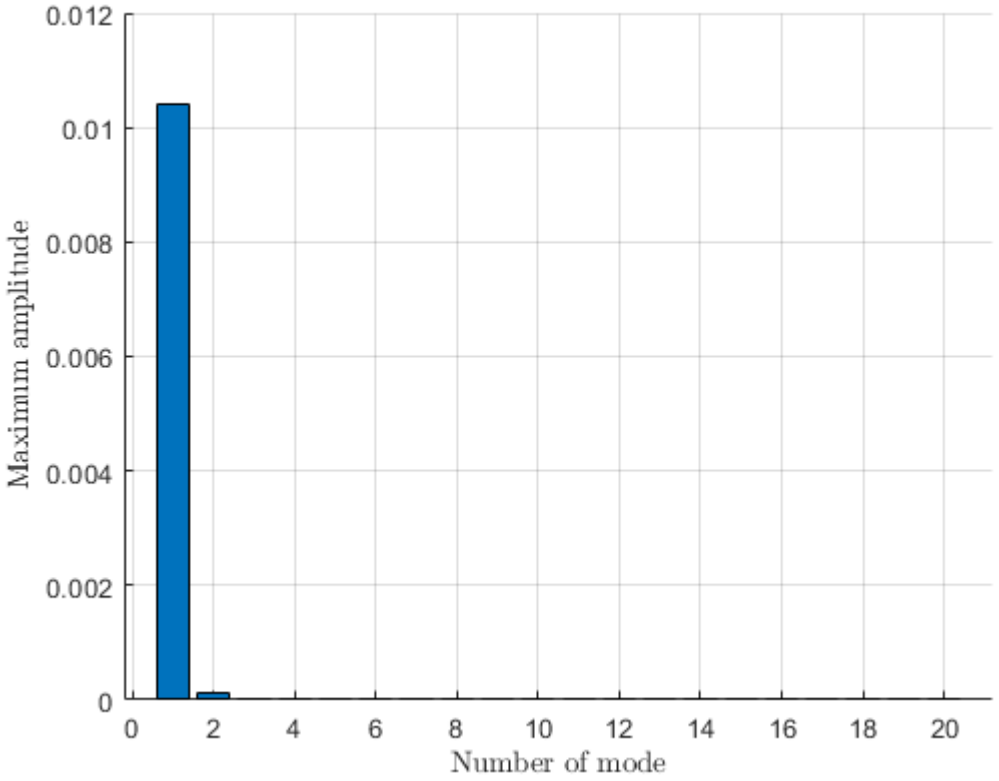

Figure 6.40: Representation of the structure natural modes that are triggered by a $\Omega = 30\ rad/s$ and harmonic external force.
Source: Own elaboration.

And the response obtained considering $\bar{F} = 1$ implies a maximum displacement of approximately 3.15 meters, as seen in figure 6.41.

Considering that the beam length is only 1 meter, it is clearly noticeable that a maximum displacement of more than 3 meters is impossible. However, these results are obtained under the small strains hypothesis, which means that there are no limitations of movement on the dynamic response of the structure. Hence, this result is only used as an orientation to estimate the maximum displacement of the linear response.

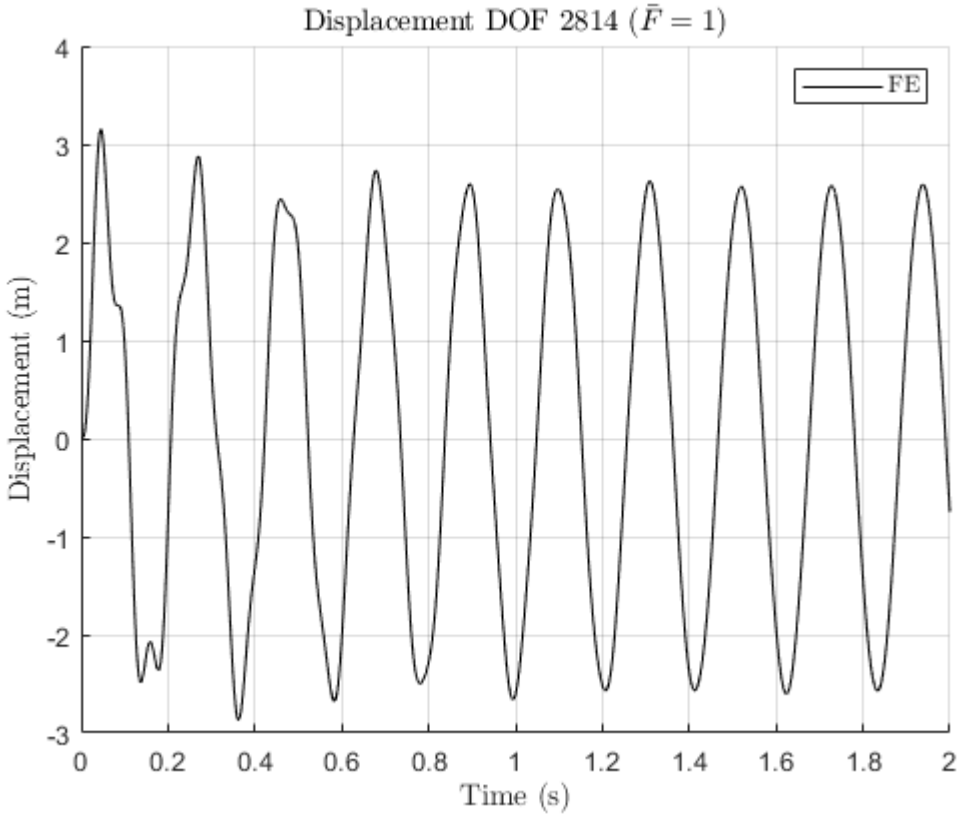

Figure 6.41: Displacement response of the structure when a $\bar{F} = 1$ external force is applied.
Source: Own elaboration.

According to equation 6.31, the nodal displacement vector is a linear combination of modes shapes ϕ_i and temporal functions $q_i(t)$ which represent the amplitude of each mode along time. Therefore, and since modifying $\bar{F}$ only affects q_i^{max}, one can establish a proportional relationship between d^{max} and $\bar{F}$.
In other words, taking into account that for $\bar{F} = 1$ the maximum displacement is 3.15 meters, one could use a simple linear interpolation to deduce the required $\bar{F}$ given an arbitrary d^{max}.

In order to ensure that the structure responds under the linear regime, it has been opted for a relatively small value of the maximum displacement of the beam, i.e $d^{max} = 2\ cm$. Thus, the required value of $\bar{F}$ is interpolated as:

$$\bar{F} \approx 0.0063\ MPa$$

After launching the simulations in both regimes, the displacement and energy plots obtained with the two methods can be compared.

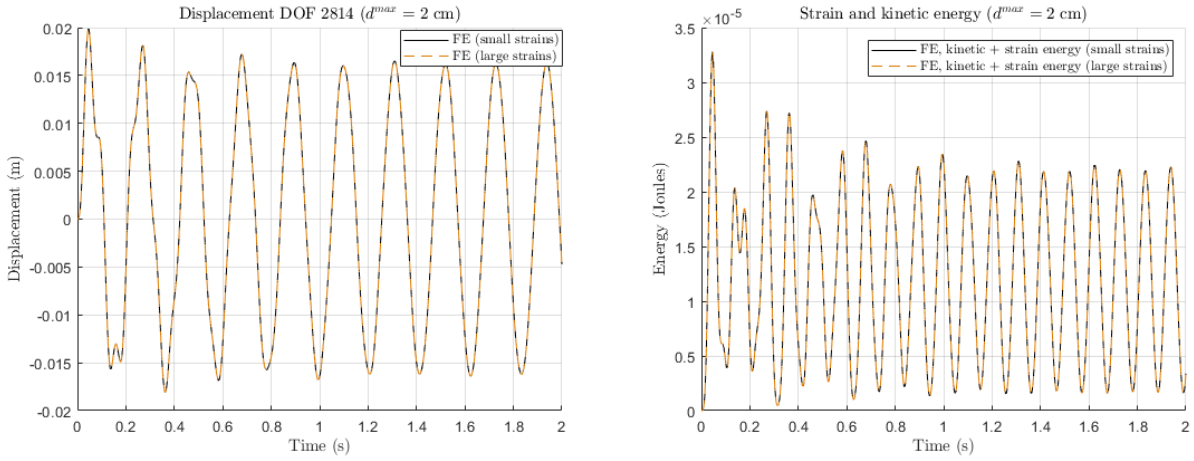

(a) Displacement

(b) Energy

Figure 6.42: Comparison between the displacement (a) and energy (b) results obtained when $d^{max} = 2$ cm, under both the linear hypothesis and those achieved considering nonlinear regime.
Source: Own elaboration.

As it can be observed in figure 6.42, the linear interpolation to estimate the maximum displacement is appropriate for this case of study.

Moreover, for the small strain case, linear and nonlinear results coincide. This is easily explained with the fact that, for small strains, the nonlinearity of the structure is almost inappreciable, due to the fact that the deformation is small.

Nonetheless, the HROM performance and efficiency, as table 6.1 suggests, has decreased for the nonlinear case, particularly with regard to the number of elements selected by the ECM and, especially, the consistency.

Parameter	**Linear Simulation**	**Nonlinear Simulation**
Time	10.00 s	15.54 s
d Modes	2	3
PK1 Modes	2	3
PK2 Modes	2	3
ECM Points	4	10
d error	2.65×10^{-4}	8.52×10^{-3}

Table 6.1: Performance parameters of the HROM under both the linear and nonlinear hypothesis in a small strains study, i.e $d^{max} = 2$ cm.

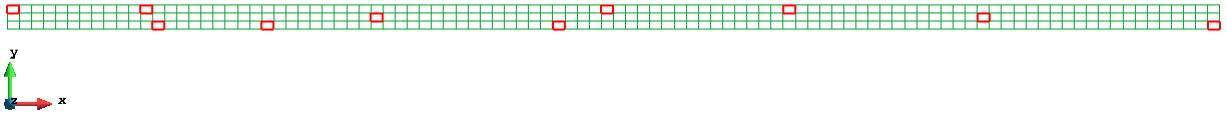

Figure 6.43: Location of the elements containing the 10 ECM selected Gauss points required to integrate the internal forces in the reduced order space.
Source: Own elaboration.

6.5.2 Large Strains

According to figure 3.1 in section 3, the length of the beam is 1 meter. Thus, to ensure that the problem will be nonlinear at the same time that it does not involve any buckling phenomena, it has been decided to impose a maximum displacement equivalent to 65% of the beam's length. In other words, the beam should bend up to 65 cm from its equilibrium position.

Repeating the same linear interpolation explained in the previous section, the required $\bar{F}$ has the following value:

$$\bar{F} \approx 0.206\ MPa$$

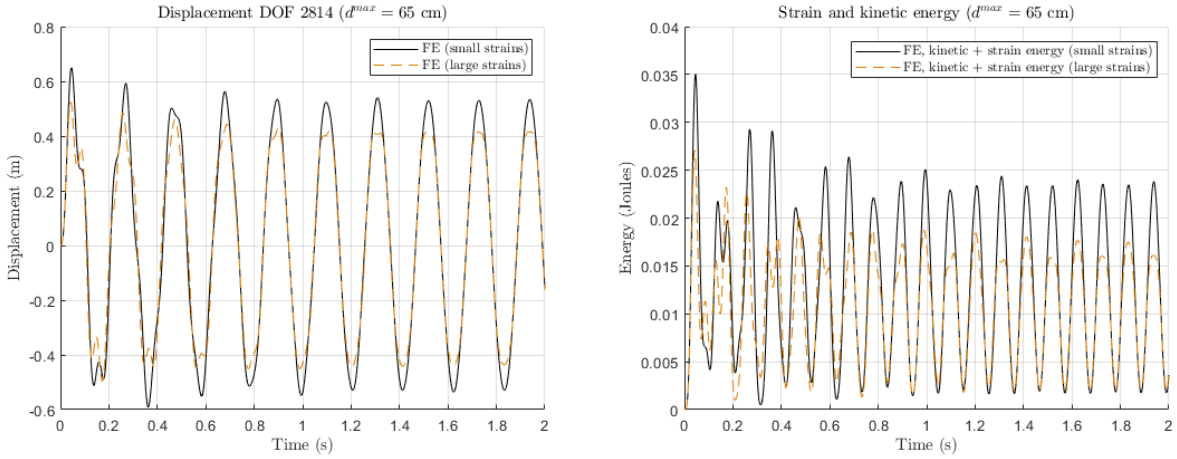

(a) Displacement

(b) Energy

Figure 6.44: Comparison between the displacement (a) and energy (b) results obtained when $d^{max} = 65$ cm, under both the linear hypothesis and those achieved considering nonlinear regime.
Source: Own elaboration.

In the nonlinear regime, $\tilde{C}$ is larger (see section 4.3), which translates also into a greater stiffness matrix K and thus, as it can be seen in figure 6.44, the structure experiences a more rigid behaviour as its movement seems to be limited.

In conclusion, it is clear that the displacements obtained using the nonlinear approach must differ from the ones computed with the linear hypothesis: the rigidity or stiffness increase discussed above suggests a lower displacement for this approach.

Hence, it seems like the real properties of the material (which are nonlinear), would not let one node situated at the tip of the beam (which corresponds to DOF 2814) bend up to 65 cm. Instead, the beam is only able to deflect up to roughly 50 cm.

As it has been done in the small strains simulation, the HROM efficiency must also be checked. However, since the linear simulation does not give legitimate results when subjected to large strains, the comparison is to be done between the nonlinear HROM performed considering $d^{max} = 2$ cm and $d^{max} = 65$ cm.

Parameter	$d^{max} = 2$ **cm Simulation**	$d^{max} = 65$ **cm Simulation**
Time	15.54 s	21.37 s
d Modes	3	4
PK1 Modes	3	4
PK2 Modes	3	4
ECM Points	10	17
d error	8.52×10^{-3}	0.03

Table 6.2: Performance parameters of the HROM under both the linear and nonlinear hypothesis in a large strains study, i.e $d^{max} = 65$ cm.

Finally, figure 6.45 shows the exact location of the 17 elements that include these 17 points selected by the ECM.

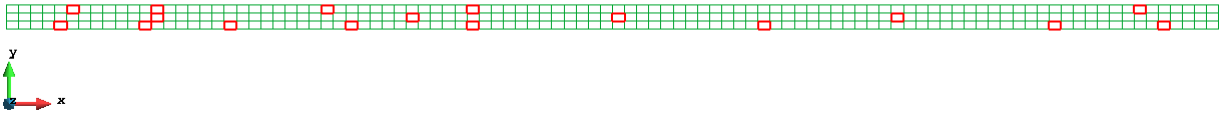

Figure 6.45: Location of the elements containing the 17 ECM selected Gauss points required to integrate the internal forces in the reduced order space.
Source: Own elaboration.

As explained, the nonlinearities of the problem (which only manifest when large strains are considered) affect the computation of the stiffness matrix and ultimately contribute to an increase in the number of iterations of the Newton-Raphson scheme. Moreover, in order to achieve convergence, more integration point are also required.

Given such circumstances, the computational effort associated to the FEM is drastically increased from 177.50 seconds in the small strains regime, to 601.87 seconds in the large strains.
As a consequence, the HROM computational parameters depicted in table 6.2 have also increased, but just slightly. Nonetheless, the HROM performance is still very remarkable with respect to the FEM, including computational time reduction of more than 90%.

Chapter 7

Budget Summary

This thesis has not involved any direct costs. However, the author has gathered a set of different indirect costs that would have been considered had it been a real engineering project.

As seen in table 7.1, the total budget consists on three distinct costs: the software license cost, the electric consumption and the cost associated to the professional fees.

The budget breakdown is further explained in the Budget Annex.

Expenses	**Cost [€]**
Software	1040
Electric Consumption	25.74
Professional Fee	2268
TOTAL	**3333.74**

Table 7.1: Breakdown of the budget associated to this thesis' development.

Chapter 8

Analysis and assessment of environmental and social implications

The intention of this chapter is to give a brief analysis and assessment of how the study that the thesis focuses on considers environmental and social considerations or has a positive impact in these dimensions.

Since this work is only focused on the study of the methodology behind the finite element implementation of the structural vibrations problem, there little to no direct contributions to those considerations.
Nonetheless, it is safe to say that this project can create an indirect positive impact both environmentally and socially, when scaled to real life situations.

Being able to predict the dynamic response of a structure is, on its own, a concept that has a huge range of applications in any engineering industry, since the vast majority of engineering designs do include some kind of structure that must withstand a series of external conditions. Furthermore, if one includes the optimization phase, in this case the HROM, the impact becomes even higher, since reducing the number of points/elements of the FE mesh required to obtain practically the same response is translated into being able to simulate really complex situations much more efficiently. These scenarios can go from large structures made up of really refined meshes to circumstances where the state of the system is highly nonlinear and complicated to compute.

Socially, these benefits imply, as already mentioned, being able to predict the dynamic response that any structure of interest, such as a building, bridge, plane, etc. would have under certain dangerous conditions, thus preventing lots of lives from being taken. These interesting situations include earthquakes, strong winds or typhoons, impacts or crashes, fatigue/buckling failures ...

When a catastrophe or accident that involves human beings takes places, it usually leaves so many traces that are really difficult to correct or get rid of. For example, when an earthquake or typhoon hits a city, lots of structures are devastated and even sometimes, part of the city or even its entirety has to be abandoned. Environmentally, being capable of launching simulations of such caliber would involve predicting the response that structures would have against these kind of accidents. Since human beings have a huge impact on the environment, being able to predict, reduce or even avoid these misfortunes would drastically decrease the footprint that man-made related disasters leave on the environment.

Although this project is a major simplification of all those above-mentioned cases, it is important to understand that it lays the foundations from which complexity can progressively be increased, until, eventually, the model is scaled to the magnitude of any of the previous real life scenarios.

Chapter 9

Conclusions

After having performed all the studies detailed in chapter 6, one could extract some relevant conclusions about the present thesis, as well as some ideas about future work or aspects to improve.
This chapter will be divided into three different topics, each of which will cover one of the three main objectives of the present work: the hyperreduction analysis, the nonlinear regime and the wind study.

First of all, it is of utmost importance to talk about the FEM and the HROM: they represent the heart of this work, since, without them, no simulations would have been possible to launch.

Thanks to a deep analysis conducted in chapter 4, the author achieved the necessary background and knowledge that enabled him to perform several simulations with different types of external forces as well as analyse its dynamic response.

However, since Finite Element analysis is not anything new, the author wanted to apply dimensionality reduction techniques in order to significantly optimize the solver. To do so, the classical finite element shape functions used in the FEM were replaced by spaces spanned by globally supported basis.

After having discussed in sections 6.4 and 6.5 the results obtained from the wind and the nonlinear analysis respectively, it can be concluded that the HROM stage is far better than humans in uncovering dominant patterns from data. Hence, it represents a qualitative leap in modelling physical systems which are considerably more complex than the cantilever beam.

The Empirical *Cubatre* Method (ECM) has enabled the evaluation of the internal forces in a set of reduced Gauss points instead of in the totality of Gauss points (as it is the case in the FEM).
Thanks to this tailored *cubature* scheme, the computational time required to solve the problem is reduced by more than 96% in section 6.4 and by more than 90% in 6.5. Moreover, the number of elements, which corresponded to 506 by default, has been decreased to just 4 for section 6.4 and to 17 for 6.5.
Besides having achieved these upgrades in efficiency, it has also been observed that the accuracy has not been

compromised: in the wind simulation (which included the linear hypothesis), the error of the displacements has been 1.01×10^{-3}, while for the stress the error has been 6.49×10^{-3}.
On the other hand, in nonlinear simulations included in section 6.5, the displacement error has been kept in the order of 10^{-2} or below.
Nevertheless, the employed ROM partitioning framework is rather general, and extensions to geometrically distinct subdomains, as well as continuous interface boundaries, could be applied in future studies with minor modifications.

Unfortunately, the computational approach that has been carried out to perform the FEM simulations does have a major disadvantage, and that is the required number of time steps.
As it has been repeatedly showed in various sections from chapter 6, the number of time steps that are needed to conduct simulations where the external force is formed by either high frequency sines or combination of several of them, is drastically high due to the noisy and narrow-peaked nature of these functions.
Therefore, it would be really interesting, as further work, to develop an algorithm that could create adaptable time vectors, i.e reducing the Δt in periods where the response is expected to be transient and increasing it when the response becomes more steady. Furthermore, it would also be interesting to research ML time-forecasting algorithms that could be capable of predicting the behaviour of the dynamic response and thus would require less number of time steps.

In second place, the nonlinear analysis has also been conducted satisfactorily. Although consisting just on an introduction, the student has been able to get familiar with a phenomena that is omnipresent in any engineering problem. It has been observed that, when structures are subjected to large deformations, their stiffness increases and thus their movement becomes more restricted than under the linear hypothesis.

It has also been noticed that in the nonlinear regime, the computational time was higher due to a larger number of iterations needed to achieve convergence in the Newton-Raphson algorithm.
As a result, the performance of the nonlinear HROM worsened with respect to the one obtained under the small strains hypothesis: nonlinearities always complicate matters since they demand more calculations and, thus, more ECM points. According to [5], the ECM is not optimal and there is room for improvement, since it does not exploit the topology of the function it intends to integrate. On that account, it would be worth exploring whether the ECM algorithm can be improved so that it gives out less integration points without threatening accuracy.

In third place, and regarding the wind analysis, being able to find papers including experiments or studies that involved measurements of wind speed in short periods of time has been extremely hard, since the most frequent sampling rate for wind measurements is usually hourly or daily. In addition, extracting the data, which had to be done manually, further complicated matters as it demanded high amounts of precision and

patience.

Besides that, the Fast Fourier Transform, which was quite unfamiliar to the author at first, has been of vital importance to the analysis of the structure under the action of the wind. Being able to obtain a continuous representation of discrete data in such a simple way implies having the capacity of studying the dynamic response of a structure for almost any kind of external condition, as long as it is properly represented with a discrete dataset, i.e constant sampling rate, even number of samples, etc.

Finally, and as a rather personal conclusion, the author believes that although it may seem that the present thesis' results are not of great value, it is all the process and adaptation to new concepts and especially new variants of code that represent the actual effort behind this work.
Having been faced with a Matlab code of such magnitude as the one used in the present work has not only extended the author's knowledge on this software, but has also given the opportunity to visualize the way in which real-life problems of finite elements are addressed as well as understand how is all the code structured in order to achieve the maximum efficiency.

References

1. BRUNTON, Steven L; KUTZ, J Nathan. *Data-driven science and engineering: Machine learning, dynamical systems, and control*. Cambridge University Press, 2022.
2. HEY, Anthony JG; TANSLEY, Stewart; TOLLE, Kristin Michele, et al. *The fourth paradigm: data-intensive scientific discovery*. Microsoft research Redmond, WA, 2009.
3. TEAM, Spatial. *An introduction to Finite Element modelling* [online]. 2020 [visited on 2022-07-29]. Available from: https://blog.spatial.com/finite-element-modeling//29-07.
4. HERNÁNDEZ, JA; OLIVER, Javier; HUESPE, Alfredo Edmundo; CAICEDO, MA; CANTE. High-performance model reduction techniques in computational multiscale homogenization. *Computer Methods in Applied Mechanics and Engineering*. 2014, vol. 276, pp. 149–189.
5. HERNÁNDEZ, JA. A multiscale method for periodic structures using domain decomposition and ECM-hyperreduction. *Computer Methods in Applied Mechanics and Engineering*. 2020, vol. 368, p. 113192.
6. CARLBERG, Kevin; BOU-MOSLEH, Charbel; FARHAT, Charbel. Efficient non-linear model reduction via a least-squares Petrov–Galerkin projection and compressive tensor approximations. *International Journal for numerical methods in engineering*. 2011, vol. 86, no. 2, pp. 155–181.
7. RYCKELYNCK, David. Hyper-reduction of mechanical models involving internal variables. *International Journal for numerical methods in engineering*. 2009, vol. 77, no. 1, pp. 75–89.
8. BARRAULT, Maxime; MADAY, Yvon; NGUYEN, Ngoc Cuong; PATERA, Anthony T. An 'empirical interpolation'method: application to efficient reduced-basis discretization of partial differential equations. *Comptes Rendus Mathematique*. 2004, vol. 339, no. 9, pp. 667–672.
9. CHATURANTABUT, Saifon; SORENSEN, Danny C. Discrete empirical interpolation for nonlinear model reduction. In: *Proceedings of the 48h IEEE Conference on Decision and Control (CDC) held jointly with 2009 28th Chinese Control Conference*. 2009, pp. 4316–4321.
10. NGUYEN, Ngoc Cuong; PATERA, Anthony T; PERAIRE, Jaime. A 'best points' interpolation method for efficient approximation of parametrized functions. *International journal for numerical methods in engineering*. 2008, vol. 73, no. 4, pp. 521–543.
11. BAIGES, Joan; CODINA, Ramon; IDELSOHN, Sergio. Explicit reduced-order models for the stabilized finite element approximation of the incompressible Navier–Stokes equations. *International Journal for Numerical Methods in Fluids*. 2013, vol. 72, no. 12, pp. 1219–1243.

12. ASTRID, Patricia; WEILAND, Siep; WILLCOX, Karen; BACKX, Ton. Missing point estimation in models described by proper orthogonal decomposition. *IEEE Transactions on Automatic Control*. 2008, vol. 53, no. 10, pp. 2237–2251.
13. HERNANDEZ, Joaquin Alberto; CAICEDO, Manuel Alejandro; FERRER, Alex. Dimensional hyper-reduction of nonlinear finite element models via empirical cubature. *Computer methods in applied mechanics and engineering*. 2017, vol. 313, pp. 687–722.
14. BONET, Javier; WOOD, Richard D. *Nonlinear continuum mechanics for finite element analysis*. Cambridge university press, 1997.
15. BELYTSCHKO, Ted; LIU, Wing Kam; MORAN, Brian; ELKHODARY, Khalil. *Nonlinear finite elements for continua and structures*. John wiley & sons, 2014.
16. PO, OC. *Zienkiewicz and RL Taylor, The Finite Element Method*. McGraw Hill, 1989.
17. ORTEGA, Joaquín Alberto Hernández. *FE 1D theory plus Nonlinear*. ESEIAAT, 2020.
18. ZIENKIEWICZ, Olek C; TAYLOR, Robert Leroy; ZHU, Jian Z. *The finite element method: its basis and fundamentals*. Elsevier, 2005.
19. FISH, Jacob; BELYTSCHKO, Ted. *A first course in finite elements*. John Wiley & Sons New York, 2007.
20. ZIENKIEWICZ, Olgierd Cecil; TAYLOR, Robert Leroy; TAYLOR, Robert Leroy; TAYLOR, Robert Lee. *The finite element method: solid mechanics*. Butterworth-heinemann, 2000.
21. WOOD, WL; BOSSAK, M; ZIENKIEWICZ, OC. An alpha modification of Newmark's method. *International journal for numerical methods in engineering*. 1980, vol. 15, no. 10, pp. 1562–1566.
22. HUGHES, Thomas JR. *The finite element method: linear static and dynamic finite element analysis*. Courier Corporation, 2012.
23. ORTEGA, Joaquín Alberto Hernández. *Projection-based hyperreduced-order models (dynamic analysis). Clustering techniques*. ESEIAAT, 2020.
24. COOK, Robert D. *Modeling for Stress Analysis*. New York: Wiley, 1994.
25. CHOPRA, Anil K. *Dynamics of structures (Vol. 3, p. 339)*. New Jersey: Prentice Hall, 1995.
26. NOBACH, Holger; TROPEA, Cameron; CORDIER, Laurent; BONNET, Jean Paul; DELVILLE, Joël; LEWALLE, Jacques; FARGE, Marie; SCHNEIDER, Kai; ADRIAN, Ronald. Review of some fundamentals of data processing. In: *Springer Handbooks*. Springer, 2007, pp. 1337–1398.
27. CLOUGH, RW; PENZIEN, J. (1993), Dynamics of Structures. McGraw Hill, New York. [N.d.].
28. BISHOP, Christopher M; NASRABADI, Nasser M. *Pattern recognition and machine learning*. Springer, 2006. No. 4.
29. LIBRARY, ASCE. *Maxwell Damping: An Alternative to Rayleigh Damping* [online]. 2021 [visited on 2022-07-14]. Available from: https://ascelibrary.org/doi/abs/10.1061/9780784483701.004.
30. DEMKOWICZ, Leszek F; GOPALAKRISHNAN, Jay. An overview of the discontinuous Petrov Galerkin method. *Recent developments in discontinuous Galerkin finite element methods for partial differential equations*. 2014, pp. 149–180.
31. ORTEGA, Joaquín Alberto Hernández. *Projection-based hyperreduced-order models (static analysis)*. ESEIAAT, 2020.

32. AMSALLEM, David; ZAHR, Matthew J; FARHAT, Charbel. Nonlinear model order reduction based on local reduced-order bases. *International Journal for Numerical Methods in Engineering*. 2012, vol. 92, no. 10, pp. 891–916.
33. PAGANI, Stefano; MANZONI, Andrea; QUARTERONI, Alfio. Numerical approximation of parametrized problems in cardiac electrophysiology by a local reduced basis method. *Computer Methods in Applied Mechanics and Engineering*. 2018, vol. 340, pp. 530–558.
34. LIPTAK, Bela G. *Instrument Engineers' Handbook, Volume One: Process Measurement and Analysis*. CRC press, 2003.
35. CERNA, Michael; HARVEY, Audrey F. *The fundamentals of FFT-based signal analysis and measurement*. 2000. Tech. rep. Application Note 041, National Instruments.
36. VISWANATHAN, Mathuranathan; MATHURANATHAN, V. Digital Modulations using MATLAB. *Building Simulation Models from Scratch. India, Pilani*. 2017.
37. MARTIN-MARTINEZ, Sergio; VIGUERAS-RODRIGUEZ, Antonio; GÓMEZ-LÁZARO, Emilio; MOLINA-GARCIA, Angel; MULJADI, Eduard; MILLIGAN, Michael. Wind power variability and singular events. In: *Advances in Wind Power*. Janeza, 2012, pp. 285–304.
38. LANDAU, Lev Davidovich; LIFSHITZ, Evgenii Mikhailovich. *Fluid Mechanics: Landau and Lifshitz: Course of Theoretical Physics, Volume 6*. Elsevier, 2013.